

N O T I C E

THIS DOCUMENT HAS BEEN REPRODUCED FROM
MICROFICHE. ALTHOUGH IT IS RECOGNIZED THAT
CERTAIN PORTIONS ARE ILLEGIBLE, IT IS BEING RELEASED
IN THE INTEREST OF MAKING AVAILABLE AS MUCH
INFORMATION AS POSSIBLE

DEVELOPMENT OF A SEVERE LOCAL STORM PREDICTION SYSTEM:
A 60-DAY TEST OF A MESOSCALE PRIMITIVE EQUATION MODEL

Final Report for the Period
Dec. 1, 1976 to Sept. 30, 1978

by

Douglas A. Paine, Principal Investigator
John W. Zack

Cornell University
Ithaca, NY 14853

and

Michael L. Kaplan

General Electric Management and Technical Service Co.
NASA Langley Research Center, Hampton, VA 23665

(NASA-CR-162756) DEVELOPMENT OF A SEVERE
LOCAL STORM PREDICTION SYSTEM: A 60-DAY
TEST OF A MESOSCALE PRIMITIVE EQUATION MODEL
Final Report, 1 Dec. 1976 - 30 Sep. 1978
(Cornell Univ., Ithaca, N. Y.) 147 p

N80-17639

Unclassified
G3/47 47165



Prepared under NASA GRANT NSG 1365, entitled,
"The Balance Equation as a Diagnostic Tool for Detecting the Initiation
of the Multiscale Energy Cascade"

TABLE OF CONTENTS

	<u>Page</u>
1.0 The Cascade Approach to the Forecasting of Severe Convective Storms.....	1
1.1 The Meteorological Problem.....	3
1.2 The Cascade Hypothesis.....	6
2.0 Structure of the Primitive Equation Model System.....	12
2.1 Model Equations.....	13
2.2 Vertical Structure.....	14
2.3 Initial Conditions.....	15
2.4 Space Differencing Scheme.....	15
2.5 Time Differencing Scheme.....	16
2.6 Smoother.....	17
2.7 Lateral Boundary Conditions.....	17
3.0 Selected Examples of Model Performance.....	19
3.1 Case I: 14 April 1978.....	24
3.2 Case II: 17 April 1978.....	43
3.3 Case III: 29 April 1978.....	64
3.4 Case IV: 17 June 1978.....	83
3.5 Case V: 12 May 1978.....	107
3.6 Case VI: 18 May 1978.....	121
4.0 Summary.....	138
5.0 References.....	143
6.0 Appendix.....	144

1.0 The Cascade Approach to the Forecasting of Severe Convective Storms

Severe microscale convective storms such as tornadoes, hail-storms and thunderstorms with damaging winds are responsible for millions of dollars of property damage, hundreds of injuries and many fatalities each year. Consequently, an improvement in forecasting of the location and timing of these severe weather events, is an important meteorological goal whose achievement will have significant economic and social value.

The forecasting of these events with useful precision and accuracy, at present, can be considered nearly impossible on a time scale of more than a few hours before their occurrence, even if one uses a relatively liberal definition of useful precision and accuracy. The forecasting of these storms presents a difficult task primarily due to the small spatial and temporal dimensions of the storm circulations relative to the dimensions of the observational and prognostic techniques available to the forecaster. In addition, the incomplete understanding of the physics responsible for their development, movement, dissipation and interconnection with other scales of the atmospheric circulation also contributes to the forecasting problem.

At present, the forecasting of severe convective storms occurs in two basic modes:

- (1) Large scale areas are assessed on a daily or semi-daily basis for the probability of occurrence of severe convective storms during the next 12 or 24 hour period based upon large scale analysis and

forecast techniques. Areas of high probability are classified as potential severe weather locations, and their location can be communicated to the public as a general outlook of severe convective weather.

- (2) Radar, surface weather observations, and satellite imagery are employed to monitor the actual development, movement and dissipation of convective activity. The short term trends in movement and amplification of existing convective features (lines, areas, cells, etc.) form the basis for specific watches and warnings which carry most of the current forecast's economic and social value.

The problems associated with each of the two forecast modes are obvious. The outlook mode is rather vague with respect to location, timing and intensity although it does provide considerable preparation time. The watch/warning mode increases the spatial, temporal and amplitude specifications at the cost of providing less preparation time.

The solution of these problems will certainly require forecasts of atmospheric circulations at a number of different scales and a representation of the interaction of these different scales of circulation. (A summary of atmospheric scales and associated observational phenomena is presented in Figure I-1) Dynamical forecasting procedures (i.e. dynamical numerical models) appear to hold considerable promise for the simulation of the multi-scale processes associated with the development of severe convective storms in advance of their occurrence.

The purpose of this writing is to describe the progress and problems associated with the dynamical forecast system tested by the NASA-Langley research group in coordination with the National Severe Storms Laboratory (NSSL) and the Air Force Global Weather Center (AFGWC) during a 60 day period from April through June 1978.

In subsection 1.1, the meteorological problem of severe convective storm forecasting will be briefly reviewed. Subsection 1.2 will briefly describe the cascade hypothesis which forms the theoretical core of the nested grid dynamical-numerical modelling system under development at NASA-Langley.

Section 2 will describe the dynamical and numerical structure of the model used during the 1978 test period and provide a preliminary description of the proposed multi-grid system which will be employed in future experiments and tests.

Section 3 is a presentation of six cases from the Spring 1978 test period which are illustrative of the model's performance and of its problems.

Finally, section 4 is a preliminary description of potential solutions to the problems discussed in section 3.

1.1 The Meteorological Problem

Severe convective storms are a manifestation of the rapid release of hydrostatic instability. Thus, the prediction of these storms depends upon first forecasting the establishment of the hydrostatic instability, and then forecasting the development of the mechanism which allows its release. Both of these processes are largely controlled by atmospheric circulation systems which

are larger than the convective storm itself. Hence, the forecasting of severe convective storms is a multi-scale atmospheric problem concerned with the establishment and release of hydrostatic instability.

Absolute hydrostatic instability is characterized by an environmental lapse rate which is greater than the dry adiabatic lapse rate. However, large scale atmospheric circulations do not produce deep layers of absolute hydrostatic instability. An instability of this type is destroyed shortly after its development since the initiation of its release requires only slight vertical displacements. Instead, the larger scale circulations tend to produce atmospheric layers which are in a state referred to as potentially unstable. Potential instability is characterized by a layer which when saturated would develop a lapse rate in excess of the moist adiabatic lapse rate. This condition can be identified by the decrease with height of either the potential wet-bulb temperature (θ_w), the equivalent potential temperature (θ_E) or the static energy ($s = C_p T_v + gz + Lm$). Palmén and Newton (1969) distinguished two classes of potential instability depending upon whether the lapse rate is conditionally unstable or not. If the lapse rate is conditionally unstable, vertical accelerations can commence as soon as saturation is reached, usually via lifting, anywhere in the layer. In contrast, a lapse rate which is not conditionally unstable may require considerable additional lifting with latent heating in the lower portion of the layer or upper level evaporation to make the atmosphere hydrostatically unstable. Thus, it should be apparent from this discussion that the establishment of potential instability and the lifting mechanism for

its release are the important factors which must be correctly forecasted by models designed to simulate the convective organization process of circulations larger than the convective cell itself.

In the 1960's and 1970's the development of quasi-geostrophic theory (outlined in Holton, 1972) and large scale quasi-geostrophic numerical models (Shuman and Hovormale, 1968) greatly improved the forecasting of the synoptic scale organization of potential instability and vertical motion. However, the organization of potential instability and vertical motion at the sub-synoptic, meso and sub-meso scales remain very difficult to forecast.

In an effort to forecast the sub-synoptic organization of potential instability and vertical velocities, several experimental attempts have been made to extend the filtered primitive equation model concept to smaller spatial and temporal scales than the large scale synoptic models (e.g. the 167 km grid used by NMC's LFM2 model). This has been done by shortening the grid spacing to about 1/4 of the LFM2 value and appropriately adjusting the other model parameters (e.g. Kreitzberg, et al., 1974; Perkey, 1976). In addition, a parameterization scheme ascertains the net feedback effects (e.g. momentum and energy transport, energy transformations and increased precipitation rates) of microscale circulations at locations in the large scale model fluid where the vertical temperature, pressure and moisture gradients imply hydrostatic instability. These models generate an adequate forecast of the net effects of the convective circulations, but they do not model the entire multiscale organization process or the actual release of the potential instability at the microscale. As a result, the

forecasts do not provide good estimates of the timing and intensity of the microscale circulations. The cascade hypothesis presented in the next subsection may form the core of a numerical-dynamical system which can eventually model the entire multi-scale organization process and the release of the instability at the microscale.

1.2 The Cascade Hypothesis

Paine, et al. (1975) and Paine and Kaplan (1976) have proposed a cascade hypothesis based on a series of isallobarically induced convergence zones which are generated at successively smaller spatial and temporal scales by the action of the next immediately larger scale circulation. This hypothesis is suggested by Prandtl's fundamental description of turbulence (Sutton, 1955) which states that macroscale momentum sources drive microscale momentum sinks by evolving intermediate or mesoscale processes. Implicit in this view of fluid motion is a cascade sequence in which the characteristics (e.g. spatial distributions of mass and momentum) of the macroscale flow field determine the location, amplitude and timing of the mesoscale wave development. The characteristics of the resulting mesoscale circulation, in turn, control the location, amplitude and timing of the microscale circulation. In the atmosphere, the large scale synoptic energy sources produce the mass and momentum geometries necessary to initiate the cascade sequence. The horizontal kinetic energy is then passed down the atmospheric spectrum (to shorter wavelengths) and simultaneously acts to organize the zones of potential vertical instability and low level convergence. Eventually this horizontal kinetic energy initiates the production of vertical kinetic energy through the release of the vertical

Instability. This process can also be viewed as a form of vertical convergence production.

The following brief summary of the hypothesized cascade sequence will refer to the conservation equations for the seven "primitive" dependent atmospheric variables listed in Table 1 (Richardson, 1922) and the divergence, vorticity and pressure tendency equations listed in Table 2. The divergence, vorticity and pressure tendency equations are derived from the primitive equations in the manner described by Hess (1959).

The cascade sequence begins when the synoptic scale mass and momentum distributions possess a geometry such that the terms in the divergence theorem (8) add to produce large time tendencies of convergence and divergence over a sub-synoptic volume of the lower troposphere. Since the $-\alpha \nabla^2 P$, $+f\zeta$ and $-2J(u,v)$ terms usually dominate the divergence equation at large scales, the sum of these will usually dictate where the production of large quantities of convergence or divergence will occur. The details of this process are discussed in Paine et al. (1978).

As areas of large convergence and divergence develop within the synoptic circulation, the pressure will change in accordance with the pressure tendency equation. The pressure changes will be magnified if the appropriately signed kinematic divergence is phased with the appropriately signed density advection. Thus, kinematic convergence and cold advection will tend to produce large pressure rises over an area.

The resulting pressure changes will initiate the development of an isallobaric circulation which is on a smaller scale than the original sub-synoptic scale divergence production.

The new mesoscale circulation will, in turn, generate its own areas of rapid divergence production in the areas of appropriate mass and momentum distributions.

This sequence is hypothesized to continue down to the micro-scale where the multi-scale organization of the superposition of potential instability and low level convergence is sufficient to generate large quantities of vertical momentum and kinetic energy which create the tornado or severe thunderstorm circulations.

The dynamical details of this process are described in Paine et al. (1978). However, in summary, each scale of circulation is forced by the convergence/divergence production at the preceding larger scale. The circulation development is accomplished through the isallobaric wind derived from the changing pressure distribution forced by the fluid's mass divergence/convergence.

If this sequence is correct, a series of nested grid numerical primitive equation models initialized in the areas determined by the maximum convergence tendency superimposed on the maximum potential instability should be able to simulate the spatial and temporal organization of intense convective storms. This system has the advantage of beginning with the available large scale data and allowing the data to dictate where higher frequency waves will develop. Thus, high resolution spatial and temporal data are not absolutely necessary for its implementation. This alleviates one of the primary problems of severe local storm forecasting. Secondly, the simulation experiments will probably reveal a great deal about the nature of the physical processes which are responsible for the development of severe local storms.

The first version of such a forecast model is described in the next section.

TRADITIONAL U.S. USAGE	TIME SCALE SPACE SCALE	ONE MONTH	ONE WEEK	ONE DAY	ONE HOUR	ONE MINUTE	ORLANSKI'S PROPOSED DEFINITION
PLANETARY SCALE		Ultra Long Waves					MACRO α SCALE
SYNOPTIC SCALE	10000 km		Quasi- Geostrophic Waves				MACRO β SCALE
MESO SCALE	1000 km			Fronts and Hurricanes			MESO α SCALE
	100 km				Squall Lines		MESO β SCALE
	10 km				Inertial Waves Mtn. and Lake Effect		MESO γ SCALE
MICRO SCALE	1 km				Thunder- storms C. A. T. Urban Effects		MICRO α SCALE
	100 m				Tornadoes Short Gravity Waves		MICRO β SCALE
	10 m				Dust Devils Thermals Wakes		

Figure 1-1. The hydrodynamic spectrum and the atmospheric circulation systems which are characteristic of each of its divisions. (Adapted from Orlanski, 1975)

Table 1. The primitive equation set consisting of the conservation laws for momentum, mass, energy and moisture.

	<u>Internal Source/Sink Terms</u>	<u>External S/S Terms</u>	
a. Conservation of momentum			
	$-\frac{1}{\rho} \frac{\partial p}{\partial x} + fv$	$+F_x$	(1)
	$-\frac{1}{\rho} \frac{\partial p}{\partial y} - fu$	$+F_y$	(2)
	$-\frac{1}{\rho} \frac{\partial p}{\partial z} - g + \lambda u$	$+F_z$	(3)
b. Conservation of mass			
	$-\rho (\frac{\partial u}{\partial x} + \frac{\partial v}{\partial y} + \frac{\partial w}{\partial z})$	$+\rho_{\text{flux}}$	(4)
c. Conservation of energy*			
	$-\frac{RT}{C_v} (\frac{\partial u}{\partial x} + \frac{\partial v}{\partial y} + \frac{\partial w}{\partial z})$	$+T_{\text{diabatic}}$	(5)
d. Conservation of moisture			
	$-\rho_v (\frac{\partial u}{\partial x} + \frac{\partial v}{\partial y} + \frac{\partial w}{\partial z})$	$+\rho_v \text{flux}$	(6)
e. Ideal gas law, defines pressure in terms of density, temperature and the specific gas constant, R.			
	$p = \rho RT$		(7)

*Note: To suggest the parallelism between the three conservation laws, the three-dimensional velocity divergence in (5) has been substituted for the adiabatic term.

Table 2. The two-dimensional divergence and vorticity theorems
and the pressure tendency equation.

a. Two-dimensional Divergence Theorem

$$\frac{dD}{dt} = -D^2 + f\zeta - \left[\frac{\partial w}{\partial x} \frac{\partial u}{\partial z} + \frac{\partial w}{\partial y} \frac{\partial v}{\partial z} \right] - \left[\frac{\partial \alpha}{\partial x} \frac{\partial p}{\partial x} + \frac{\partial \alpha}{\partial y} \frac{\partial p}{\partial y} \right] \quad (8)$$

$$-2 \left[\frac{\partial u}{\partial y} \frac{\partial v}{\partial x} - \frac{\partial u}{\partial x} \frac{\partial v}{\partial y} \right] - \alpha \left[\frac{\partial^2 p}{\partial x^2} + \frac{\partial^2 p}{\partial y^2} \right] - u \frac{\partial f}{\partial y} + \left[\frac{\partial F_x}{\partial x} + \frac{\partial F_y}{\partial y} \right]$$

$$\text{where: } D = \frac{\partial u}{\partial x} + \frac{\partial v}{\partial y} = \nabla \cdot \vec{V}$$

$$\zeta = \frac{\partial v}{\partial x} - \frac{\partial u}{\partial y}$$

$$\alpha = \frac{1}{\rho}$$

$$\nabla = \frac{\partial}{\partial x} \hat{i} + \frac{\partial}{\partial y} \hat{j} \text{ (2-D del operator)}$$

$$J(u, v) = \left[\frac{\partial u}{\partial y} \frac{\partial v}{\partial x} - \frac{\partial u}{\partial x} \frac{\partial v}{\partial y} \right]$$

b. Two-dimensional Vorticity Theorem

$$\frac{d\zeta}{dt} = - (f + \zeta) D - \left[\frac{\partial \alpha}{\partial x} \frac{\partial p}{\partial y} - \frac{\partial \alpha}{\partial y} \frac{\partial p}{\partial x} \right] - \left[\frac{\partial w}{\partial x} \frac{\partial v}{\partial z} - \frac{\partial w}{\partial y} \frac{\partial u}{\partial z} \right] \quad (9)$$

$$-v \frac{\partial f}{\partial y} + \left[\frac{\partial F_x}{\partial x} - \frac{\partial F_y}{\partial y} \right]$$

c. Pressure Tendency Equation

$$\left(\frac{\partial p}{\partial t} \right)_h = -g \int_h^\infty \rho \left(\frac{\partial u}{\partial x} + \frac{\partial v}{\partial y} \right) dz - g \int_h^\infty \left(u \frac{\partial p}{\partial x} + v \frac{\partial p}{\partial y} \right) dz - (gpw)_h \quad (10)$$

velocity convergence density advection vertical
mass flux

where h = elevation ($w=0$ at $h=0$) above surface.

2.0 Structure of the Primitive Equation Model System

The complete numerical-dynamical system required to simulate the entire hypothesized cascade sequence through the microscale consists of a set of sequentially nested primitive equation models formulated in an x,y,z,t coordinate system. The physics employed in each model will ultimately depend upon the physical effects found to be significant at each scale. The initial model in the sequence has a horizontal grid mesh of 38 km or about 1/4 the size of the LFM2 horizontal grid and 12 vertical levels. At present, the data for this model is interpolated from objectively analyzed constant pressure surface data supplied by National Meteorological Center (NMC) through the Bureau of Reclamation. Each successive model is then initialized at a point in space and time where the preceding larger scale model produced the maximum value of an index which incorporates the meteorological parameters (e.g. equivalent hydrostatic stability, convergence tendency, low level moisture content) considered necessary for the development of circulation at smaller scales. The grid mesh at each successive nesting is generally reduced by a factor of 1/2. The initialization of the nested models is accomplished through linear interpolation of the large scale model forecast.

However, during the 60 day test in the spring of 1978, the computer and communications resources available constrained the model test to be conducted through the use of only the 38 km model. Thus, only the sub-synoptic and mesoscale potential for convective development could be assessed during the test period. A significant

improvement in the forecast of the timing, location and intensity of convective development is expected when a greater portion of the model sequence can be employed in the generation of the forecast.

The details of the 38 km model used during the spring 1978 test period are presented in the following subsections.

2.1 Model Equations

The model includes prognostic equations for the water vapor mixing ratio (Q), the potential temperature (θ), the north-south (v) and east-west (u) wind components and the pressure tendency at the base of the model (P_b):

$$\frac{\partial Q}{\partial t} = -m(u \frac{\partial Q}{\partial x} + v \frac{\partial Q}{\partial y}) - w \frac{\partial Q}{\partial z} + Q_C + Q_E + Q_F \quad (11)$$

where Q_C is the loss of water vapor by condensation, Q_E is the gain of water vapor by evaporation and Q_F is the surface flux of water vapor, $Q_C = Q_E = Q_F = 0$ in the 38 km version of the model;

$$\frac{\partial \theta}{\partial t} = -m(u \frac{\partial \theta}{\partial x} + v \frac{\partial \theta}{\partial y}) - w \frac{\partial \theta}{\partial z} + \theta_D + \theta_F \quad (12)$$

where θ_D is the diabatic heating and θ_F is the surface flux of sensible heat and are both zero in the 38 km model;

$$\frac{\partial u}{\partial t} = -m(u \frac{\partial u}{\partial x} + v \frac{\partial u}{\partial y}) - w \frac{\partial u}{\partial z} - \alpha \frac{\partial P}{\partial x} + fv + F_x \quad (13)$$

where F_x represents the surface frictional stress and is set equal to zero in this model;

$$\frac{\partial v}{\partial t} = -m(u \frac{\partial v}{\partial x} + v \frac{\partial v}{\partial y}) - w \frac{\partial v}{\partial z} - \alpha \frac{\partial P}{\partial y} - fu + F_y \quad (14)$$

where F_y represents the surface frictional stress and is set equal to zero in the current model;

$$\frac{\partial P_b}{\partial t} = -g \int_{z_b}^Z t m(u \frac{\partial \rho}{\partial x} + v \frac{\partial \rho}{\partial y}) dz - g \int_{z_b}^Z t m(\frac{\partial u}{\partial x} + \frac{\partial v}{\partial y}) w_z dz + g \rho w_b \quad (15)$$

where w_b is the vertical velocity at the base of the model is zero.

The model diagnostic equations include the ideal gas law,

$$\rho = \frac{P}{RT_v} \quad (16)$$

where T_v is the virtual temperature defined by $T_v = T(1+0.61Q)$, ρ is the density and R is gas constant for dry air; the hydrostatic equation,

$$\frac{\partial P}{\partial z} = -\rho g \quad (17)$$

the definition of potential temperature,

$$\theta = T \left(\frac{P_o}{P} \right)^\kappa \quad (18)$$

where $P_o = 1000.0$ mb and $\kappa = 0.286$; and the continuity equation with $\partial \rho / \partial t = 0$,

$$\frac{\partial w}{\partial z} = -m \left(\frac{\partial u}{\partial x} + \frac{\partial v}{\partial y} \right) - m \left(\frac{u}{\rho} \frac{\partial \rho}{\partial x} + \frac{v}{\rho} \frac{\partial \rho}{\partial y} \right) - \frac{w}{\rho} \frac{\partial \rho}{\partial z} \quad (19)$$

2.2 Vertical Structure

There are 12 vertical levels in the 38 km model. These are horizontal surfaces and no terrain effects are included. The vertical levels are 1150, 2275, 3400, 3875, 4550, 5100, 6000, 6750, 7650, 8625, 9750 and 11200 meters.

2.3 Initial Conditions

The initial data consists of the height, temperature and dew point at 190 km intervals on the 1000, 850, 700, 500, 400, 300, 250 and 200 mb surfaces. The dew point values are converted to mixing ratio values and the temperature is converted to potential temperature before the data is vertically interpolated to obtain the values for pressure, potential temperature and mixing ratio on the z surfaces at 190 km intervals. A horizontal linear interpolation is then employed to obtain the values of P, θ and Q at 38 km intervals.

The initial horizontal momentum field is assumed to be in geostrophic equilibrium so that the initial u and v wind components are given by:

$$u = - \frac{\alpha}{f} \frac{\partial P}{\partial y} \quad \text{and} \quad v = + \frac{\alpha}{f} \frac{\partial P}{\partial x} \quad (20)$$

The initial specific volume ($\alpha = 1/\rho$) or density (ρ) distribution is determined from the pressure and temperature distribution through the ideal gas law.

The initial vertical motion (w) is assumed to be zero.

2.4 Space Differencing Scheme

A sixth order space differencing scheme is employed for horizontal derivatives and has the general form:

$$\begin{aligned} \frac{\partial \epsilon}{\partial x} \approx & \frac{1}{60\Delta x} (45.0(\epsilon_{i+1,j,k} - \epsilon_{i-1,j,k}) - 9.0(\epsilon_{i+2,j,k} - \epsilon_{i-2,j,k}) \\ & + 1.0(\epsilon_{i+3,j,k} - \epsilon_{i-3,j,k}) \end{aligned} \quad (21)$$

where i, j, k are the indices for the grid points in the x, y, z directions respectively and ϵ is any dependent variable.

Vertical derivatives are computed with a fourth order scheme which has the form:

$$\frac{\partial \epsilon}{\partial z} \approx \frac{1}{12\Delta z} [8.0 (\epsilon_{i,j,k+1} - \epsilon_{i,j,k-1}) - 1.0 (\epsilon_{i,j,k+2} - \epsilon_{i,j,k-2})]. \quad (22)$$

However, a second order differencing scheme is used for vertical derivatives at levels 2 and 11:

$$\frac{\partial \epsilon}{\partial z} \approx \frac{1}{2\Delta z} [\epsilon_{i,j,k+1} - \epsilon_{i,j,k-1}]. \quad (23)$$

Simpson's rule is utilized for the integrated divergence calculations within the continuity equation to obtain the vertical velocities.

2.5 Time Differencing Scheme

The predictor-corrector (Euler Forward-Backward) time differencing scheme is employed. If ϵ is any of the five (Q, θ, u, v, P_b) prognostic variables and τ is the time level at which the spatial derivatives are computed, then the "first guess" field is obtained by extrapolating forward in time:

$$\epsilon^* = \epsilon^\tau + \frac{\partial \epsilon}{\partial t} (Q, \theta, u, v, P_b) \Delta t \quad (24)$$

The field at time $\tau+1$ is then obtained by using the "guess" field to recompute the tendencies and then again extrapolating forward in time from the original time level τ :

$$\epsilon^{T+1} = \epsilon^T + \frac{\partial c}{\partial t} (Q^*, \theta^*, u^*, v^*, P_b^*) \Delta t \quad (25)$$

The time increment is 60 seconds for the 38 km model based on Courant Number ≈ 1 .

2.6 Smoother

A sixth order smoother is used on the dependent variables every ten time steps. If c is any dependent variable, the smoother has the form:

$$\begin{aligned} \epsilon_{i,j,k} = & \epsilon_{i,j,k} + [.1171875 * (\epsilon_{i+1,j,k} + \epsilon_{i-1,j,k} + \epsilon_{i,j+1,k} + \epsilon_{i,j-1,k}) \\ & - .0468750 * (\epsilon_{i+2,j,k} + \epsilon_{i-2,j,k} + \epsilon_{i,j+2,k} + \epsilon_{i,j-2,k}) \\ & + .0078125 * (\epsilon_{i+3,j,k} + \epsilon_{i-3,j,k} + \epsilon_{i,j+3,k} + \epsilon_{i,j-3,k}) \\ & - .3125 * \epsilon_{i,j,k}] \end{aligned} \quad (26)$$

2.7 Lateral Boundary Conditions

The lateral boundary conditions listed below are applied to Q, θ, u, v and P and to Q^*, θ^*, u^*, v^* and P^* . Once again c is used to designate any dependent variable. The notation i_m, j_m refers to the last row and column of the model grid.

For Southern Rows

$\epsilon_{i,3} = \epsilon_{i,4}$	Row 3
$\epsilon_{i,2} = \epsilon_{i,3}$	Row 2
$\epsilon_{i,1} = \epsilon_{i,2}$	Row 1

For Northern Rows

$$\epsilon_{i,jm-2} = \epsilon_{i,jm-3} \quad \text{Row } jm-2$$

$$\epsilon_{i,jm-1} = \epsilon_{i,jm-2} \quad \text{Row } jm-1$$

$$\epsilon_{i,jm} = \epsilon_{i,jm-1} \quad \text{Row } jm$$

For Western Columns

$$\epsilon_{3,j} = \epsilon_{4,j} \quad \text{Column 3}$$

$$\epsilon_{2,j} = \epsilon_{3,j} \quad \text{Column 2}$$

$$\epsilon_{1,j} = \epsilon_{2,j} \quad \text{Column 1}$$

For Eastern Columns

$$\epsilon_{im-2,j} = \epsilon_{im-3,j} \quad \text{Column } im-2$$

$$\epsilon_{im-1,j} = \epsilon_{im-2,j} \quad \text{Column } im-1$$

$$\epsilon_{im,j} = \epsilon_{im-1,j} \quad \text{Column } im$$

Vertical Boundary Conditions on w:

$$w_{z_t} = 0$$

$$w_{z_b} = 0$$

3.0 Selected Examples of Model Performance

The presentation of several examples of the model's performance during the spring 1978 test period is designed to illustrate the model's predictive ability as well as provide a partial understanding of the deficiencies in the model and the initial data which prevented the system from achieving a better forecast of the actual events.

The real time output of the model was limited to an index which consisted of the low level equivalent static stability multiplied by the low level mass convergence and transformed to a scale from 0 to 10. This index was printed every thirty minutes of model time. Several modifications in the original index were made during the course of the test. These indices are similar to the one which will ultimately be used to a 19 km grid model in the next phase of the model development.

During the test period, it was noted that the development of convection was closely aligned to the time when areas of low level convergence became superimposed upon regions of large potential instability. This, of course, is not an extremely shocking observation, but it does provide a framework for comparing the model forecast fields with the observed convective development. Thus, much of the presentation of the individual cases will be formulated to illustrate the model's development of low level convergence in proximity to zones of large potential instability. A discussion of the dynamical processes responsible for the development of the low level convergence and potential instability will not be

included in the presentations. Thus, this is basically a presentation of what the model was simulating rather than how it was doing it.

There appears to be three areas of problems which noticeably affected the forecasts during the 60 day test.' A brief description of each, at this point, will alert the reader to its existence as the cases are presented.

- (1) The area of x,y space integration ($\approx 2400 \times 2000$ km) was insufficient to fully capture the advective processes associated with the synoptic scale waves. That is, only a portion of the synoptic scale wave could, in general, be represented within the model domain. This often lead to a situation in which a well simulated mesoscale flow field is superimposed upon a slowly degrading macroscale field. In a relatively short time, this will create new mesoscale fields which are misforecasted. Several times mesoscale zones of low level convergence and large potential instability developed in the appropriate space-time position early in the model forecast, but subsequently failed to move (usually eastward) with the proper speed. This was primarily due to the lack of a model simulation of the synoptic scale advective processes. However, in cases which featured slowly changing advective or isallobaric patterns at the synoptic scale or rapidly changing subsynoptic patterns, the 38 km model appeared to capture the mesoscale nonlinear interactions with reasonable fidelity.

- (2) The low level initial data over the western Plains and Rocky Mountain region did not adequately represent the low level atmospheric structure. This problem was a result of the necessity to construct fictitious atmospheric columns downward to the 850 and 1000 mb surfaces in regions of high surface elevation. The NMC method of "building down" did not generate an adequate representation of the low level structure in these areas. The build-down used in constructing the data allowed the temperature and dew point fields in the lowest 2000 meters to possess anomalies of as much as 10° to 20°C on certain days. The effect of these bogus moisture fields was particularly devastating in the western Plains, where unrealistically high moisture values led to predicted potential instability which was inconsistent with reality. Also, the pressure gradients established in the initial data because of the fictitious thermal build down helped to amplify zones of fictitious convergence in the same region as the misspecified stability field.
- In addition, there were days on which the NMC analysis data was not completely consistent with the data taken directly from the radiosonde observations. The explanation for this discrepancy has not been ascertained.

(3) There was only a fair representation of the low level atmospheric structure contained within the model. This was due to the fact that the model had only two levels (1150, 2275 meters) in the critical volume below 3000 meters. Since it is in this volume that the isallobaric response is maximized, the development of the isallobarically forced low level convergence and moisture transport was not completely resolved by the model. However, since the initial data was received only on the 1000 mb, 850 and 700 mb surfaces, the low level structure of the atmosphere was not well resolved in the initial data. This is especially true if one recalls that the 1000 mb and in some areas, the 850 mb data represents fictitious "build-downs" of data from the observed vertical distributions of temperature and dew point above these points.

Despite these difficulties, the model appears to have captured the essence of the mesoscale organization of low level convergence and potential instability in most cases.

The six cases presented in the following subsections were chosen to illustrate the performance of the model under a variety of large scale dynamical conditions.

The 14 April case represents an isolated moderate intensity convective outbreak occurring within a weak synoptic scale feature.

The 29 April and 18 May cases illustrate a slightly more widespread, moderately strong convective outbreak associated with a non-developing synoptic scale wave.

The 17 June case is characteristic of a relatively large and strong severe weather outbreak associated with an average late spring synoptic situation.

The 12 May and 17 April cases illustrate the model's performance during the occurrence of a relatively strong springtime synoptic cyclogenesis. Both of these cases produced multi-squall line extensive severe weather outbreaks.

3.1 Case 1: 14 April 1978

An area of widely scattered moderately strong convective activity developed over western Oklahoma and southwestern Kansas during the afternoon and evening of 14 April 1978. Although no tornadoes were reported, the NSSL severe weather observation van observed 1 3/4 inch hail in the vicinity of Altus, Oklahoma at approximately 8:30 p.m. CST (0230 GMT 15 April).

The 38 km model was initialized at 1200 GMT 14 April 1978 over the area shown in Figure 3-1. The dashed box within the model domain demarcates the area over which objectively analyzed plots of the model forecast fields were printed for illustrative purposes. This region is 1/4 the area of the entire model domain and allows a better visual representation of the mesoscale structure forecasted by the model.

The surface weather map at 1200 GMT (Figure 3-2a) revealed the presence of a weak Rocky Mountain lee trough from western Kansas southward to western Texas. A warm front was analyzed from this trough eastward across southern Kansas, while a cold front was diagnosed along the trough axis from western Kansas to the Texas panhandle. The southerly flow to the east of the cold front and south of the warm front was only moderately moist. Surface dew points were near 50°F (10°C, 283°K) across most of Oklahoma and Texas. The air to the west of the cold front was dry with surface dew points below 30°F (-1°C, 272°K). Thus, as is frequently the case, the lee trough divided the cool dry continental air to the west from the warmer, more moist maritime tropical air to the east.

The 1200 GMT NMC analysis data (Figure 3-3) for the 1000 mb surface also indicates the presence of the lee trough pressure

topography. However, the 1000 mb dew point field defines a pattern which is rather unrealistic over the Western Plains and Rocky Mountain regions. For example, dew points near 299°K (26°C, 70°F) at 1000 mb are placed over northwestern Colorado where the surface dew points are near 30°F (-1°C, 272°K).

The 1200 GMT 850 mb data (Figure 3-3b) implies a substantial southerly geostrophic flow across most of the Southern Plains. There is evidence of the lee trough in eastern Colorado and eastern New Mexico. High dew points are placed to the east of the lee trough in west central Texas and in western Colorado. Another area of high dew points is placed over the Central Plains. Very dry 850 mb air extends from Central New Mexico northeastward to western Kansas.

The 1150 meter level model initialization of pressure and mixing ratio is presented in Figure 3-4. The initial pressure field indicates southwest geostrophic winds of about 25 knots over western Texas and Oklahoma. Mixing ratio values in excess of 4 g/kg are initialized over west central Texas and the Central Plains, while fictitious values near 10 g/kg are initialized in the Rocky Mountain region.

Figure 3-5 presents a time sequence of the forecasted pressure, wind vectors, divergence and mixing ratio at 1150 m and σ_E values centered at 2275 m. The fields are presented at 3 hour intervals except for hourly displays of σ_E and divergence near the time of convective development. The National Weather Service radar summaries during this period are also presented in Figure 3-5.

The most noteworthy events during the first nine hours of the model forecast are the northward transport of moisture into

western Oklahoma and the increasing easterly component of momentum over eastern Oklahoma. The low level moisture transport is also reflected in the σ_E field as a northward protrusion of low σ_E values. The westward edge of the easterly momentum is also an area of convergence.

By 9 hours (2100 GMT) into the forecast, a zone of potential instability is present over western Oklahoma with an area of convergence propagating westward at the leading edge of the easterly momentum. In addition, an increase in the negative v wind component over western Kansas and eastern Colorado has organized an east-west band of convergence in the northwest corner of the display area.

During the 9 to 12 hour period, the u convergence zone ($\nabla \cdot \vec{V}$ dominated by a negative $\partial u / \partial x$) continues to propagate eastward. At 13 hours into the forecast (0100 GMT) the u convergence zone is superimposed upon the north-south axis of low σ_E values over western Oklahoma. The 0135 GMT radar summary in Figure 3-6a indicates the existence of a few isolated 40,000 foot convective cells within the area defined by the model's superposition of minimum σ_E and low level convergence.

The model forecasts the v convergence wave ($\nabla \cdot \vec{V}$ dominated by negative $\partial v / \partial y$) to propagate to the south over the next three hours. By 15 hours (0300 GMT 15 April) into the forecast the eastern flank of the v wave is forecasted to intersect the westward propagating u wave just to the northwest of Gage, Oklahoma. The 0335 GMT radar summary indicates an area of growing cells to the northwest of Gage, Oklahoma. By 0535 GMT one of these cells has reached a radar height of 58,000 ft.

By 18 hours (0600 GMT) into the forecast the u wave has vanished and the dominant wave is the southwestward propagating v wave. However, only the extreme eastern portion of this wave of convergence is superimposed upon an area of appreciable potential instability. It is only in this area that substantial convective activity is observed.

The magnitude of the south-southwestward propagating v wave is probably overforecasted. This overforecasting is most likely related to the data build down problems associated with the high elevations in western Kansas and eastern Colorado.

In this case, the model's forecast of the superposition of potential instability and low level convergence was in good agreement with the observed spatial and temporal location of the meso-scale area of convective activity.

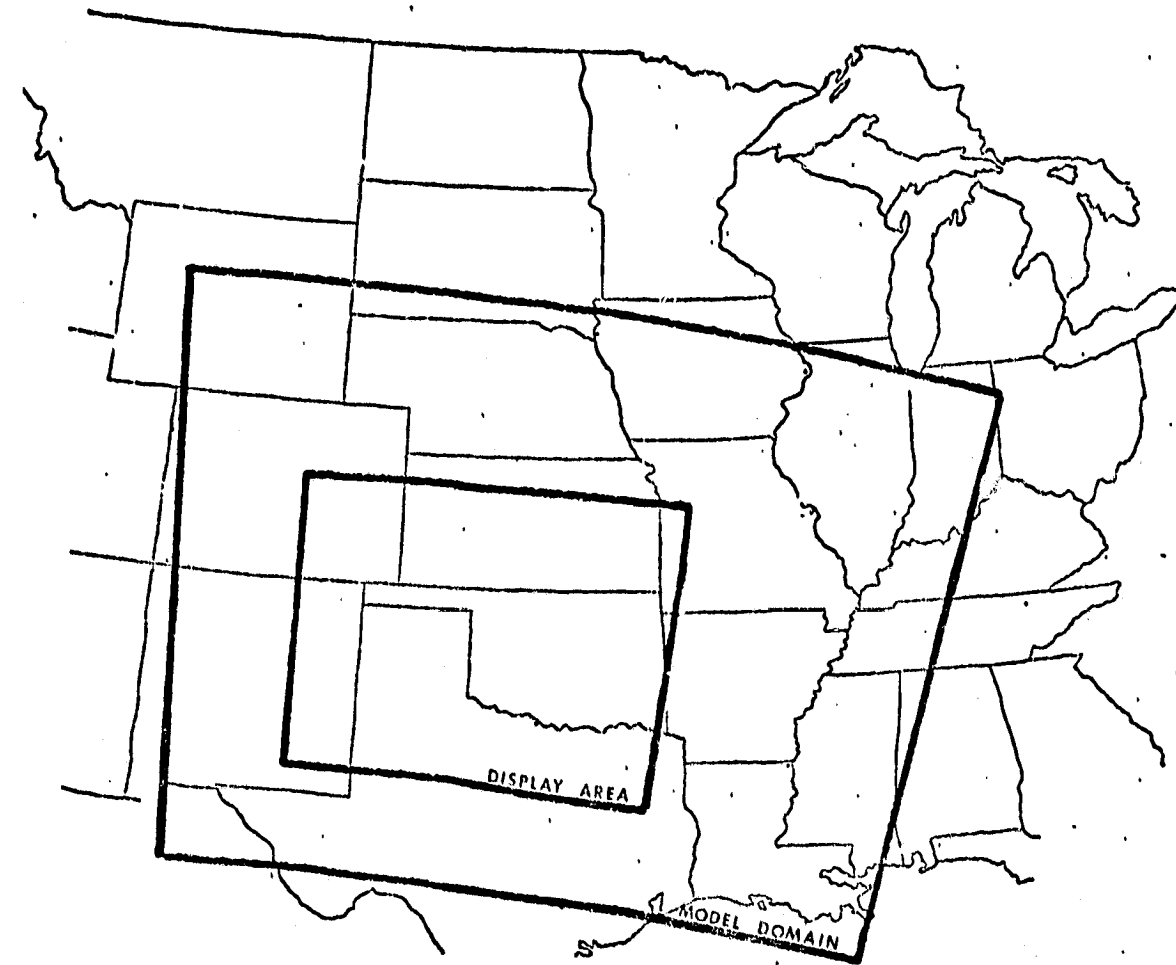


Figure 3-1. The model domain and forecast display area for the 14 April 1978 case. The large box indicates the horizontal domain of the 38 km model while the small box demarcates the region of display of the model forecast.

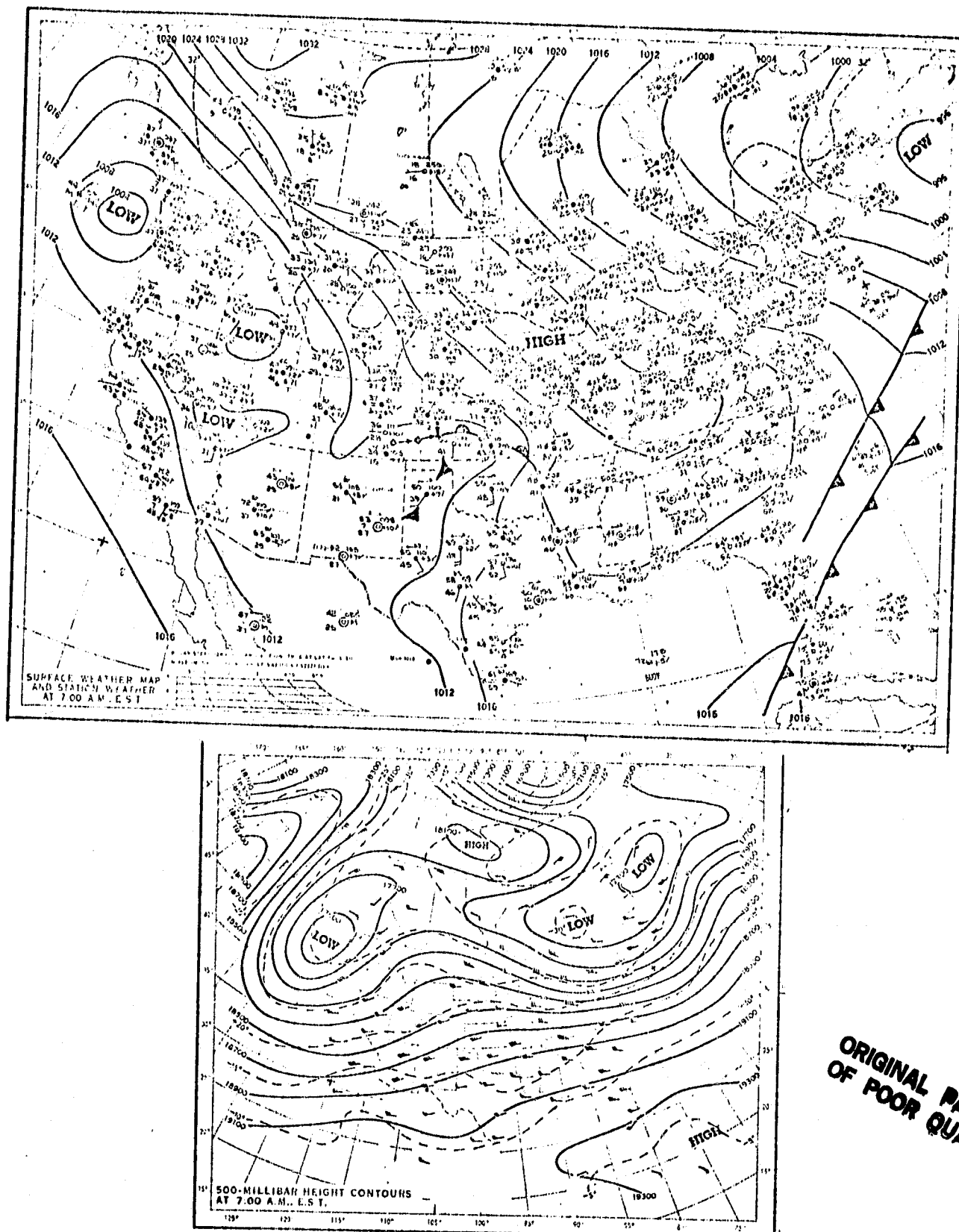


Figure 3-2a. Top: Surface weather map for 1200 GMT 14 April 1978.
 Bottom: 500 mb chart for 1200 GMT 14 April 1978.
 Height contours are labeled in feet.

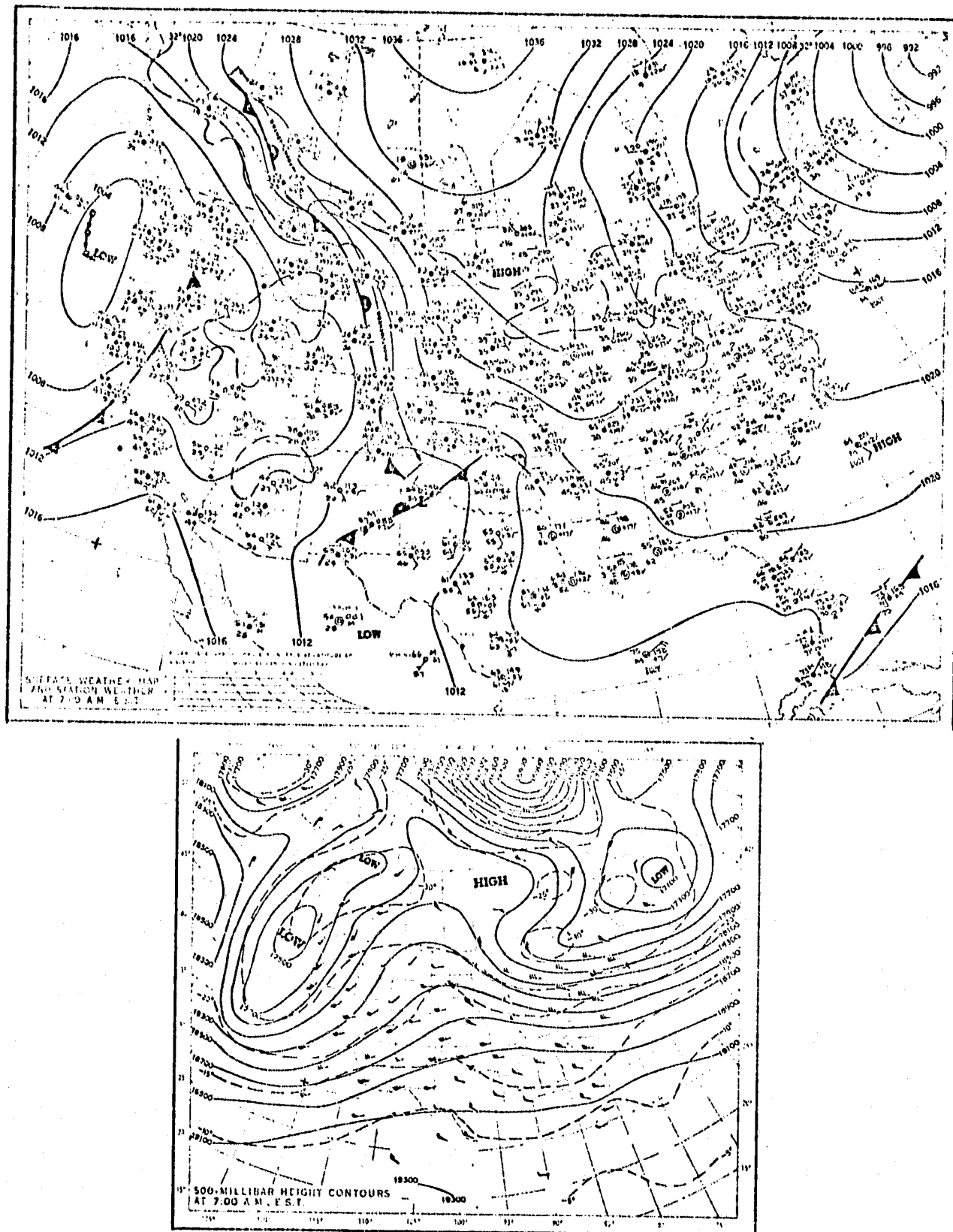


Figure 3-2b. Top: Surface weather map for 1200 GMT 15 April 1978.
 Bottom: 500 mb chart for 1200 GMT 15 April 1978.
 Height contours are labeled in feet.

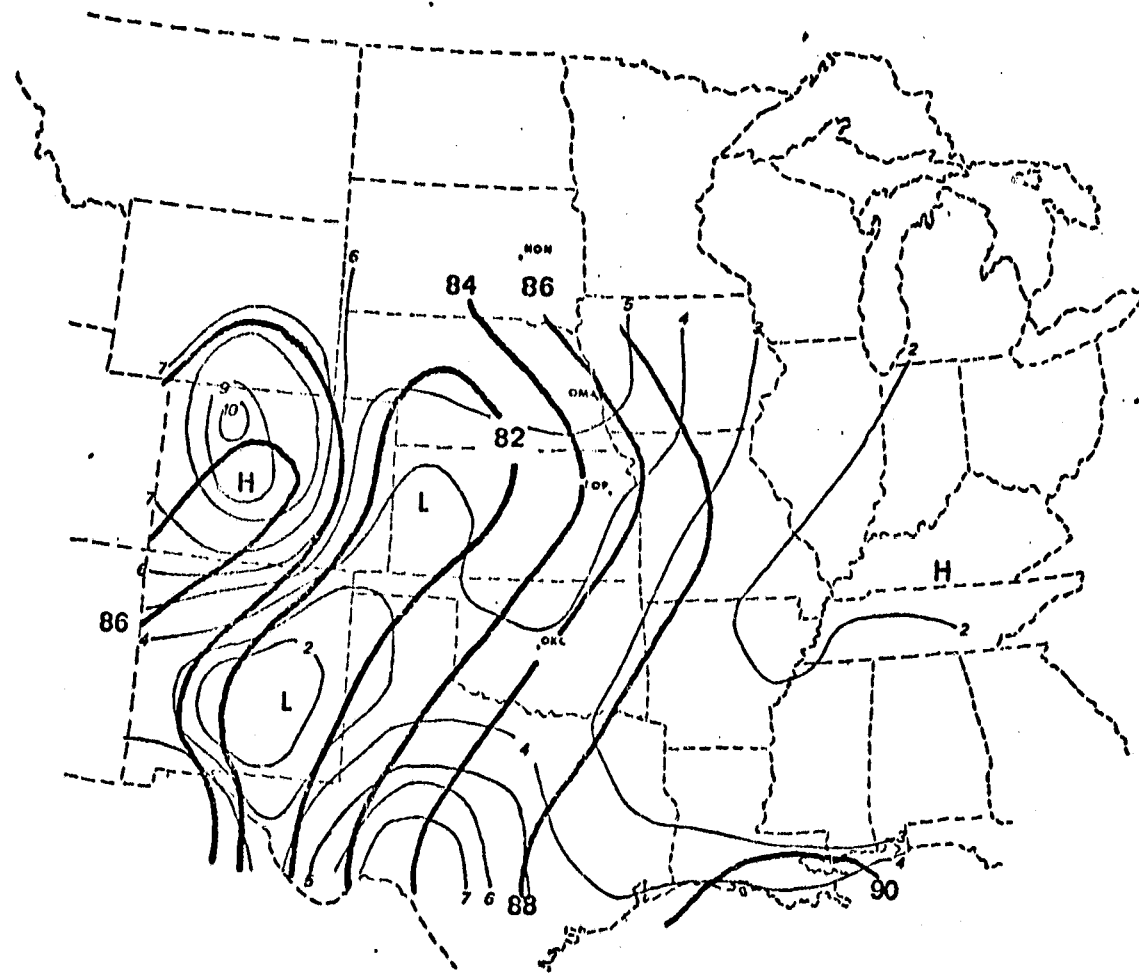


Figure 3-4. 38 km model 1150 m initialization of pressure and mixing ratio.
Bold lines are isobars at intervals of 2 mb. Labels omit the preceding 8. Light lines are mixing ratio in g/kg.

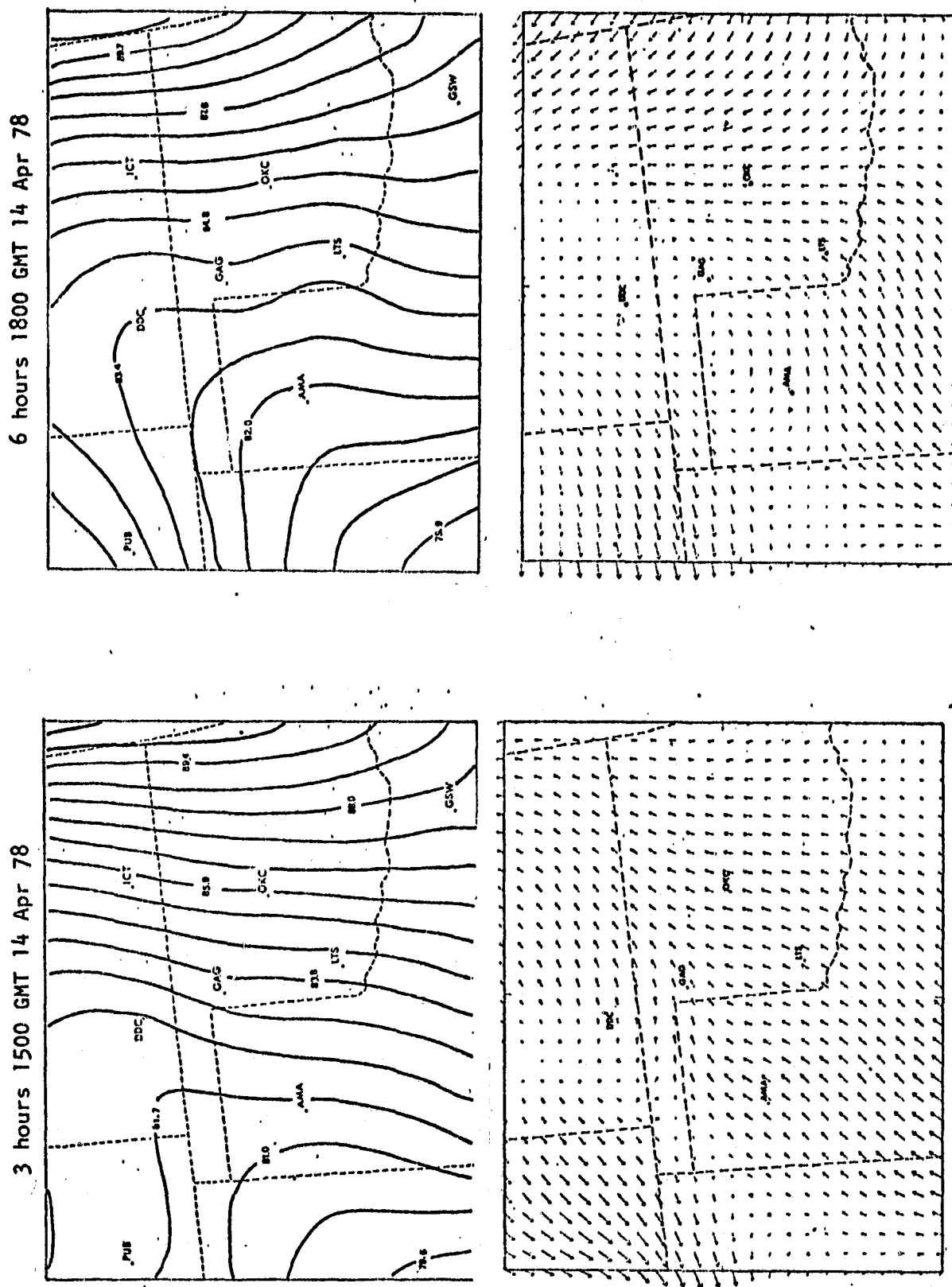


Figure 3-5a. Left: Three hour model forecast (1500 GMT 14 April) of the 1150 m pressure and wind vectors.
 Isobars are drawn at intervals of 0.7 mb. Pressure labels omit the preceding 8.
 Right: Six hour model forecast (1800 GMT 14 April) of the 1150 m pressure and wind vectors.

MARGINAL PAGE IS
OF POOR QUALITY

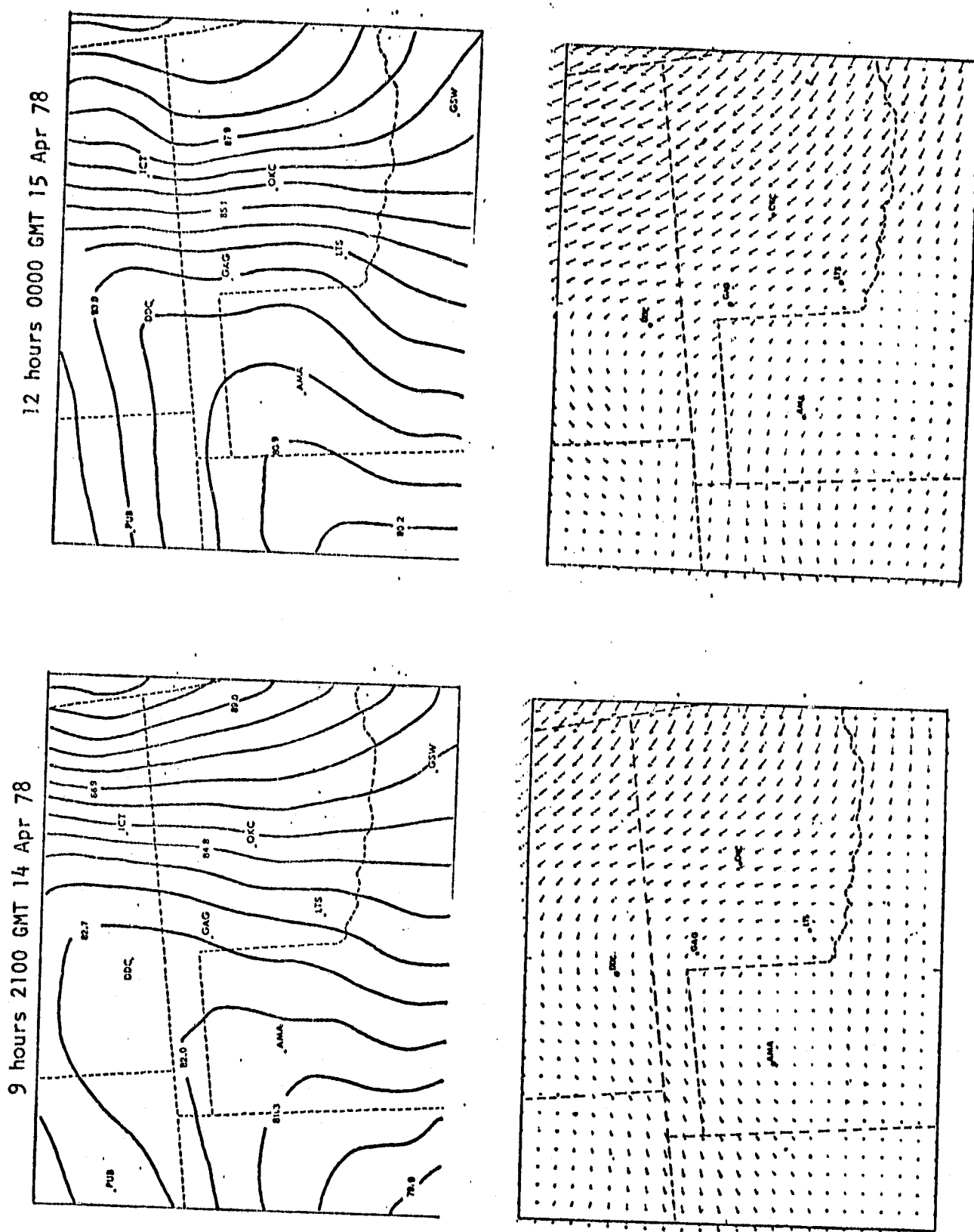


Figure 3-5b. Left: Nine hour forecast (2100 GMT 14 April) of the 1150 m pressure and wind vectors.
 Right: Twelve hour forecast (0000 GMT 15 April) of the 1150 m pressure and wind vectors.

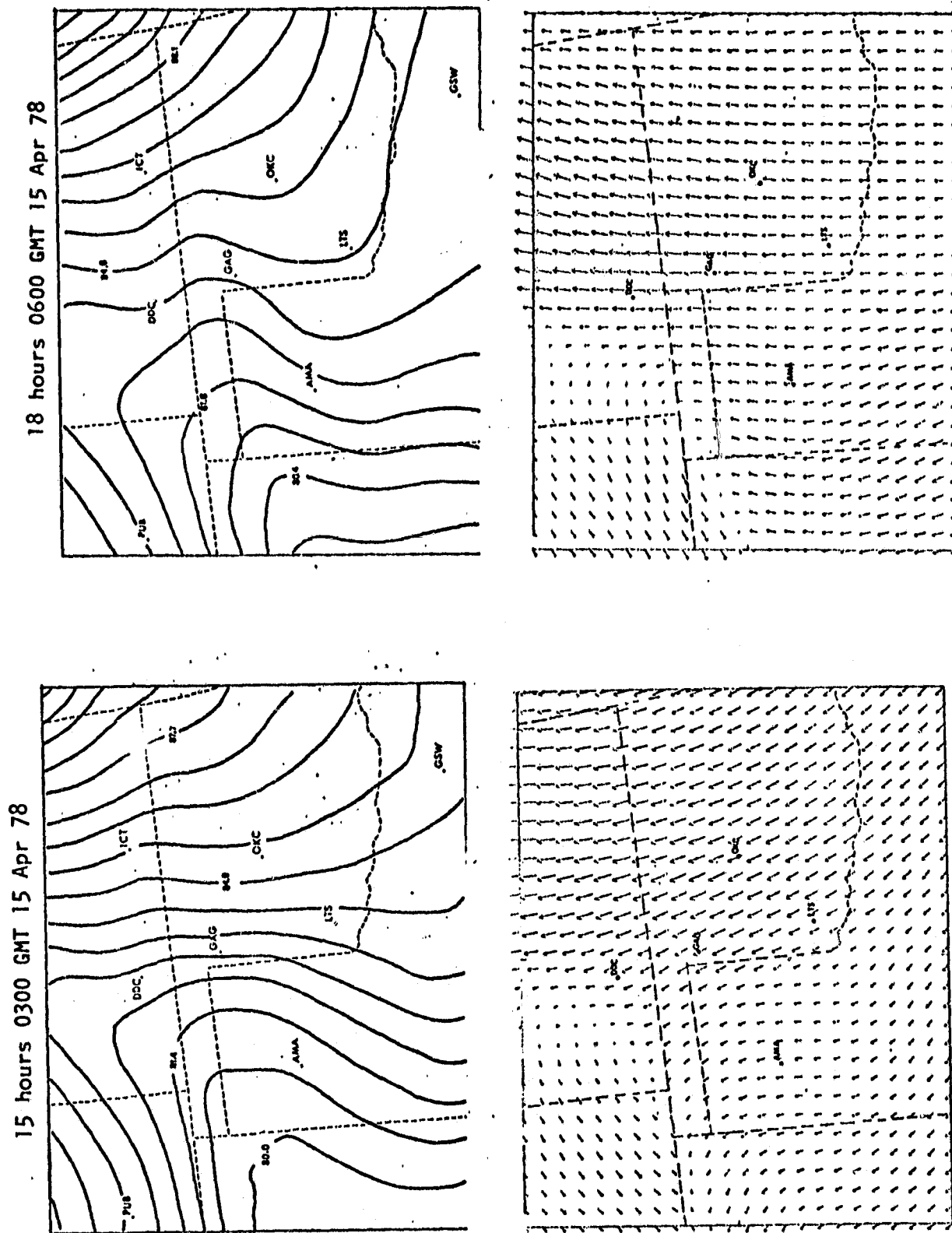
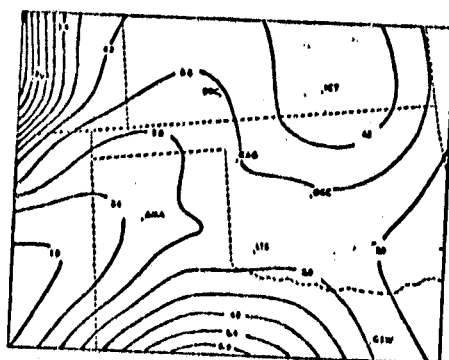


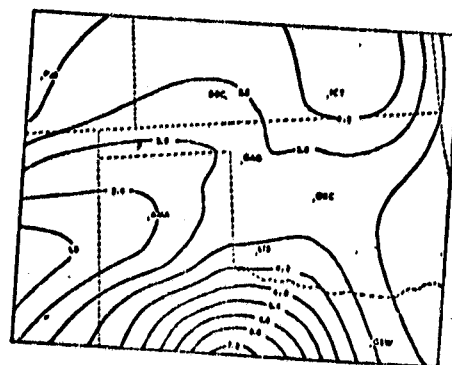
Figure 3-5c. Left: Fifteen hour forecast (0300 GMT 15 April) of the 1150 m pressure and wind vectors. Right: Eighteen hour forecast (0600 GMT 15 April) of the 1150 m pressure and wind vectors.

ORIGINAL PAGE IS
OF POOR QUALITY

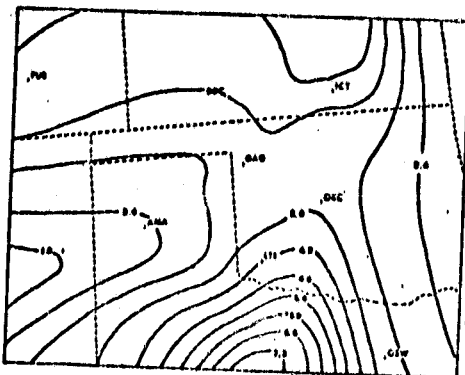
1500 GMT 14 April (3 hours)



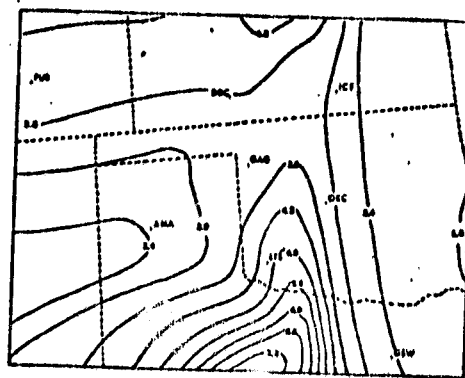
1800 GMT 14 April (6 hours)



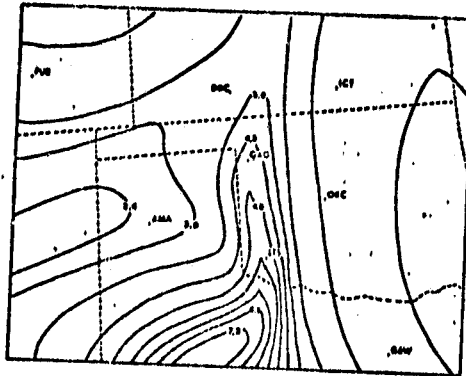
2100 GMT 14 April (9 hours)



0000 GMT 15 April (12 hours)



0300 GMT 15 April (15 hours)



0600 GMT 15 April (18 hours)

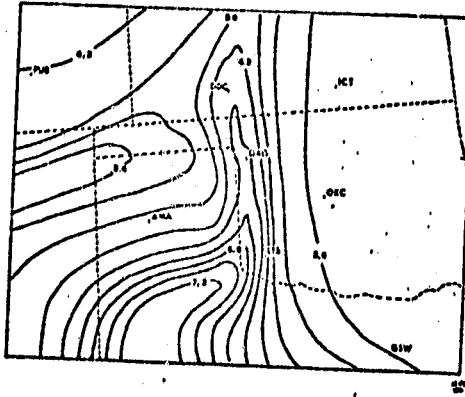


Figure 3-5d. Mixing ratio forecast at three hour intervals from 1500 GMT 14 April (3 hour forecast) to 0600 GMT 15 April (18 hour forecast). Isopleths are at intervals of 0.6 g/kg.

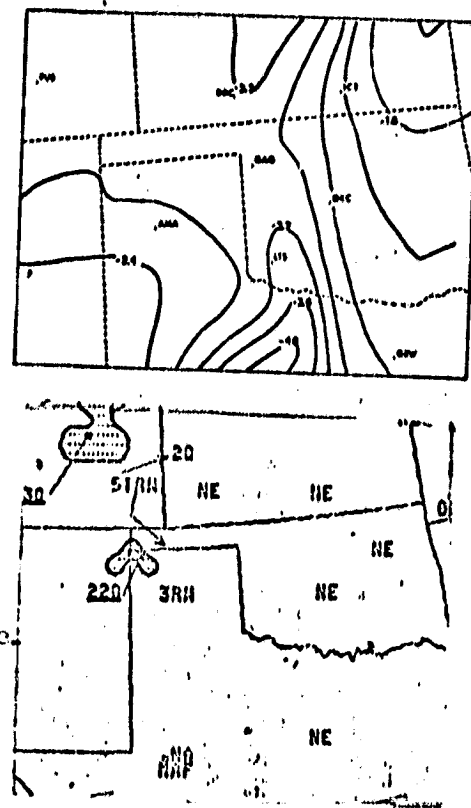
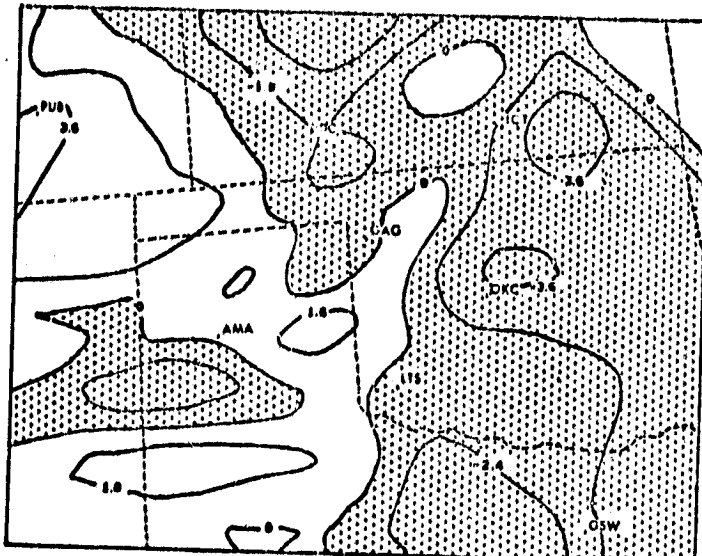


Figure 3-5e. Above: Nine hour forecast (2100 GMT 14 April) of the 1150 m divergence field. Stipple indicates convergence. Isopleths are at intervals of $1.8 \times 10^{-5} \text{ s}^{-1}$. Upper right: Nine hour forecast of the 2275 m σ_E field. Isopleths at intervals of 0.4. Lower right: National Weather Service radar summary for 2135 GMT 14 April.

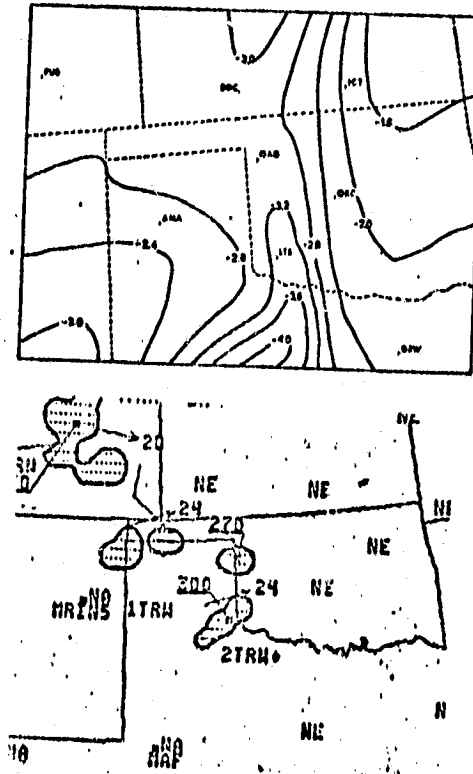


Figure 3-5f. Above: Twelve hour forecast (0000 GMT 15 April) of the 1150 m divergence field. Stipple indicates convergence. Isopleths at intervals of $1.6 \times 10^{-5} \text{ s}^{-1}$. Upper right: Twelve hour forecast of the 2275 m σ_E field. Lower right: National Weather Service radar summary for 2335 GMT 14 April.

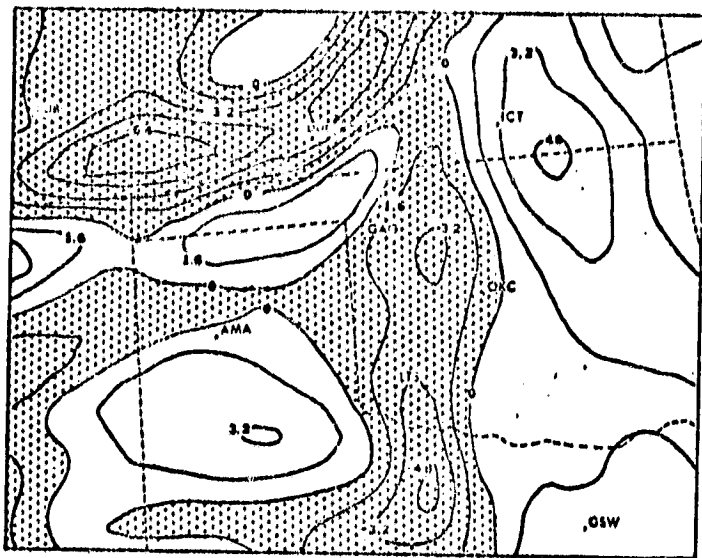


Figure 3-5g. Above: Thirteen hour forecast (0100 GMT 15 April) of the 1150 m divergence field. Stipple indicates convergence. Isopleths at intervals of $1.6 \times 10^{-5} \text{ s}^{-1}$.
 Upper right: Thirteen hour forecast of the 2275 m σ_E field.
 Lower right: National Weather Service radar summary for 0035 GMT 15 April.

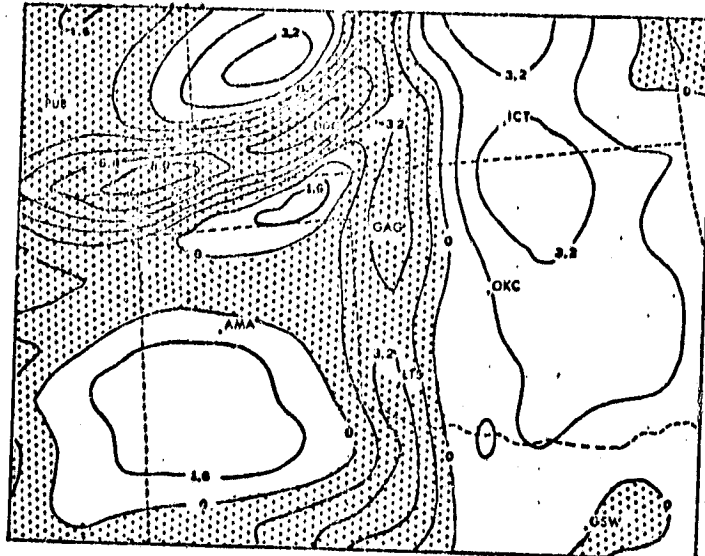
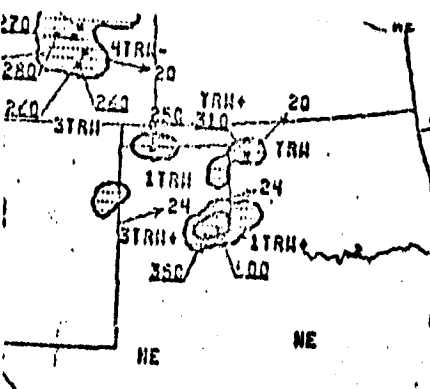
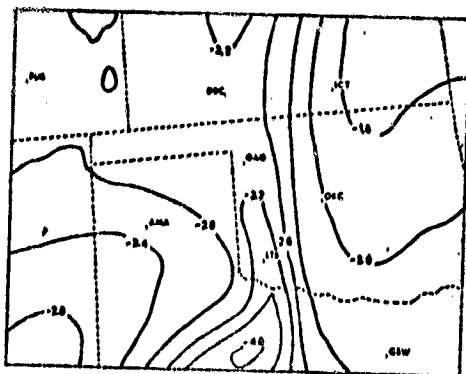


Figure 3-5h. Above: Fourteen hour forecast (0200 GMT 15 April) of the 1150 m divergence field. Stipple indicates convergence. Isopleths at intervals of $1.6 \times 10^{-5} \text{ s}^{-1}$.
 Upper right: Fourteen hour forecast of the 2275 m σ_E field.
 Lower right: National Weather Service radar summary for 0135 GMT 15 April.

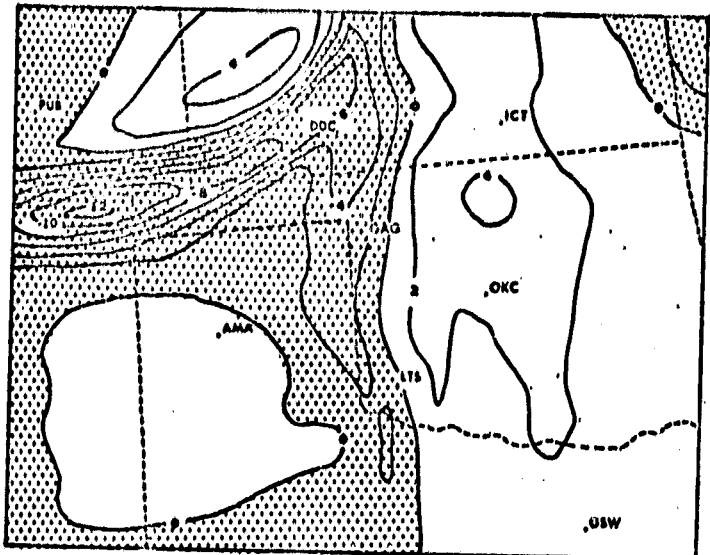


Figure 3-5i. Above: Fifteen hour forecast (0300 GMT 15 April) of the 1150 m divergence field. Stipple indicates convergence. Isopleths at intervals of $2 \times 10^{-5} \text{ s}^{-1}$.

Upper right: National Weather Service radar summary
for 0235 GMT 15 April

Lower right: National Weather Service radar summary
for 0335 GMT 15 April.

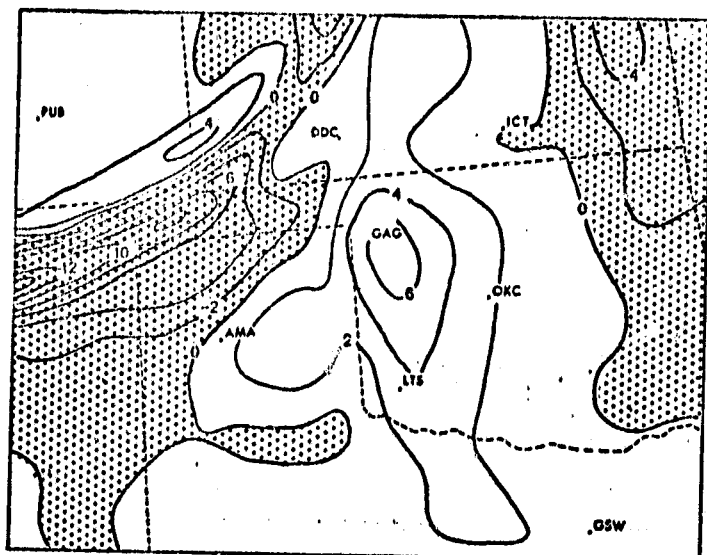
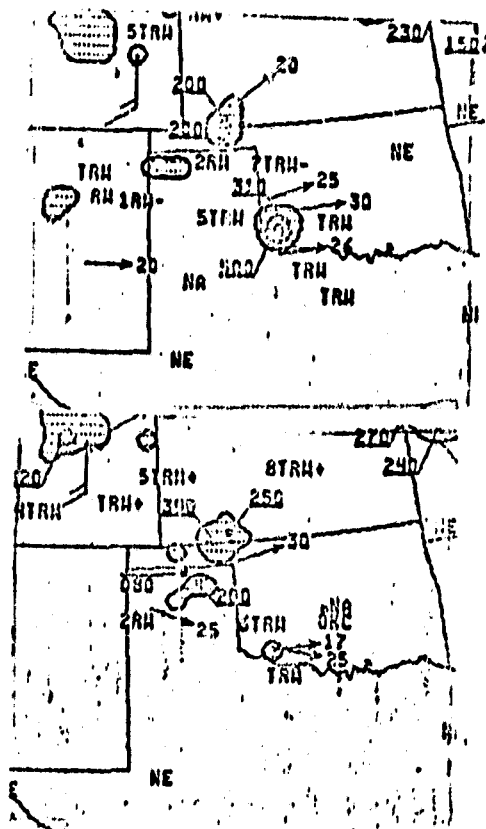
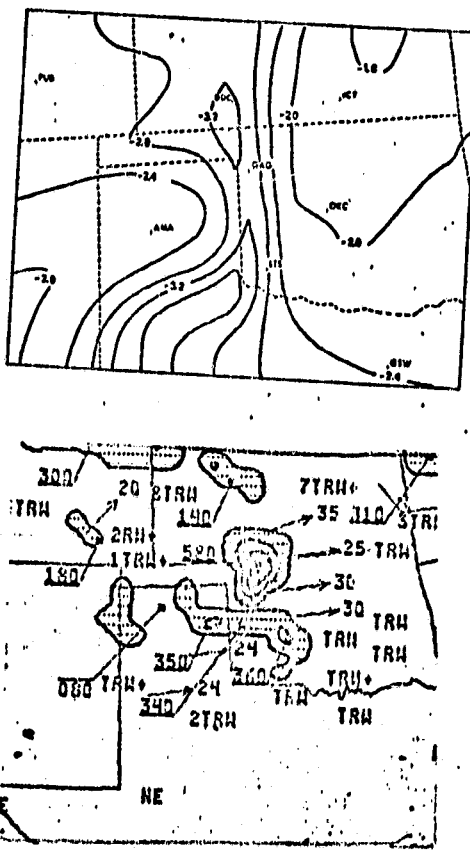


Figure 3-5j. Above: Eighteen hour forecast (0600 GMT 15 April) of the 1150 m divergence field. Stipple indicates convergence. Isopleths at intervals of $2 \times 10^{-5} \text{ s}^{-1}$.

Upper right: Eighteen hour forecast of the 2275 m σ_E field.

Lower right: National Weather Service radar summary for 0535 GMT 15 April.



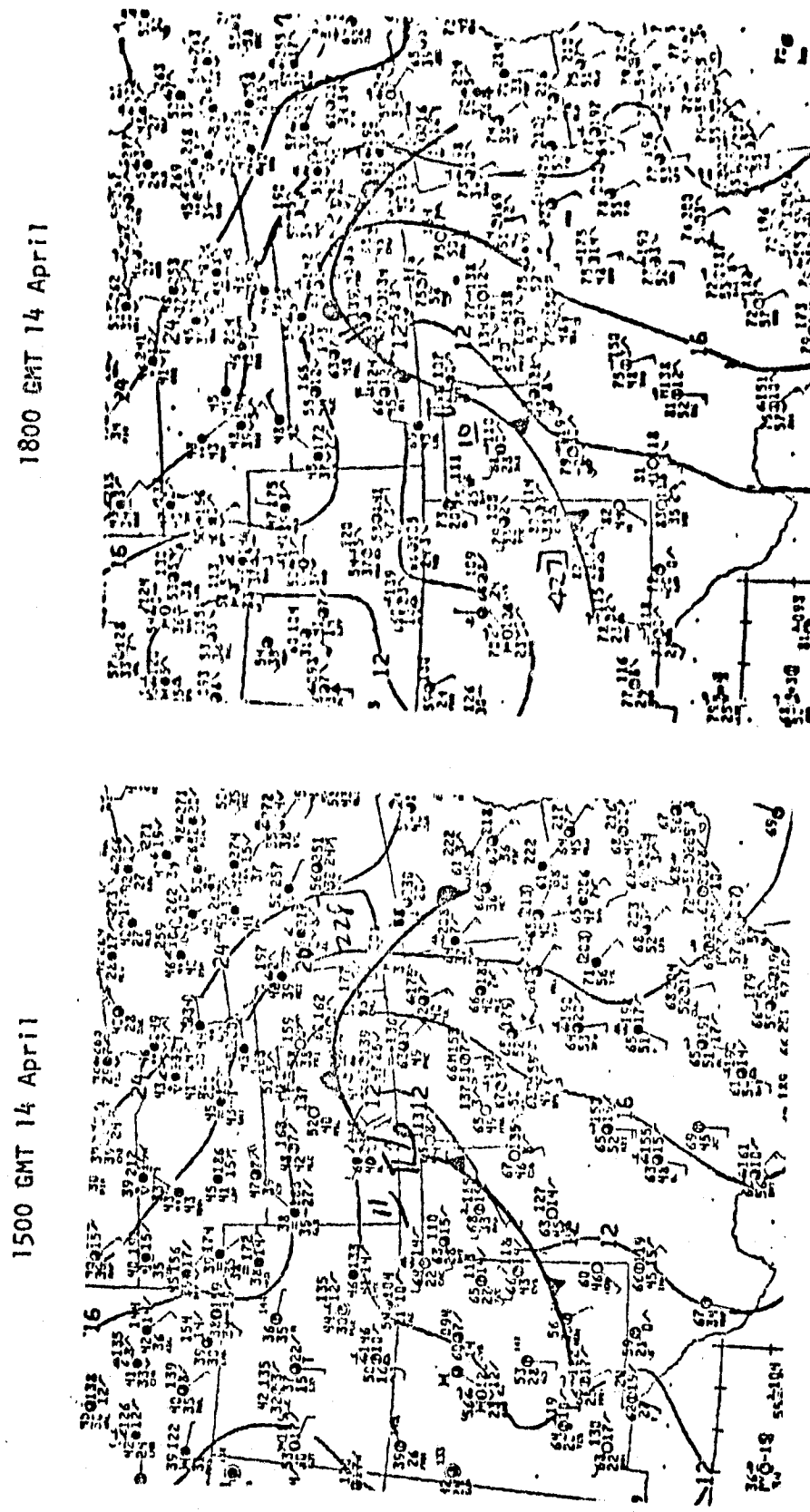
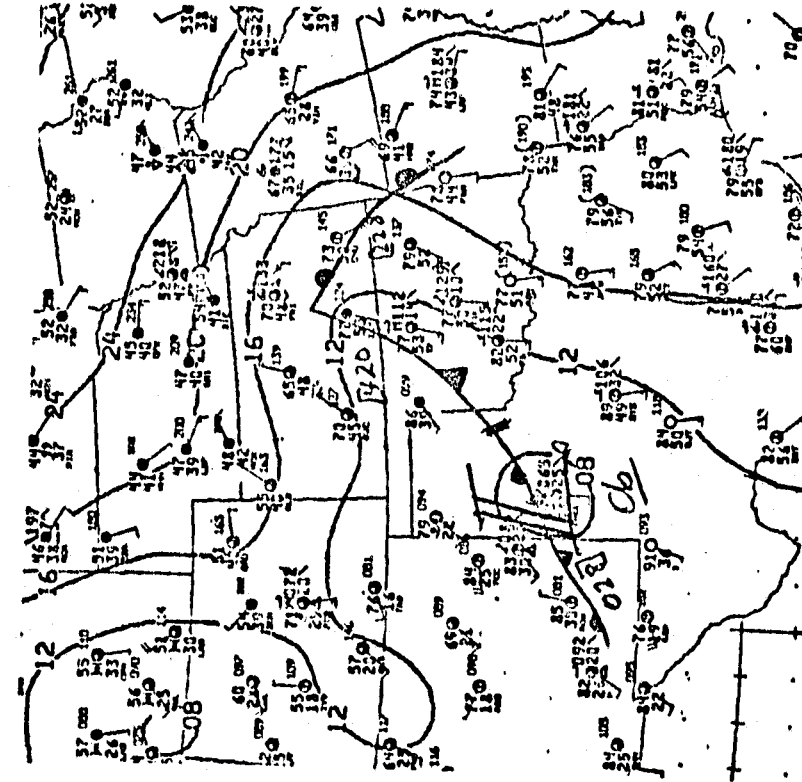


Figure 3-6a. Left: National Weather Service surface weather data and mean sea level pressure analysis for 1500 GMT 14 April.
Right: National Weather Service surface weather data and mean sea level pressure analysis for 1800 GMT 14 April.

2100 GMT 14 April



0000 GMT 15 April

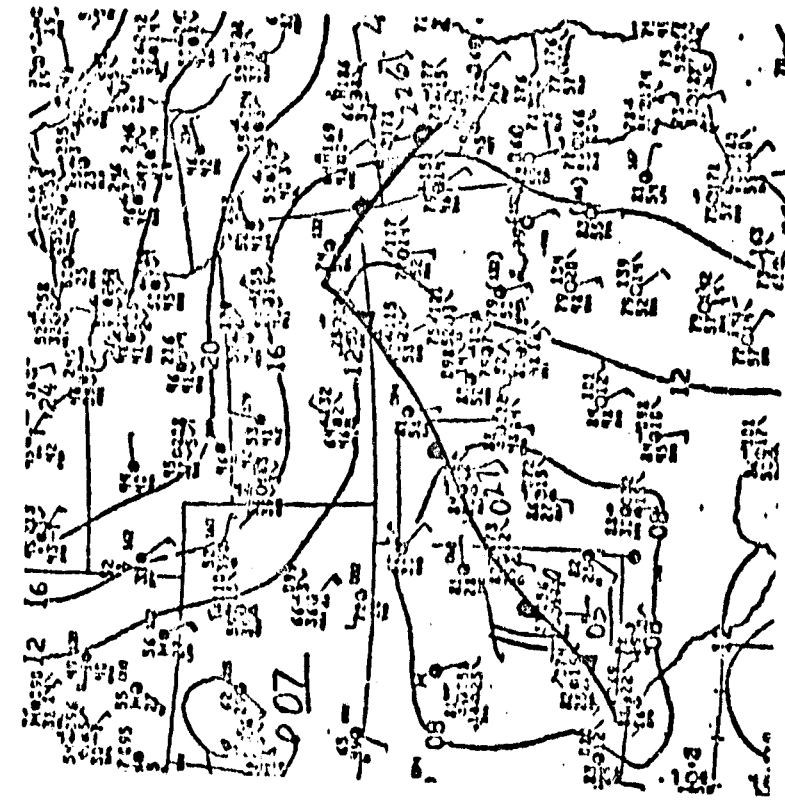


Figure 3-6b. Left: National Weather Service surface weather data and mean sea level pressure analysis for 2100 GMT 14 April.
Right: National Weather Service surface weather data and mean sea level pressure analysis for 0000 GMT 15 April.

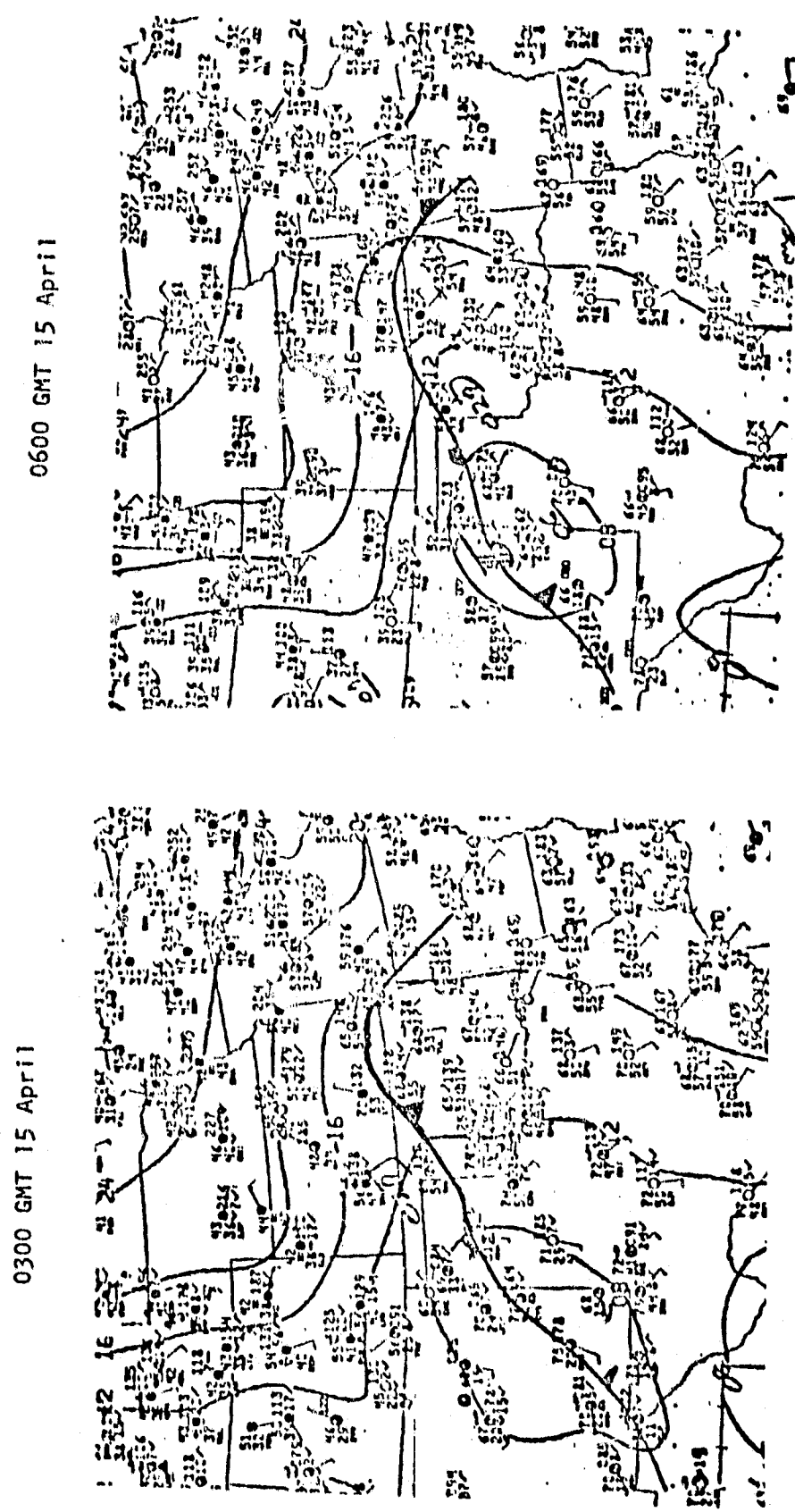


Figure 3-6c. Left: National Weather Service surface weather data and mean sea level pressure analysis for 0300 GMT 15 April.
 Right: National Weather Service surface weather data and mean sea level pressure analysis for 0600 GMT 15 April.

3.2 Case II: 17 April 1978

A good example of a multi-squall line severe weather outbreak associated with springtime synoptic cyclogenesis on the southern and Central Plains occurred on 17 April 1978. Several areas of severe weather developed during the afternoon and evening of the seventeenth. Numerous tornado reports were received from eastern Kansas and Oklahoma, Arkansas, Louisiana and Mississippi.

At 1200 GMT on 17 April 1978 the surface weather chart (Figure 3-7a) depicted a large scale trough on the western Plains from eastern Montana to western Texas. Within this trough a dissipating occluded low pressure center was situated over eastern Montana while a new developing cyclonic circulation was located at the point of occlusion over the Oklahoma panhandle. A warm front stretched eastward from the point of occlusion through northern Oklahoma and Arkansas. The air to the south of the warm front was quite moist. Surface dew points were near 60°F in Oklahoma and in the middle and upper 60's in southern and central Texas. At the same time, a cold front extended south-southwestward from the point of occlusion with cooler and much drier air to the west of it. The contrast in dew points across the cold front was quite sharp. Abilene, just to the east of the cold front, reported a 1200 GMT dew point of 61°F while Midland, located less than 250 km to the west observed a dew point of 20°F. Also noteworthy is the existence of a WNW flow at the surface across the southern and central Rocky Mountain region to the west of the macroscale trough despite a north-south orientation of the sea level isobars. Obviously, in this highly baroclinic flow the vertical change of the horizontal pressure gradient is large. Thus, the

geostrophic wind at a couple thousand meters above sea level would be expected to have a greater westerly component than at sea level. Since the surface elevation is near 2000 meters over much of this area, one would expect the surface winds to have a greater westerly component than that implied by the sea level isobaric pattern. This fact is significant because the 38 km model with its lack of terrain specification will have a tendency to initialize an excess of low level northerly geostrophic momentum over this area. This might be expected to lead to a deficiency of low level model westerly momentum on the lee slopes of the Rockies and a consequent retardation of the forecasted eastward progression of meteorological features in this area.

The 1200 GMT 500 mb chart (Figure 3-7a) reveals the presence of a strong short wave trough with an axis from northern Utah to the Gulf of California. The presence of a large vorticity maximum is apparent over the four state intersection area on the Colorado Plateau. Considerable west and northwest momentum (>50 kts) is present over Arizona, Nevada and California.

The ensuing development of this system can be seen by examining the 1200 GMT 18 April 1978 surface and 500 mb charts presented in Figure 3-7b.

The 38 km model domain and display areas are shown in Figure 3-8. It is important to note that the model domain incorporates only a portion of the synoptic scale wave. It fails to include much of the strong westerly momentum and cold advection over the western United States. The lack of complete representation

of the westerly momentum and cold advection would be expected to retard the eastward motion of hydrodynamic features forecasted within the model domain.

The combination of incomplete representation of the synoptic wave and the misrepresentation of the low level wind profile in the high elevation regions of Colorado and New Mexico would be expected to cause the model to have some difficulty in moving hydrodynamic features on the Plains to the east at the proper rate.

The NMC objective analysis data for the 1000 mb and 850 mb surfaces at 1200 GMT 17 April is presented in Figure 3-9. Once again the 1000 mb temperature and dew point fields indicate an anomalous warm and moist in Colorado which is associated with the "build down" of the temperature and dew point profile through the mountains. The 850 mb data is also affected slightly by the "build-down" problem in the Colorado and Wyoming area.

The 1150 m model initialization (Figure 3-10) reveals a band of warm moist air from eastern and central Texas northward to eastern Kansas. Significantly drier and cooler air is located immediately to the west of the moist band. Southerly geostrophic momentum is initialized across much of the eastern Plains while northerly geostrophic momentum is initialized on the lee slopes of the Rocky Mountains.

Figure 3-11 displays a time sequence of the model forecast of 1150 meter pressure, wind vectors, mixing ratio and divergence as well as σ_E evaluated between the 1150 and 3400 meter levels.

During the first six hours of the model forecast one can note the east northeastward movement of the low pressure center and

pressure trough. However, by six hours into the forecast (1800 GMT) it is apparent that the pressure falls ahead of the advancing low pressure area have contributed to the production of a low level easterly isallobaric wind component. This slows the eastward propagation of the low pressure area and eventually causes it to begin retrogressing to the southwest. Obviously, in the real world, the cold advection and synoptic scale westerly momentum which is west of the model domain at the time of initialization, continue to force the east-northeast movement of the synoptic low pressure area. The failure of this synoptic eastward translation to be maintained through the forecast period allows the westward directed pressure gradient force in advance of the trough, to act for unrealistically long time periods over the same mesoscale volume over eastern Kansas, eastern Oklahoma and Arkansas. This results in the over prediction of easterly momentum and the resultant failure of the sub-synoptic and mesoscale features to progress eastward at a realistic rate.

However, the sub-synoptic organization of potential instability and low level convergence appears to be well forecasted during the first 8 hours of the simulation. During this time the σ_E values decrease in east central Kansas from an initial value of about -4.6 to an eight hour value near -5.0. This is largely a result of drier, cooler air being advected from the west at the 3400 meter level. For example, the 1150 meter θ_E at Wichita (ICT), Kansas remains nearly constant at 310°K during the first eight hours of the model forecast, while the 3400 meter θ_E value drops from an initial value of 283.3°K to 280.4°K by eight hours (2000 GMT) into the forecast. During the same time period, the growth of convergence occurs as isallobarically generated easterly

momentum becomes dominant over the eastern section of the display area, while northwesterly momentum continues to prevail over western Kansas and the Texas-Oklahoma panhandle area. By six hours into the forecast (1800 GMT) a northwest-southeast zone of convergence is established from northwestern Kansas to southeastern Oklahoma. The eastern Oklahoma portion of the convergence area is superimposed upon an area of potential instability and one might expect convective development in this region. The 1735 GMT radar summary in Figure 3-12 shows an area of scattered convection with radar tops near 40,000 feet over this region. The other area of strong convergence over northwestern Kansas has just appeared during the past hour. During the first five hours of the forecast, this had been a region of strong divergence.

However, during the next 3 hours, the convergence area over northwestern Kansas moves eastward. By eight hours (2000 GMT) into the forecast, an area of convergence exceeding $-5 \times 10^{-5} \text{ s}^{-1}$ is located to the north of Wichita and superimposed on a σ_E minimum of nearly -5.2. The 2035 GMT radar chart in Figure 3-12 shows a fairly good correlation between this convergence-potential instability superposition area and a developing very intense squall line in east central Kansas. However, the effect of the excess generation of easterly momentum is apparent at this time. The convergence area in eastern Oklahoma at 6 hours has moved westward into central Oklahoma whereas the 2035 GMT radar summary indicates that the convective activity has moved eastward into northwestern Arkansas and extreme eastern Oklahoma.

Twelve hours into the forecast (0000 GMT 18 April) a north-south band of u convergence ($\nabla \cdot \vec{V}$ dominated by $-\partial u / \partial x$) is well

organized from central Kansas southward to western Oklahoma.

Convergence values approaching $-9 \times 10^{-5} \text{ s}^{-1}$ are forecasted in this area in superposition with a band of minimum σ_g . The convective activity implied by this forecast is about 200 km to the west of the observed activity on the 2335 GMT radar summary, although the orientation and implied severe intensity appear to be well predicted. The twelve hour forecasted wind vectors exhibit a noticeable increase in the southerly (+v) component over eastern Kansas and eastern Oklahoma as the Coriolis force begins to rotate the geostrophic wind components.

Over the next three hours the model fails to move the old convergence area farther to the east, but interestingly, another area of convergence begins to develop to the southeast of the original convergence band. This band rapidly grows and propagates southeastward so that by 18 hours (0600 GMT) convergence magnitudes have reached $-6 \times 10^{-6} \text{ s}^{-1}$ within it. Although it is well to the northwest of the actual convective area over eastern Louisiana and western Mississippi, it is interesting to note the development of a second convergence area ahead of the initial u convergence zone. This is, in principle, similar to the actual development of a second intense squall line in advance of the initial line.

In summary, the 17 April case illustrated the inadequacy of resolving only a portion of the synoptic scale wave when attempting to produce an extended period sub-synoptic or mesoscale forecast. The agreement of the forecasted initial convergence and potential instability with the observed convective activity was good through eight hours, after which the unresolved eastward motion of the

synoptic system caused the 38 km model forecast to fail to move the correctly organized mesoscale features to the east, and possibly to misforecast subsequent non-linear mesoscale wave development and interaction. The mountain "build-down" problem may have contributed to this situation by defining excess low level northerly momentum which acted to produce a poor representation of the the low level cold advection in the area to the west of the developing synoptic scale cyclone.

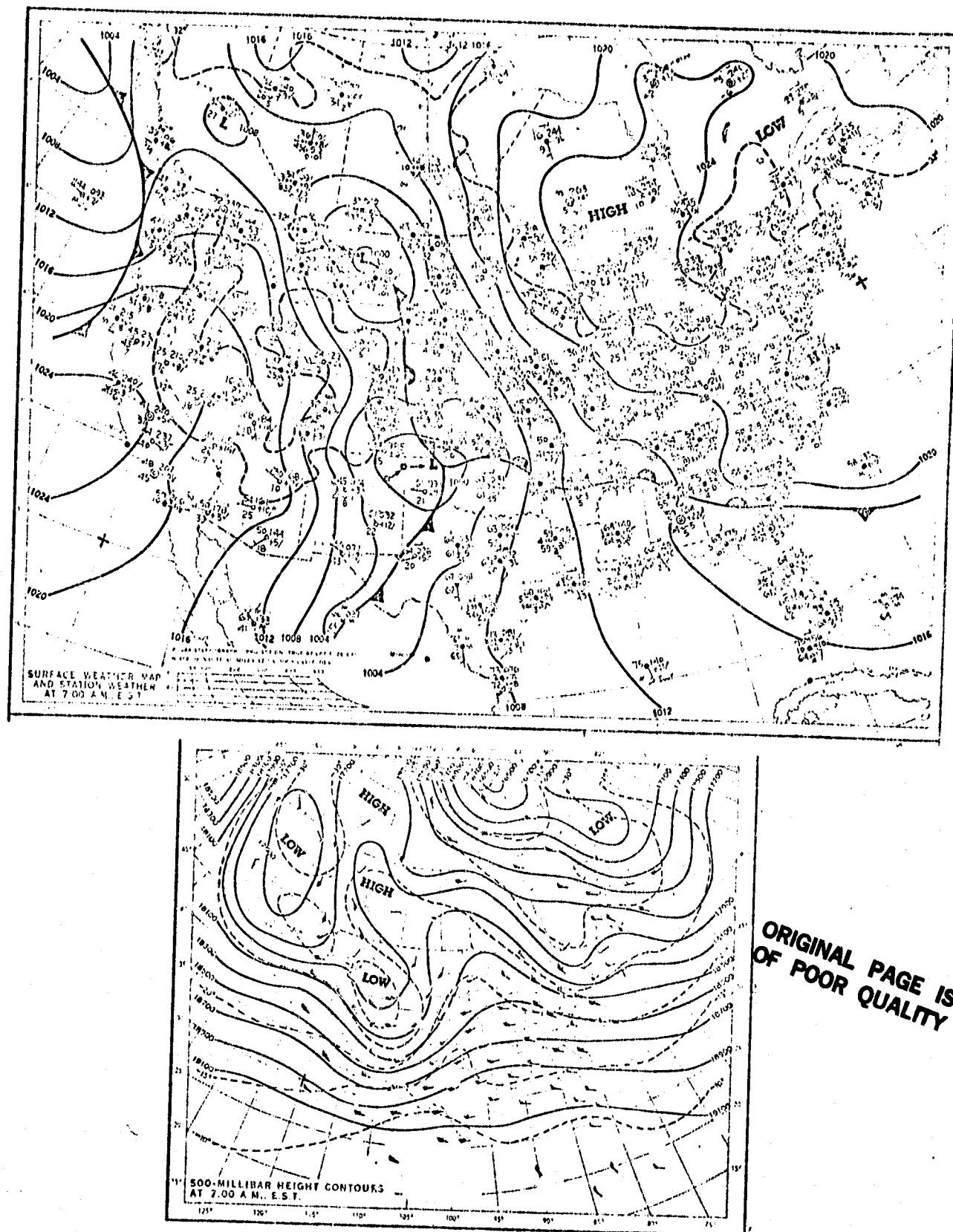


Figure 3-7a. Top: Surface Weather map for 1200 GMT 17 April 1978.
 Bottom: 500 mb chart for 12 0 GMT 17 April 1978.
 Height contours are in feet.

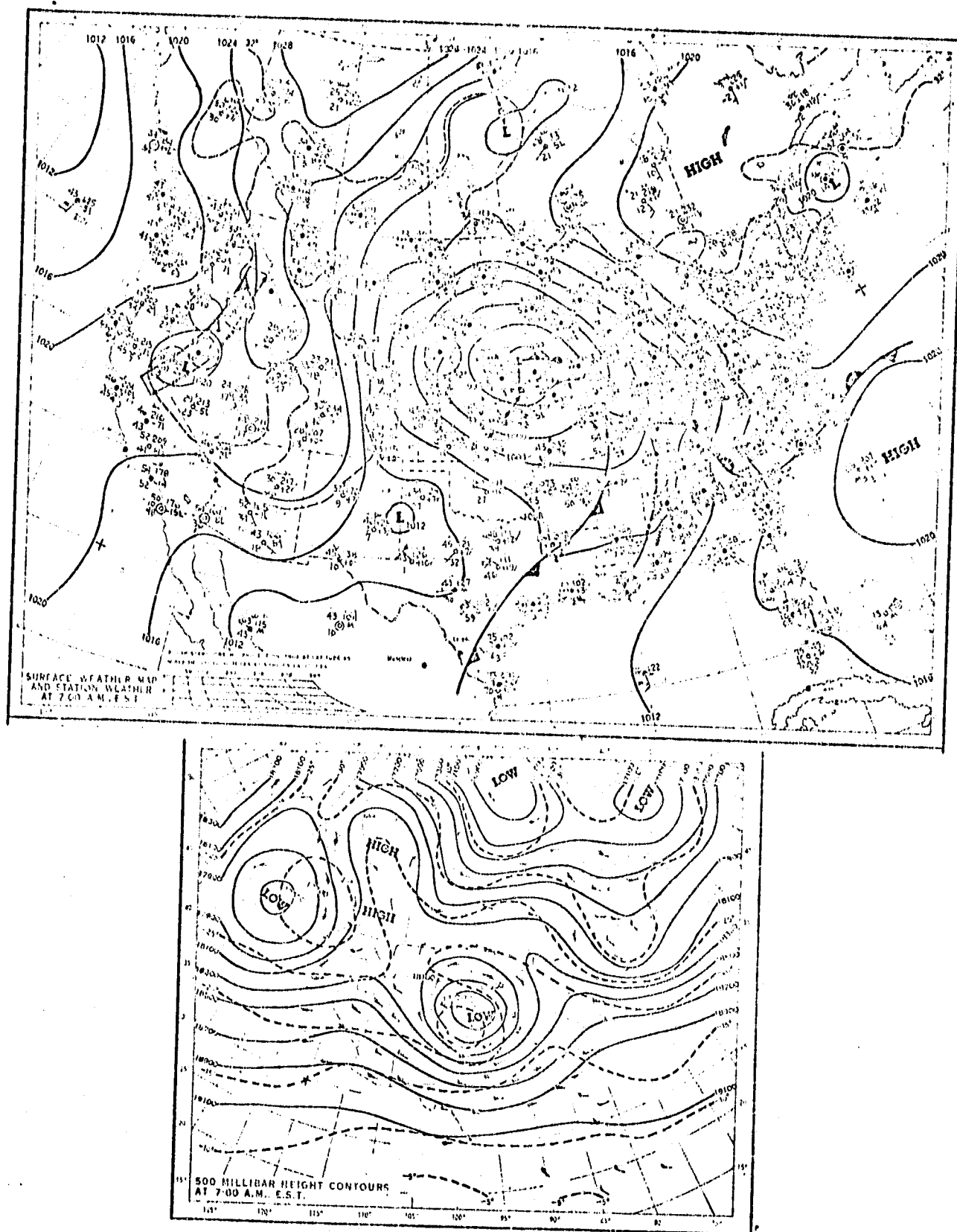


Figure 3-7b. Top: Surface Weather map for 1200 GMT 18 April 1978.
 Bottom: 500 mb chart for 1200 GMT 18 April 1978.
 Height contours are in feet.

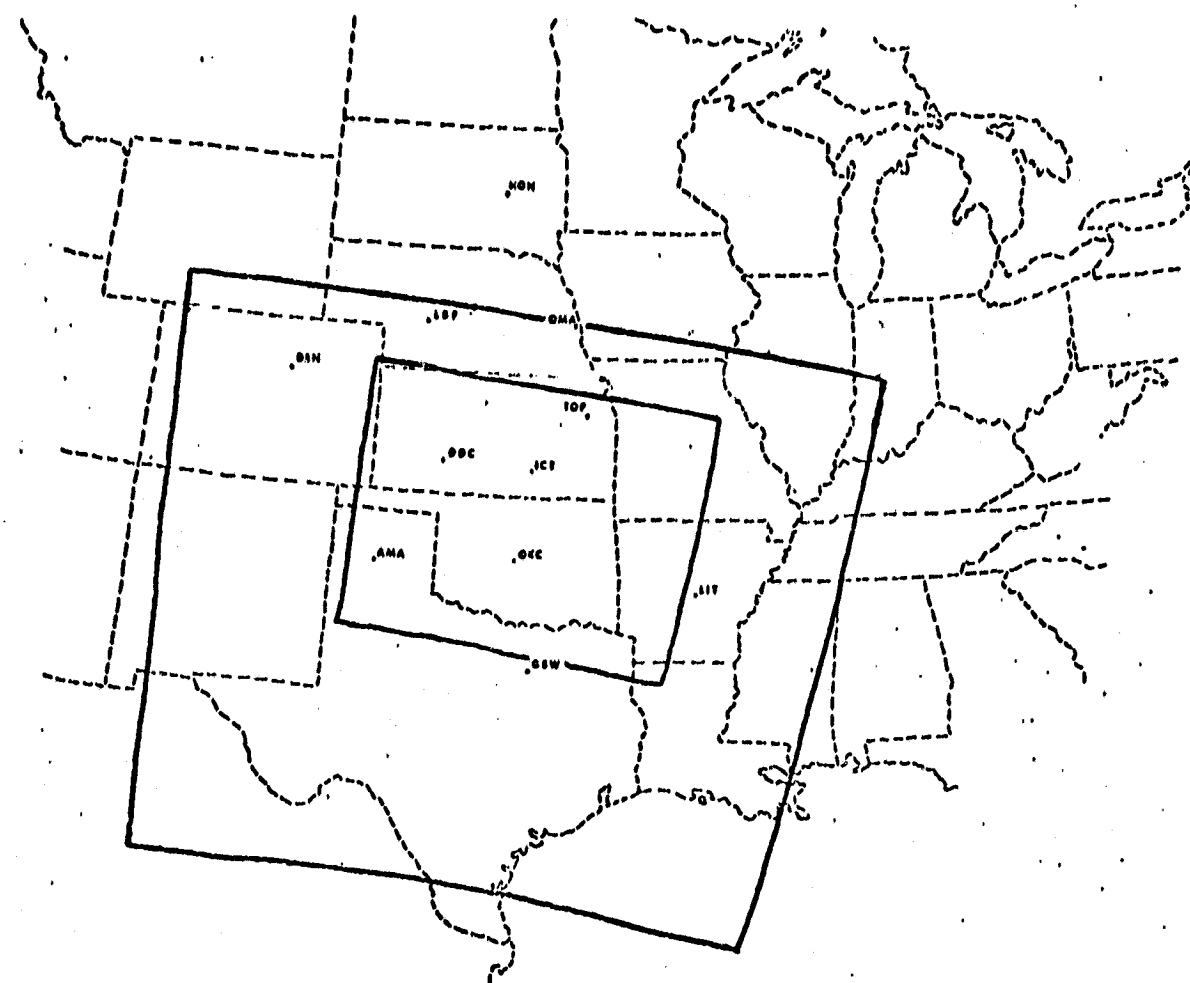


Figure 3-8. The 38 km model domain and display area for the 17 April 1978 case. Outer box indicates the model domain. Inner box demarcates the display area.

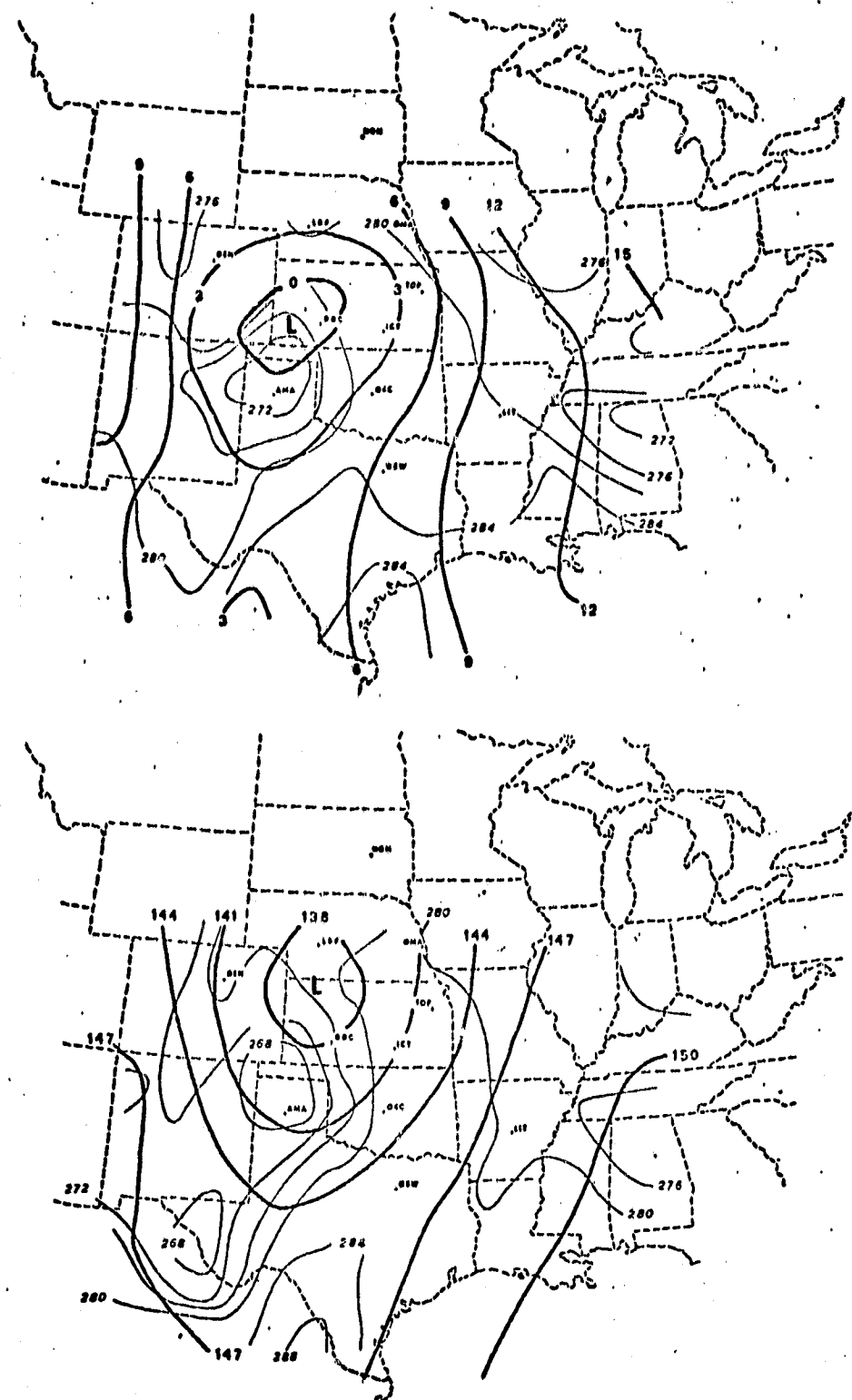


Figure 3-9. Top: NMC 1000 mb height and dew point data for 1200 GMT 17 April.
 Bold lines are heights in decameters. Light lines are dew points in °K.
 Bottom: NMC 850 mb height and dew point data for 1200 GMT 17 April.
 Bold lines are heights in decameters. Light lines are dew points in °K.

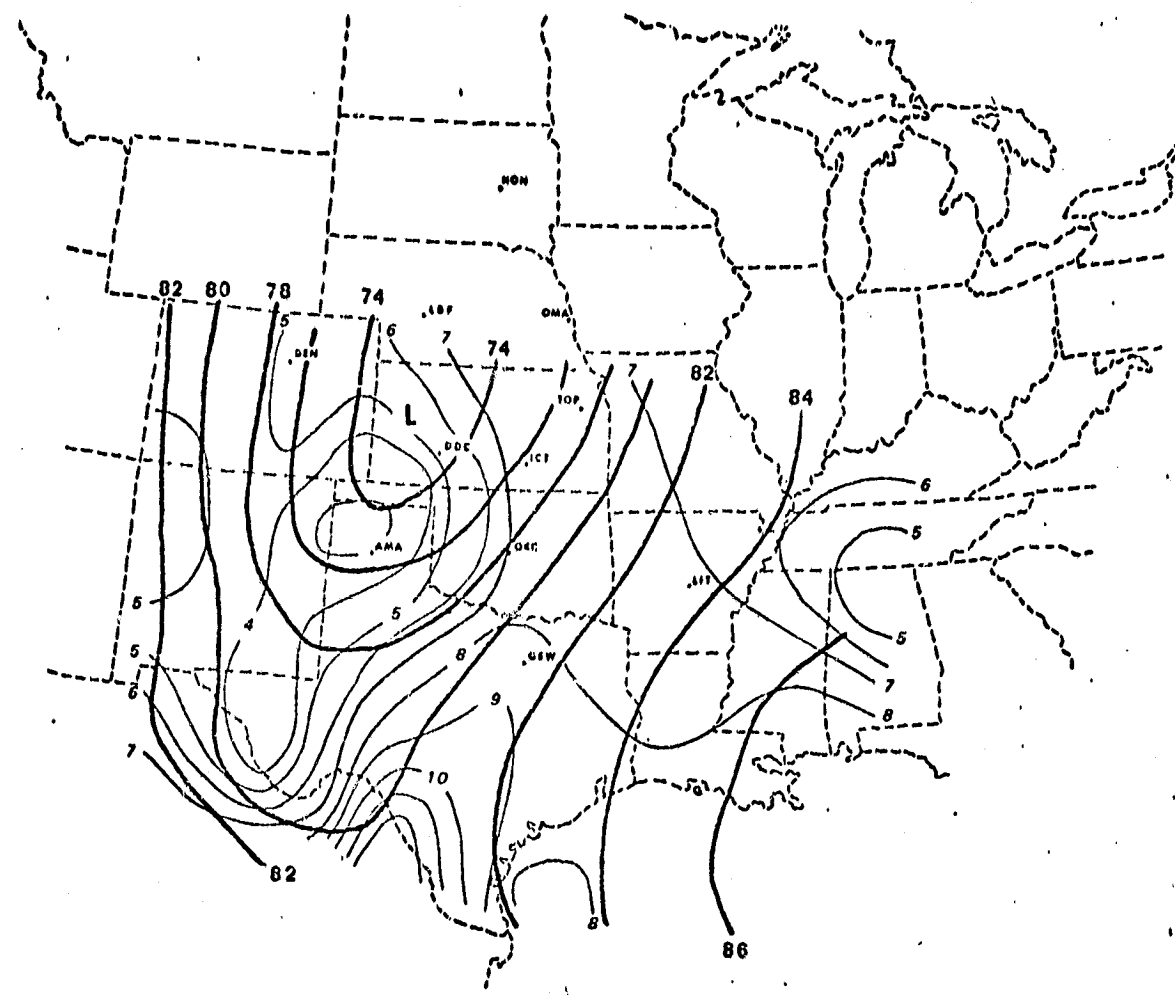


Figure 3-10. 38 km model 1150 m initialization of pressure and mixing ratio. Bold lines are isobars at intervals of 2 mb. Labels omit the preceding 8. Light lines are mixing ratios in g/kg.

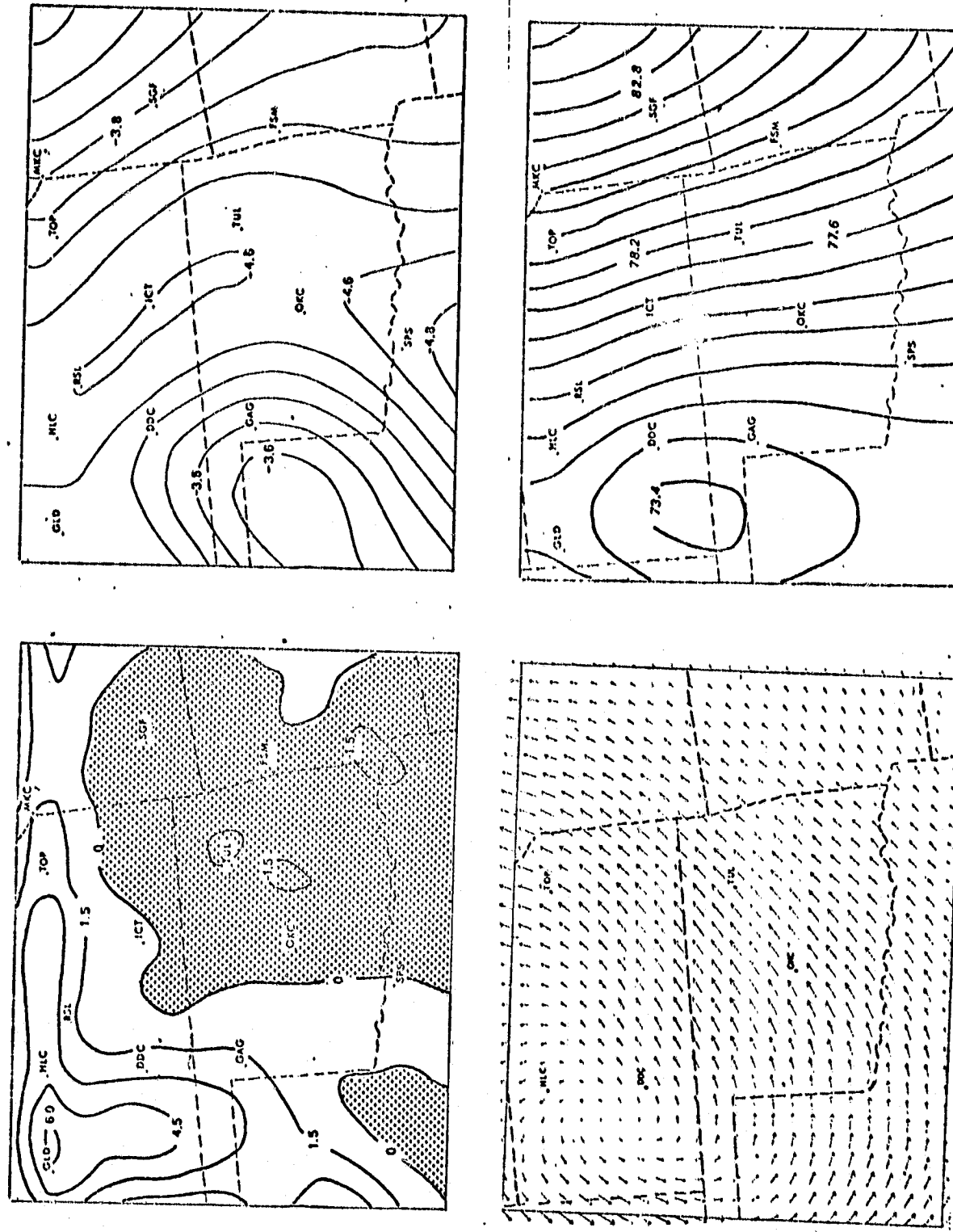


Figure 3-11a. Two hour 1150 m model forecast valid at 1400 GMT 17 April. Upper left: Divergence with isopleths at intervals of $0.2 \times 10^{-5} \text{ s}^{-1}$. Upper right: Pressure at intervals of 0.6 mb. Lower left: Wind vectors. Lower right: Wind vectors omitting preceding 8.

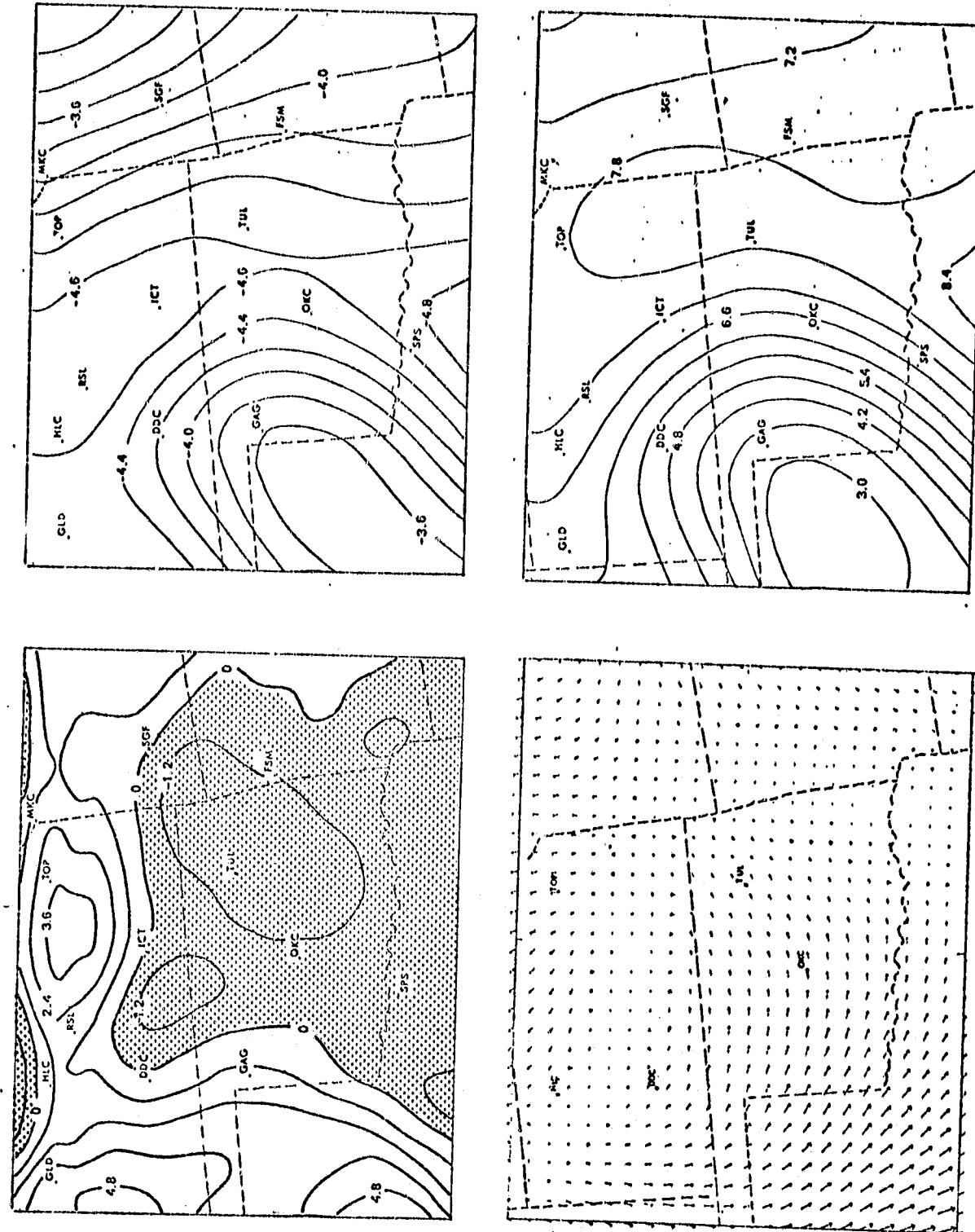


Figure 3-11b. Four hour 1150 m model forecast valid at 1600 GMT 17 April. Upper left: Divergence with isopleths at intervals of $1.2 \times 10^{-5} \text{ s}^{-1}$. Upper right: Divergence at intervals of $0.2 \times 10^{-5} \text{ s}^{-1}$. Lower left: Mixing ratio at intervals of 0.6 g/kg.

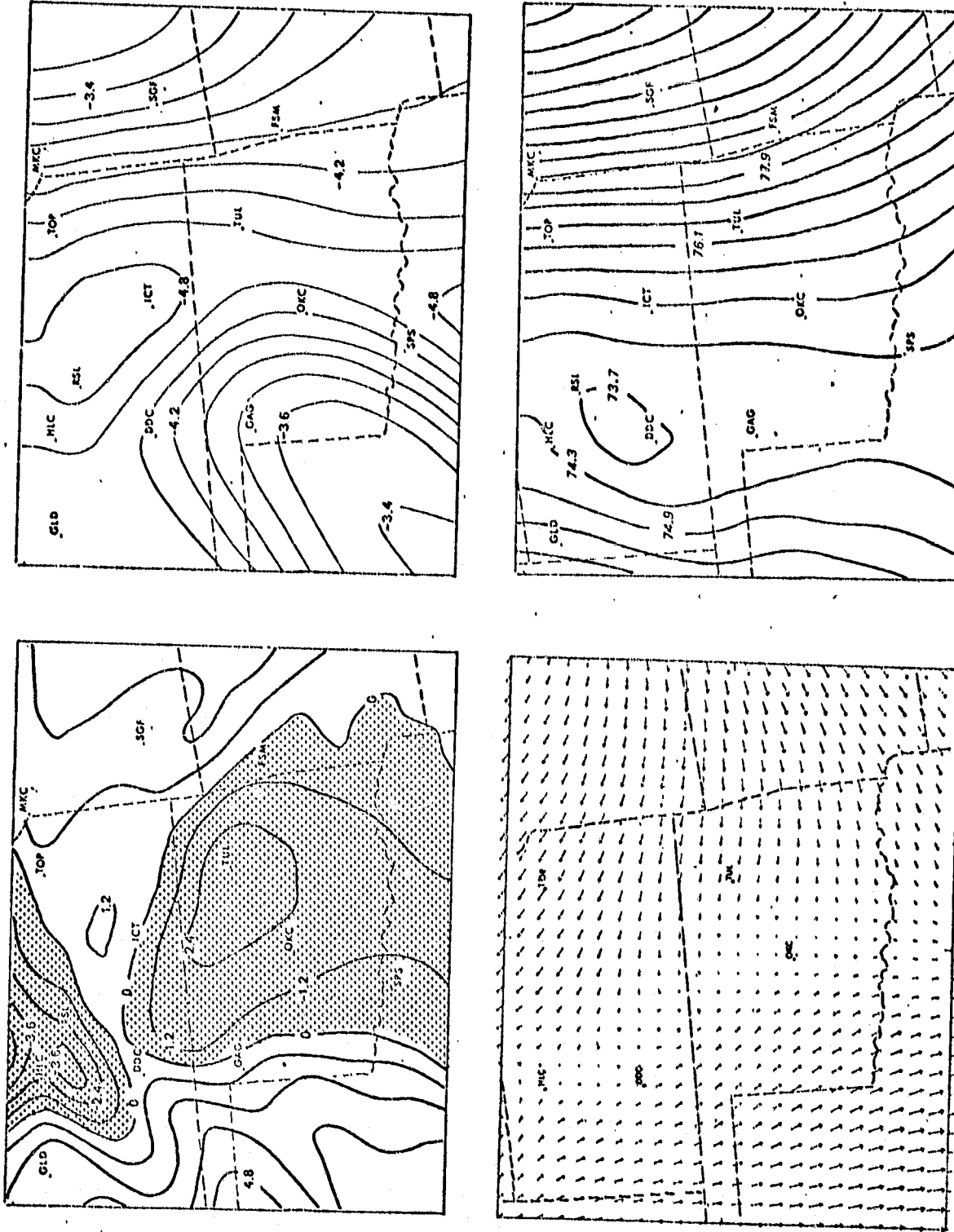


Figure 3-11c. Six hour 1150 m model forecast valid at 1800 GMT 17 April. Upper left: Divergence with isopleths at intervals of $1.2 \times 10^{-5} \text{ s}^{-1}$. Upper right: σ_E at intervals of 0.2. Lower left: Wind vectors. Lower right: Pressure at intervals of 0.6 mb, preceding 8 is omitted.

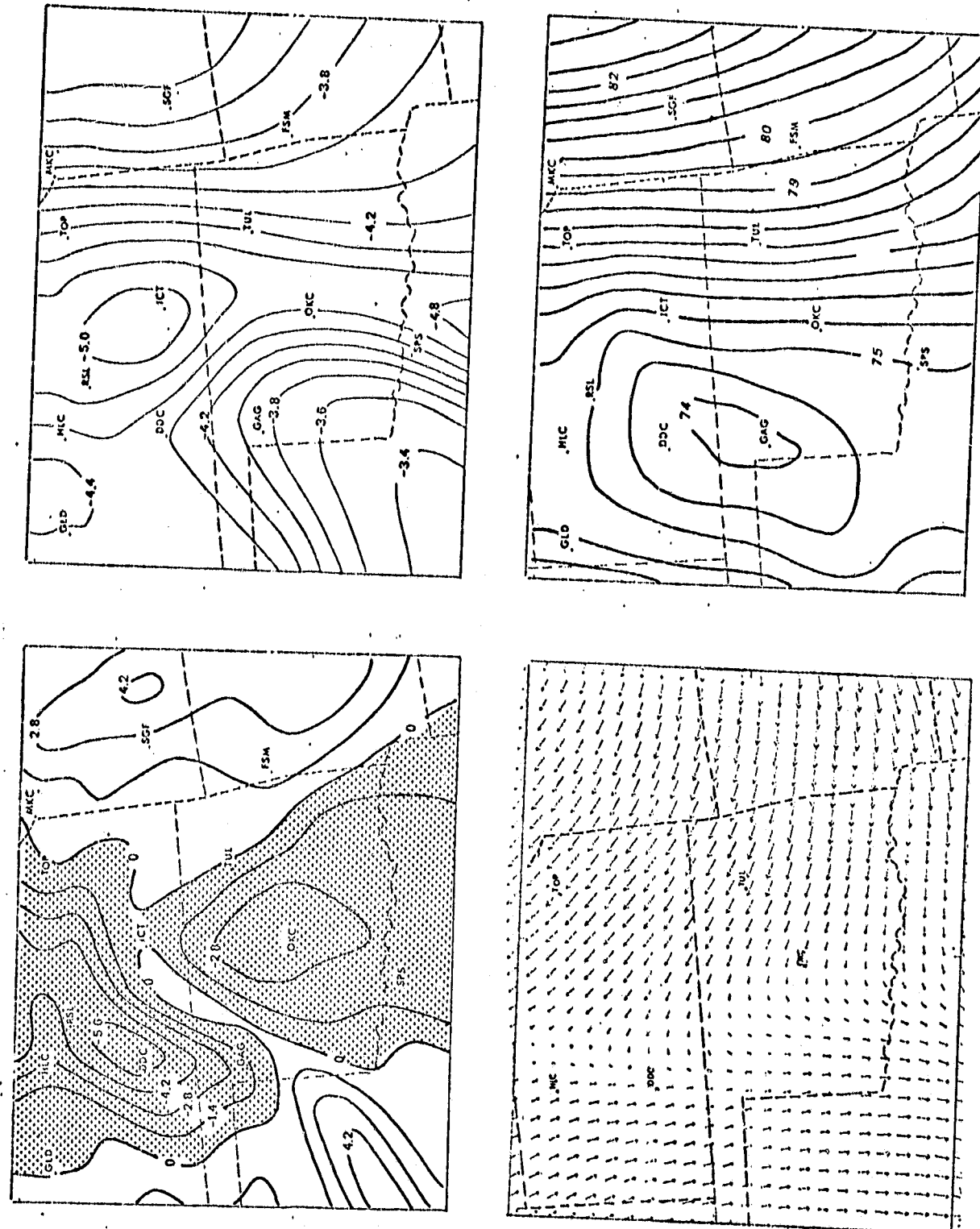


Figure 3-11d. Eight hour 1150 m model forecast valid at 2000 GMT 17 April. Upper left: Divergence with isopleths at intervals of $0.2 \times 10^{-5} \text{ s}^{-1}$. Upper right: σ_E at intervals of 0.2. Lower left: Wind vectors. Lower right: Pressure at intervals of 0.5 mb, preceding 8 is omitted.

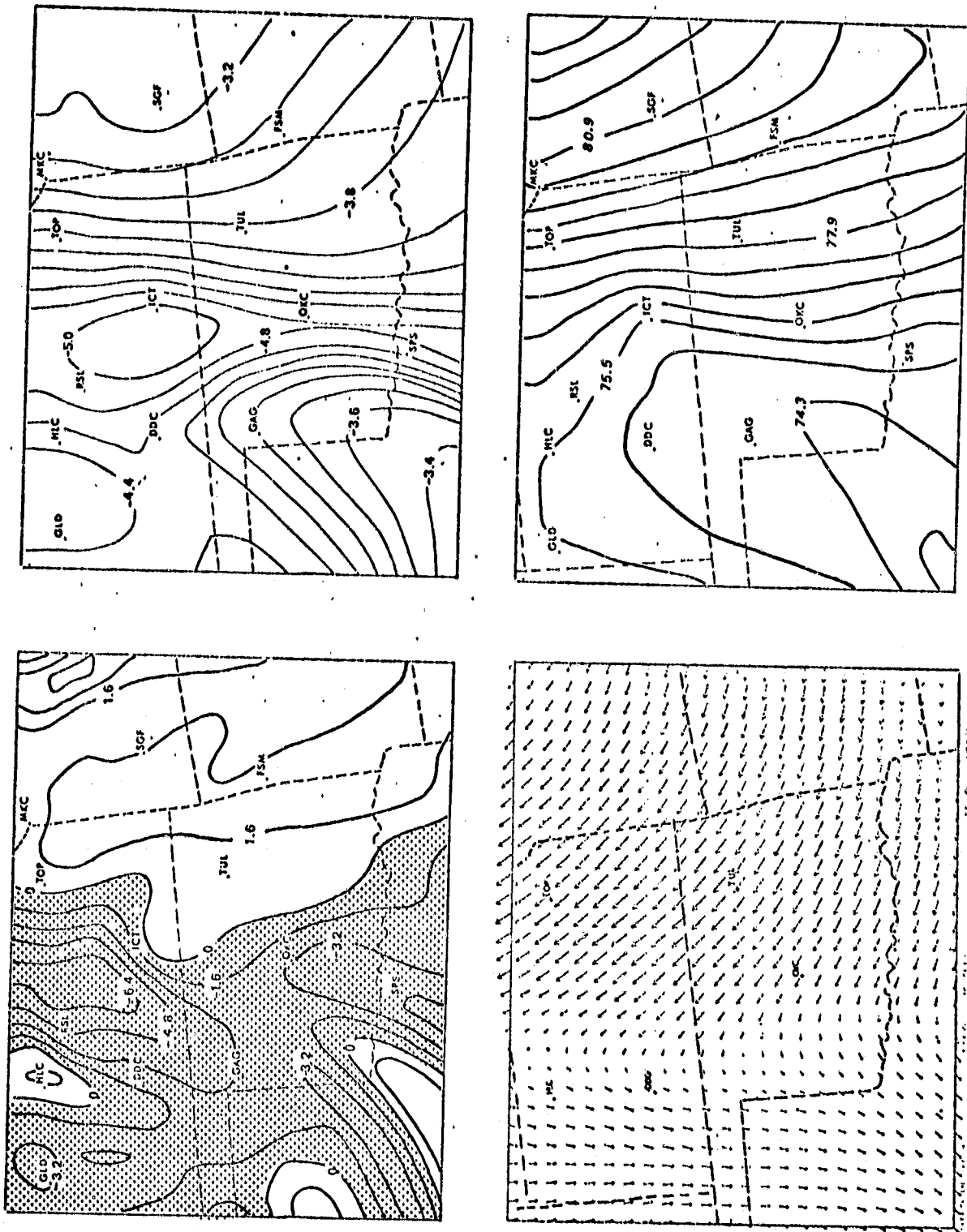


Figure 3-11e. Ten hour 1150 m model forecast valid at 2200 GMT 17 April. Upper left: Divergence with isopleths at intervals of $1.6 \times 10^{-5} \text{ s}^{-1}$. Upper right: Pressure at intervals of 0.2 mb. Lower left: Wind vectors. Lower right: Pressure at intervals of 0.6 mb, preceding 8 is omitted.

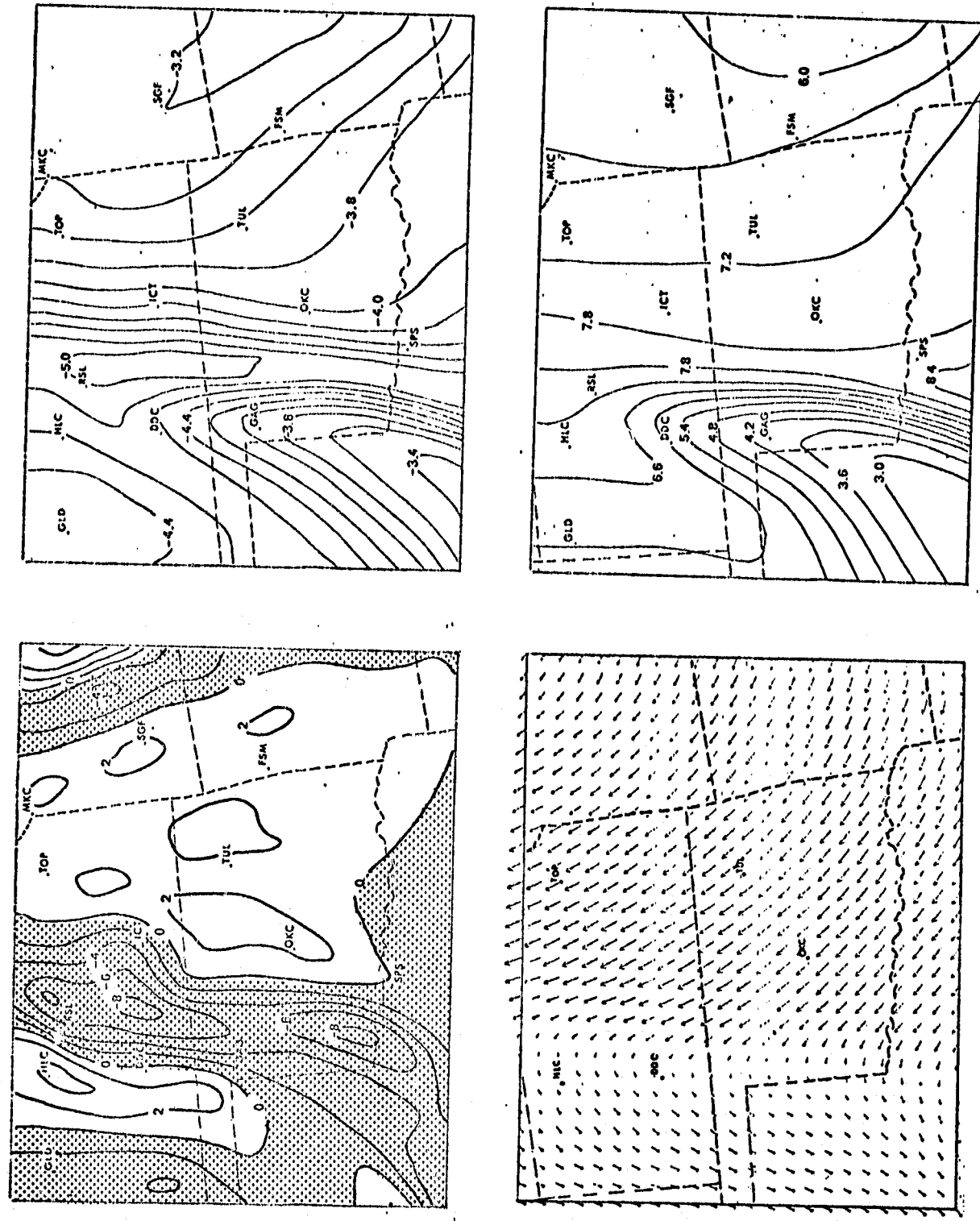


Figure 3-11f. Twelve hour 1150 m model forecast valid at 0000 GMT 18 April. Upper left: Divergence at intervals of $2 \times 10^{-5} \text{ s}^{-1}$. Upper right: Mixing ratio at intervals of 0.2. Lower left: Wind vectors. Lower right: Wind vectors.

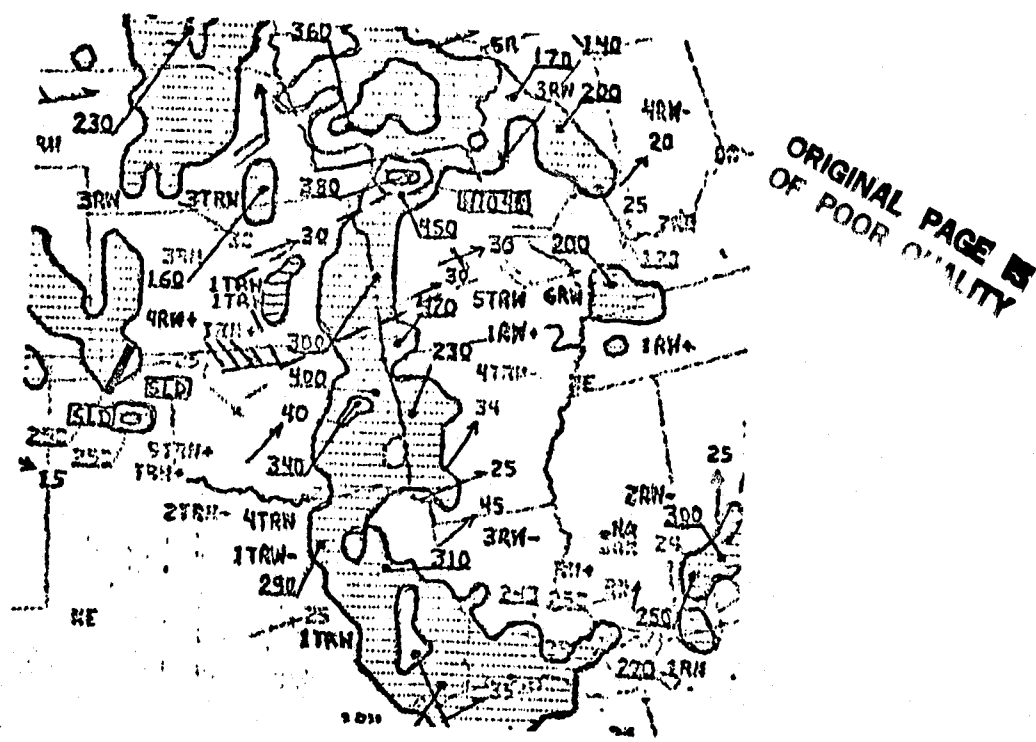
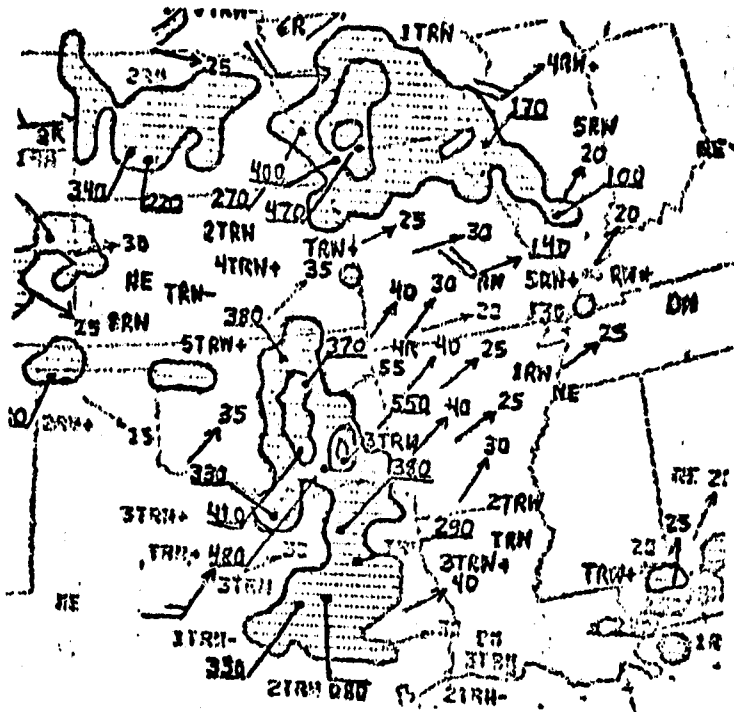


Figure 3-12a. Above: National Weather Service (NWS) radar summary for 1735 GMT 17 April 1978.
 Below: NWS radar summary for 1935 GMT 17 April 1978.

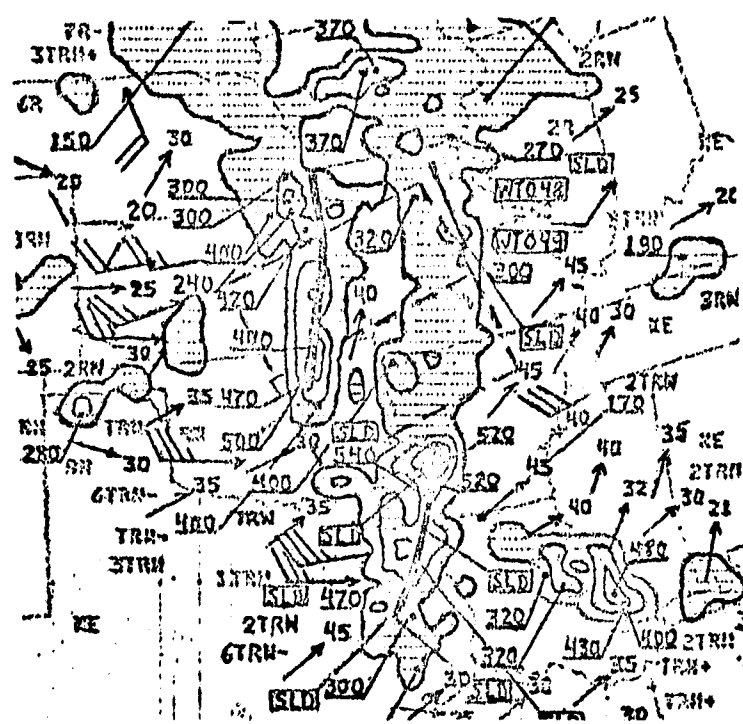
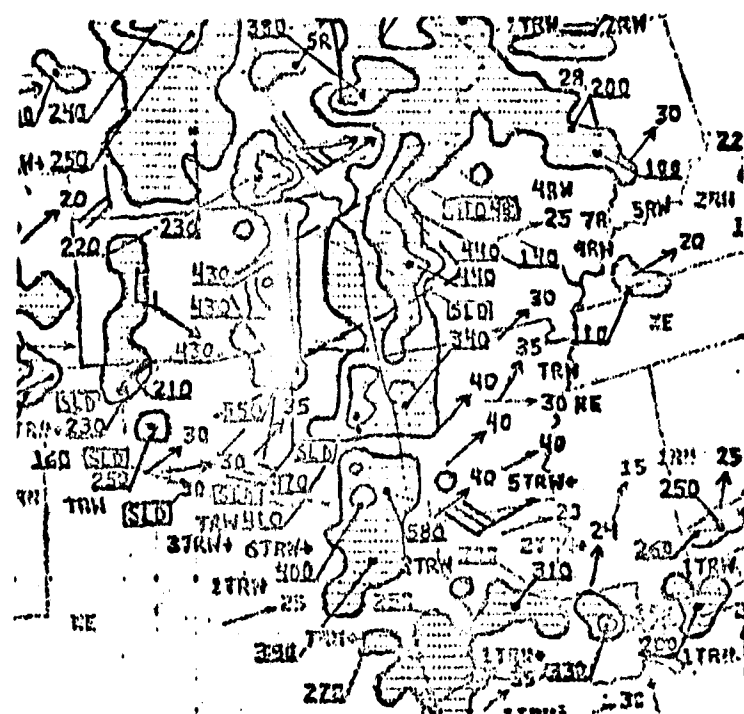


Figure 3-12b. Above: National Weather Service (NWS) radar summary for 2035 GMT 17 April 1978.
 Below: NWS radar summary for 2235 GMT 17 April 1978.

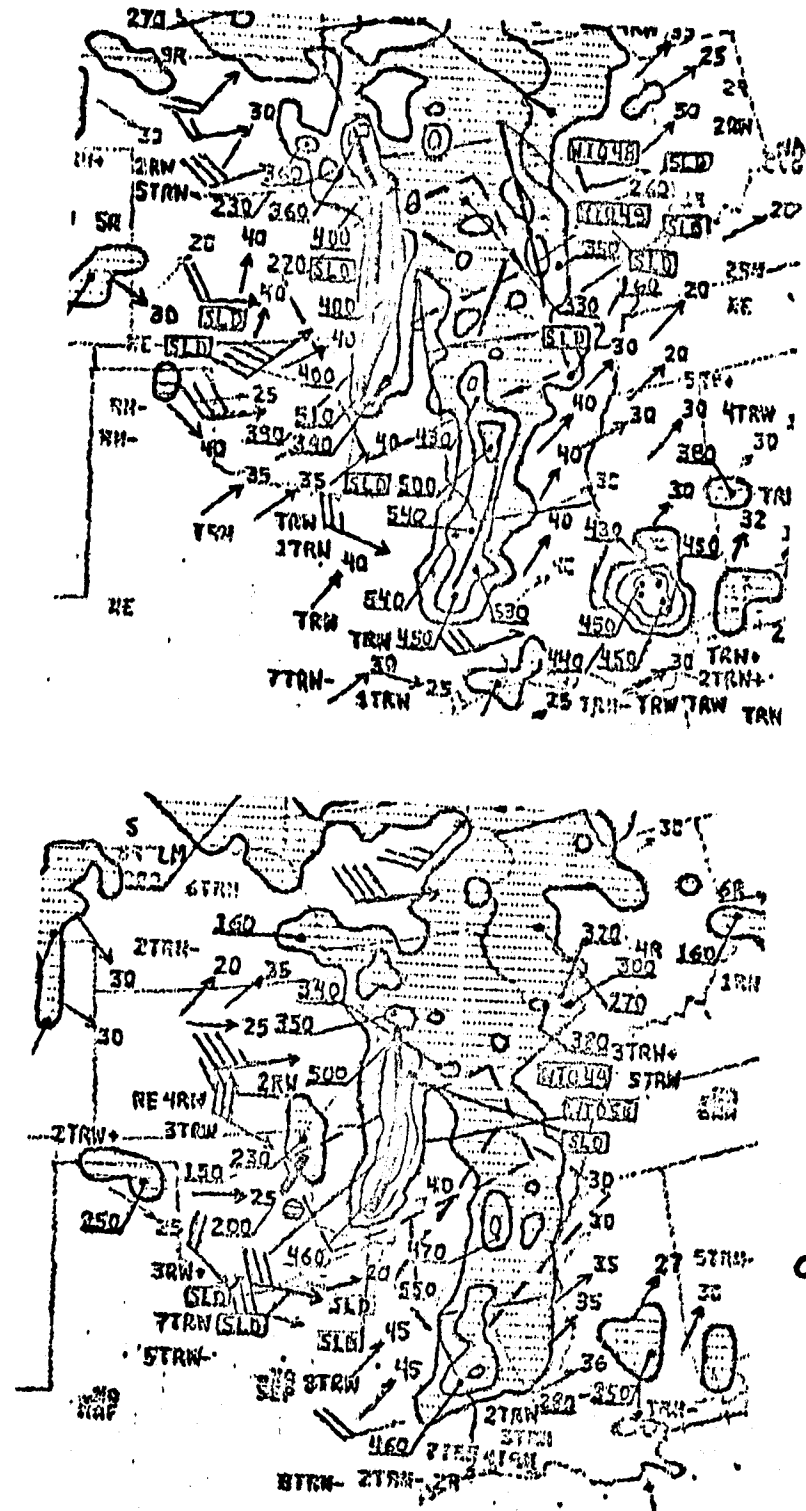


Figure 3-12c. Above: National Weather Service (NWS) radar summary for 2335 GMT 17 April 1978.
Below: NWS radar summary for 0135 18 April 1978.

3.3 Case III: 29 April 1978

A severe thunderstorm dropped hailstones up to 3.0 inches in diameter in the vicinity of Ada, Oklahoma around 8:00 pm (0200 GMT) on 29 April 1978. At the same time a funnel cloud was reported four miles to the southeast of Ada, Oklahoma (Storm Data, April 1978). In addition, several other reports of hail exceeding 1 1/2 inches in diameter were received from southeastern Oklahoma.

The synoptic circulation on the 29 April 1978 was rather tranquil over the Southern Plains. The 1200 GMT surface weather chart (Figure 3-13a) reveals the presence of trough from western Nebraska to the Rio Grande basin. As is usually the case on the Western Plains, this lee trough separated cool and very dry air to the west from warmer and somewhat more moist air to the east. Consequently, a stationary front was placed along the axis of this trough. A weak warm front extended across northern Oklahoma into Arkansas. This front separated the warm, moist tropical air from the somewhat cooler modified polar air to the north of the front.

The 1200 GMT 500 mb chart (Figure 3-13a) indicates the existence of a split in the general westerly flow over North America. The northern wave train traverses northwestern Canada and turns southward into the northeastern United States. At the same time, a weaker westerly current flows across the southern United States. Two weak disturbances are embedded in the southern current. One of these short waves is located over the Central Plains with another wave located to the west over Arizona, Nevada and Utah.

The surface and 500 mb charts for 1200 GMT 30 April 1978 (Figures 3-13b) indicate very little change in the general synoptic circulation over the 24 hour period from 1200 GMT

29 April to 1200 GMT 30 April.

The 38 km model domain and display area are demarcated in Figure 3-14. The 1000 mb, 850 mb and 700 mb NMC analysis data for the area of the model domain is presented in Figure 3-15.

The interpolated 1150 meter pressure and mixing ratio distributions are presented in Figure 3-16. The low pressure center at 1150 meters is located on the Kansas-Oklahoma border. This is slightly north of the location analyzed on the sea level pressure map. The pressure distribution implies a southwesterly geostrophic flow across central Texas and a broad southerly flow across most of the Eastern Plains and the Mississippi Valley. Northerly geostrophic flow in excess of 20 kts. is implied by the pressure distribution over the area from western Nebraska to eastern New Mexico. The 1150 meter mixing ratio distribution reveals the existence of a band of moist air from west central Texas northeastward to Missouri and Iowa. Local maxima are present in west central Texas and northwestern Missouri. Mixing ratio values of more than 8 g/kg in central Colorado and western Wyoming are fictitious and are related to the moisture build-down problem in these high altitude regions.

During the first nine hours of the model forecast, the 1150 m low pressure center is predicted to drift slowly southeastward. The model moves the low pressure center from its initial position northwest of Gage, Oklahoma to slightly south of Oklahoma City by the ninth forecast hour (2100 GMT). The pressure changes associated with the forecasted southeastward movement help to generate the southeasterly momentum which is present over Arkansas and western Louisiana in the nine hour model wind field (Figure 3-17a).

The nine hour evolution of the pressure and wind field has organized an axis of warm moist air from east central Texas northeastward into southeastern Oklahoma. This warm moist axis is clearly demarcated in the nine hour $1150 \text{ m } \sigma_E$ field depicted in Figure 3-17a.

The reality of this forecasted southeastward drift of the low pressure center and the organization of a moisture band from central Texas into eastern Oklahoma is supported by surface weather observations. The surface dew point field shown in Figure 3-18, clearly illustrates the organization of a narrow moist tongue from central Texas northeastward into eastern Oklahoma between 1200 GMT and 2100 GMT. For example, the northward advance of this moist tongue causes dew points at McAlester, Oklahoma (MLC) to rise from 58°F at 1200 GMT to 64°F by 2100 GMT. Several other stations in eastern Oklahoma also report dew point rises of about 5°F during this nine hour period. The sea level pressure map indicates a nine hour movement of the low pressure center from near the southwestern Oklahoma-Texas border southward to the vicinity of Abilene, Texas. The difference in the placement of the low pressure centers between the model forecast and the observed sea level pressure chart can be attributed to the slope of this pressure center to the north with height.

The northward displacement between sea level and 1150 m is implied by the northward slope of the low height center between the 1200 GMT 1000 mb and 850 mb pressure levels (Figure 3-15a,b). Thus, the pressure changes forecasted by the model appear to be consistent with those implied by the sea level pressure data.

The nine hour forecasted σ_E field reveals an axis of low equivalent hydrostatic stability coincident with the low level warm,

moist tongue present in the θ_E field. At the same time, the divergence field delineates two areas of moderate convergence. Both of these are on the western edge of the easterly momentum. One is located in southern Oklahoma and extends into extreme northern Texas, while a second area is located to the south of Dallas, Texas (GSW). It is this second area that is superimposed upon the forecasted area of lowest σ_E . The 2135 GMT radar chart (Figure 3-17c) indicates that no convective activity was observed at that time. However, the 2235 GMT radar summary does reveal the development of convective activity over the area south of Dallas.

By twelve hours (0000 GMT 30 April) into the forecast, the model momentum field appears to have a wave-like shape with south-southeasterly winds to the east of the wave axis and east-northeast winds to the west of the axis. At this time the axis is forecasted to extend from extreme eastern Kansas southwestward through eastern and east central Oklahoma. The 0000 GMT surface wind field (Figure 3-18) indicates a pattern which is very similar to the model forecast. South-southeast surface winds are present over eastern Oklahoma, eastern Texas and western Arkansas, while an east-northeasterly flow has become established across western Oklahoma and the Texas panhandle. In fact, the wind shift axis is very close to the position forecasted by the model.

The twelve hour model θ_E field shows a northward protrusion of the warm moist air into eastern Oklahoma over nearly the same area as the moist tongue analyzed on the observed surface dew point field. The σ_E field indicates that this 1150 m high θ_E tongue is also an axis of maximum potential instability.

The thirteen hour forecasted divergence field (Figure 3-17d) shows an area of growing convergence to the north of Tulsa, Oklahoma (TUL) while divergence is forecasted over northeastern Texas. During the next hour the model forecasts the convergence area to grow rapidly southward into eastern Oklahoma while divergence is forecasted to prevail over northern Texas. The southward growth of this convergence area allows it to move over the axis of maximum potential instability.

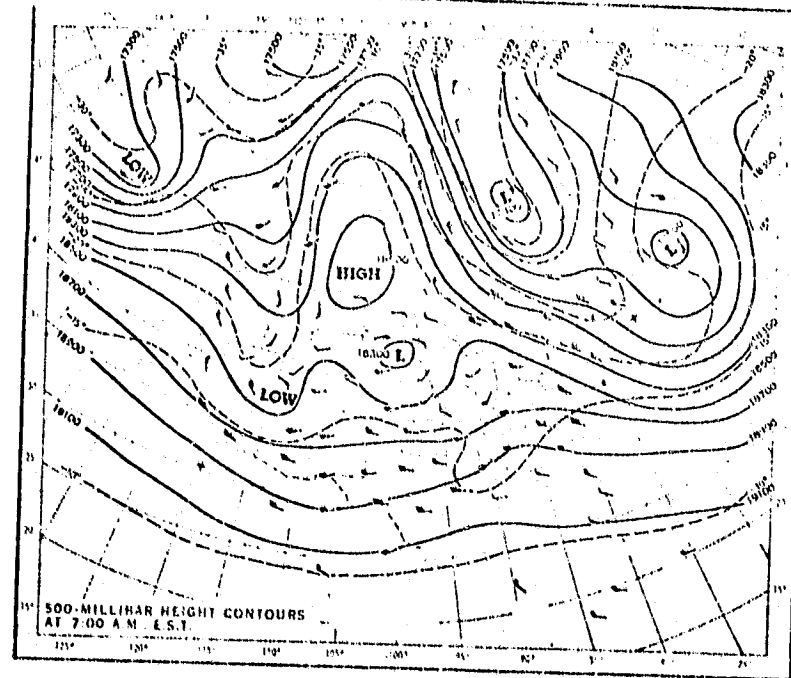
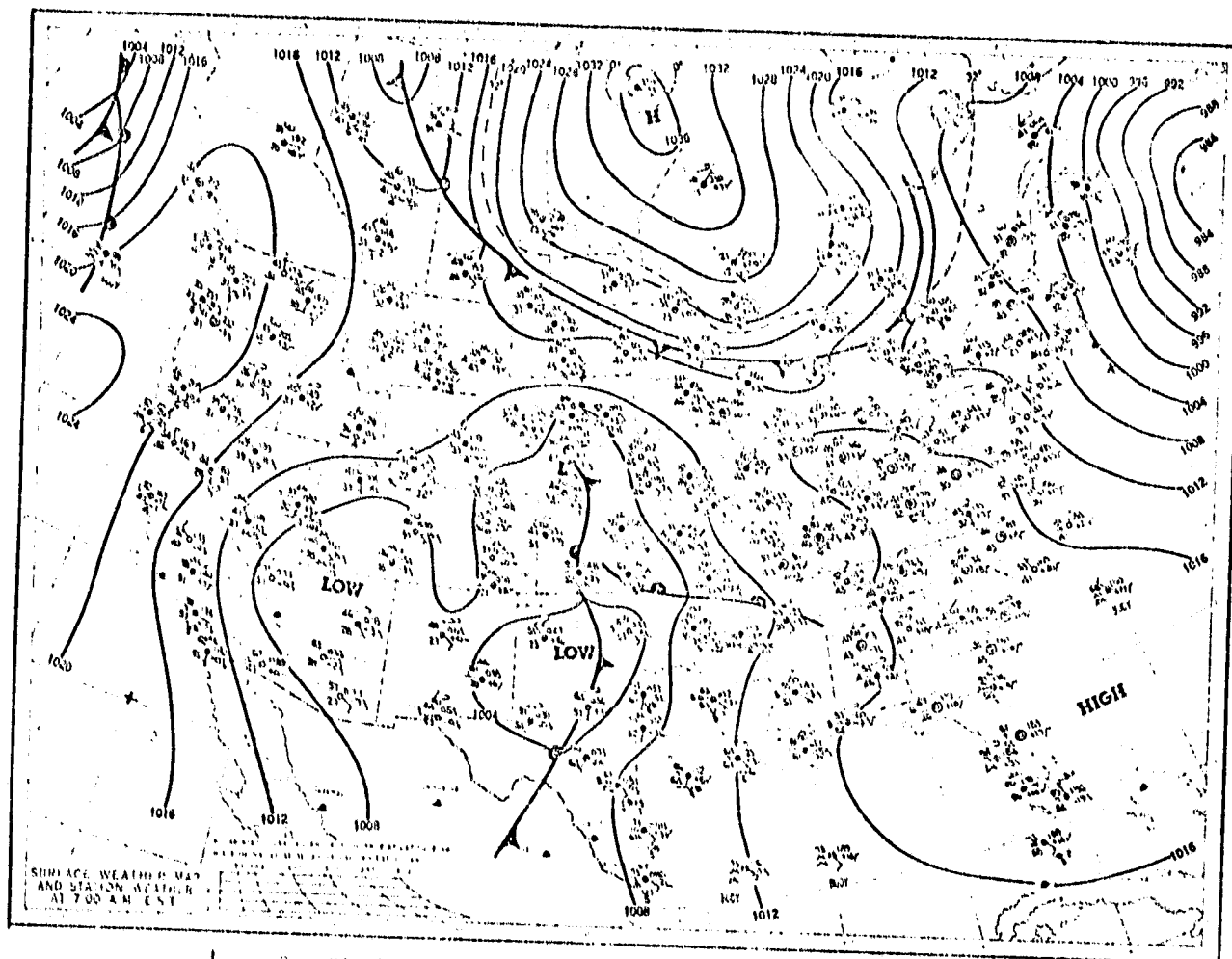
The trend of convective activity between the 2335 GMT and 0235 GMT radar summaries supports this model forecast in two ways.

The previously observed convective activity over northern Texas shows no further development during this period. The model had forecasted an increasingly divergent flow in this area. Meanwhile, convective activity explodes in the area southeast of Oklahoma City with two cells reported over 50,000 ft at 0235 GMT. This, of course, was the area over which the southward growing convergence zone became superimposed upon the axis of maximum potential instability. A comparison between the fifteen hour forecasted convergence field (Figure 3-17e) and the 0235 GMT radar summary reveals an impressive correlation over eastern Oklahoma. One convergence maxima is located slightly south of Tulsa, Oklahoma at nearly the same location as a 58,000 ft. cell while a secondary convergence maxima is located very close to the 56,000 ft. cell southeast of Ada, Oklahoma.

The fifteen hour forecasted wind field (Figure 3-17e) indicates a slight westward movement of the wave axis. The convergence area noted above is located on the eastern side of the wind shift axis. Thus, it is superimposed upon a low level southerly flow which

continues to transport warm moist air into this region. For example Ada, Oklahoma is forecasted to increase its $1150 \text{ m } \theta_E$ value from 308°K to 310°K during the 3-hour period from 0000 GMT to 0300 GMT. Thus, one might expect this area to be a zone of sustained convective activity. Indeed, even the eighteen hour forecast (0600 GMT) continues to hold the area of maximum convergence and axis of maximum potential instability over eastern Oklahoma. In addition, the southerly flow is forecasted to increase the θ_E value to near 312°K in the vicinity of Ada and McAlester, Oklahoma. The radar summaries from 0435 GMT through 0735 GMT show a continuation of the convective activity over the region designated by the model's locked-in superposition of low θ_E and convergence.

Thus, the 38 km model appeared to do very well in capturing the evolution of the convergence zone in eastern Oklahoma and the moisture transport accomplished by the southerly flow over eastern Oklahoma. Significantly, in this case, the macroscale forcing was weak. Consequently, the model did not have to contend with major movements in the synoptic weather regime during the forecast period. In addition, the area of interest was also sufficiently far from the Rocky Mountain initial data problem. Thus, in the absence of the problems previously outlined, the model does appear to capture the essence of the mesoscale organization of the quantities associated with severe local storms.



ORIGINAL PAGE IS
OF POOR QUALITY

Figure 3-13a. Top: Surface weather map for 1200 GMT 29 April 1978.
 Bottom: 500 mb chart for 1200 GMT 29 April 1978.
 Heights are labeled in feet.

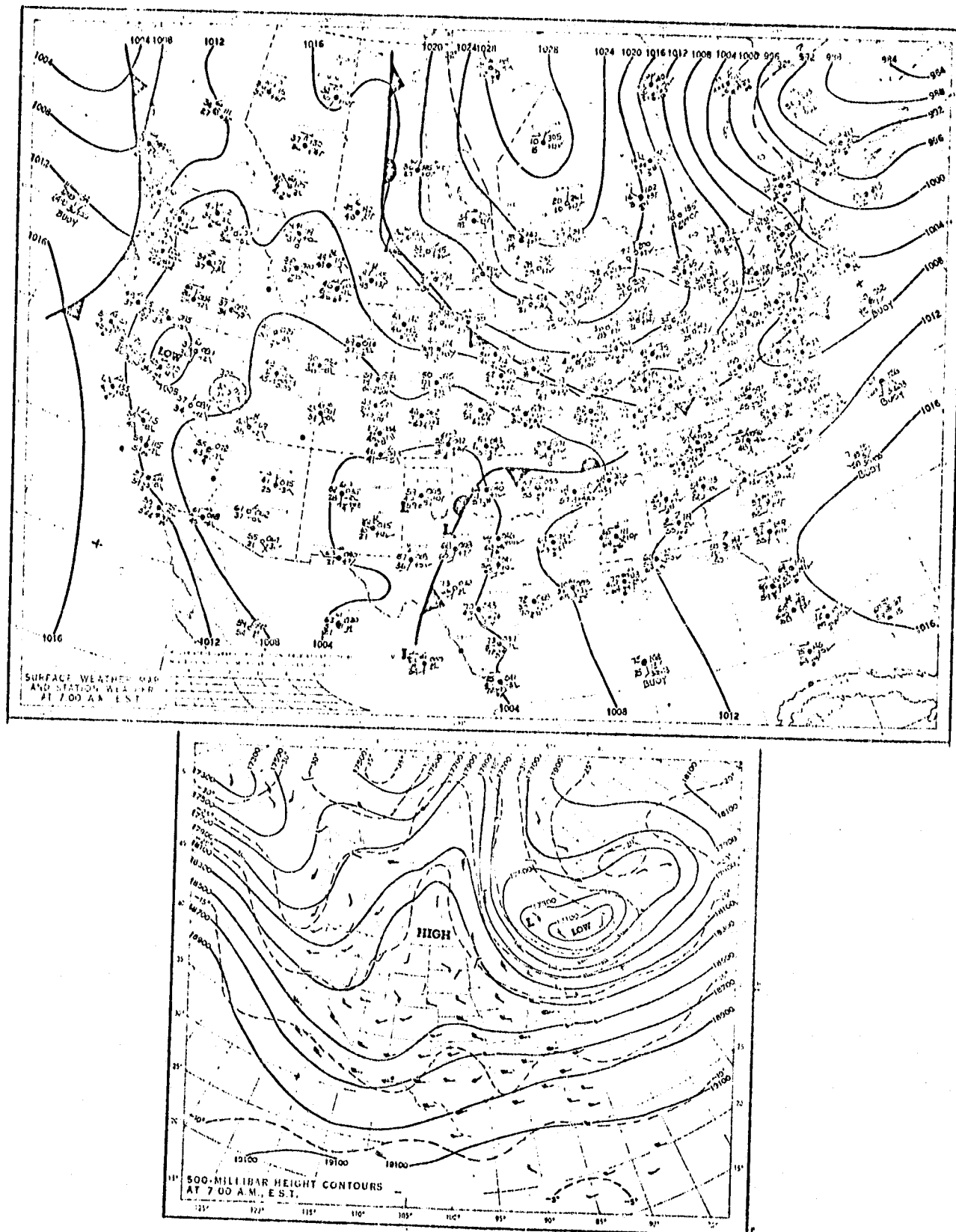


Figure 3-13b. Top: Surface weather map for 1200 GMT 30 April 1978.
 Bottom: 500 mb chart for 1200 GMT 30 April 1978.
 Heights are labeled in feet.

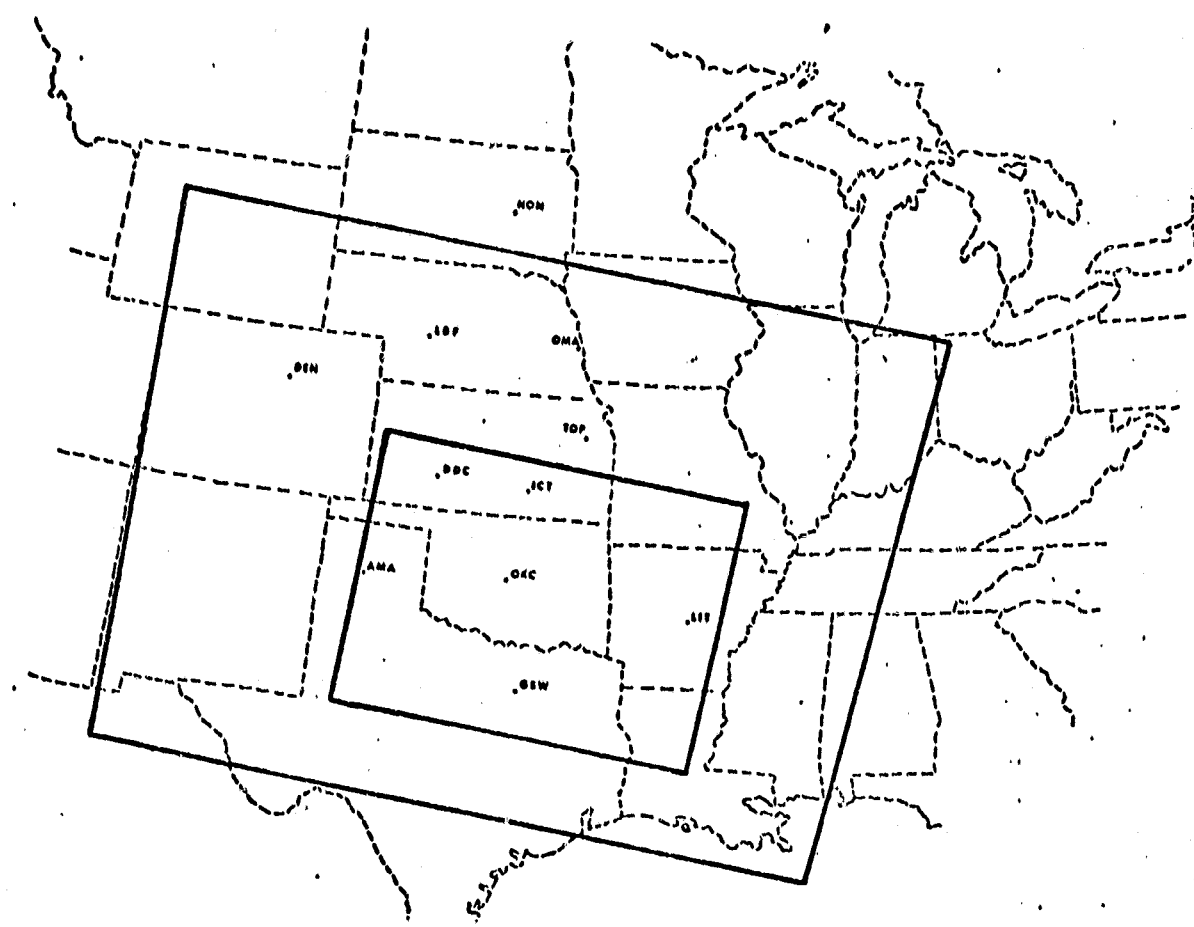


Figure 3-14. The 38 km model domain and display area for the 29 April 1978 case. The outer box demarcates the model domain. The inner box indicates the display area.

Figure 3-15a. NMC height and dew point data for the 1000 mb surface 1200 GMT 29 April 1978. Bold lines are heights in decameters. Light lines are dew points in °K.

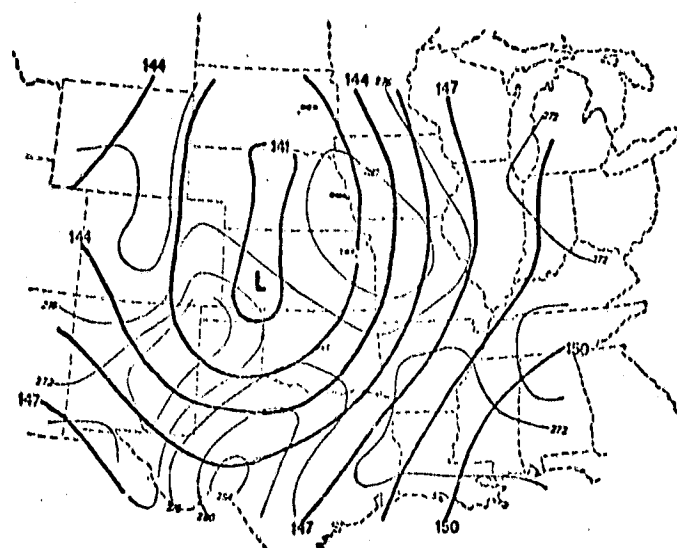
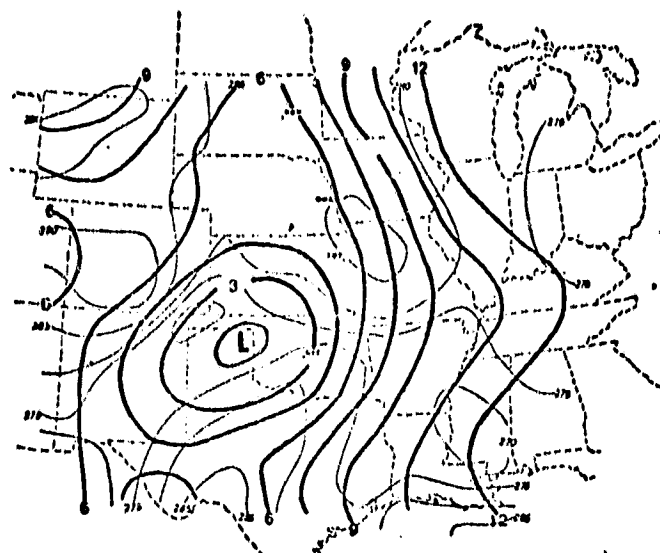
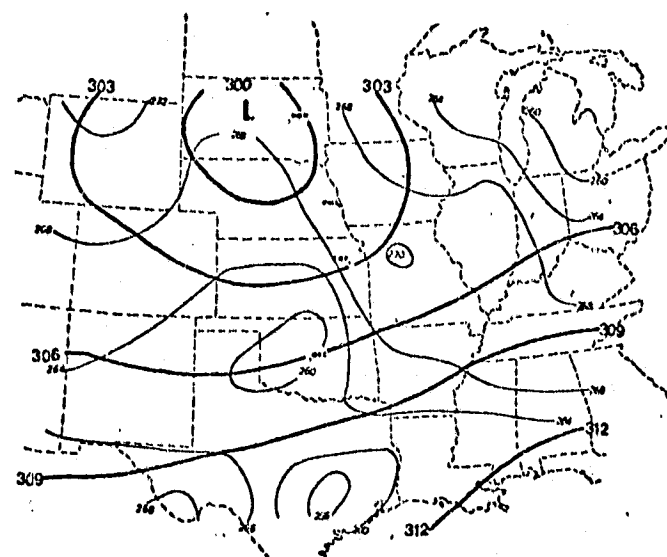


Figure 3-15b. NMC height and dew point data for the 850 mb surface 1200 GMT 29 April 1978. Bold lines are heights in decameters. Light lines are dewpoints in °K.

Figure 3-15c. NMC height and dew point data for the 700 mb surface 1200 GMT 29 April 1978. Bold lines are heights in decameters. Light lines are dew points in °K.



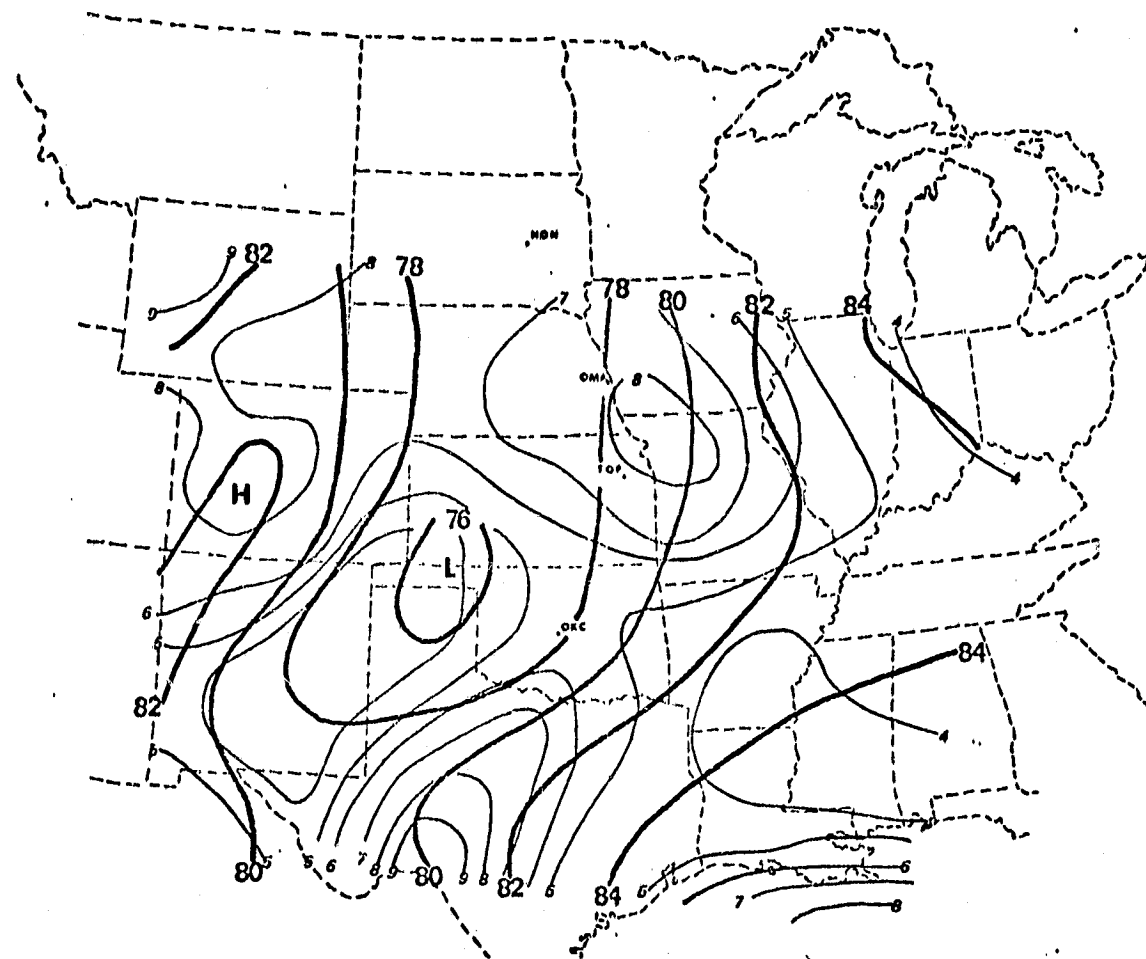


Figure 3-16. The 38 km model 1150 m initialization of pressure and mixing ratio at 1200 GMT 29 April 1978. Bold lines are isobars at intervals of 2 mb. Labels omit the preceding 8. Light lines are mixing ratios in g/kg.

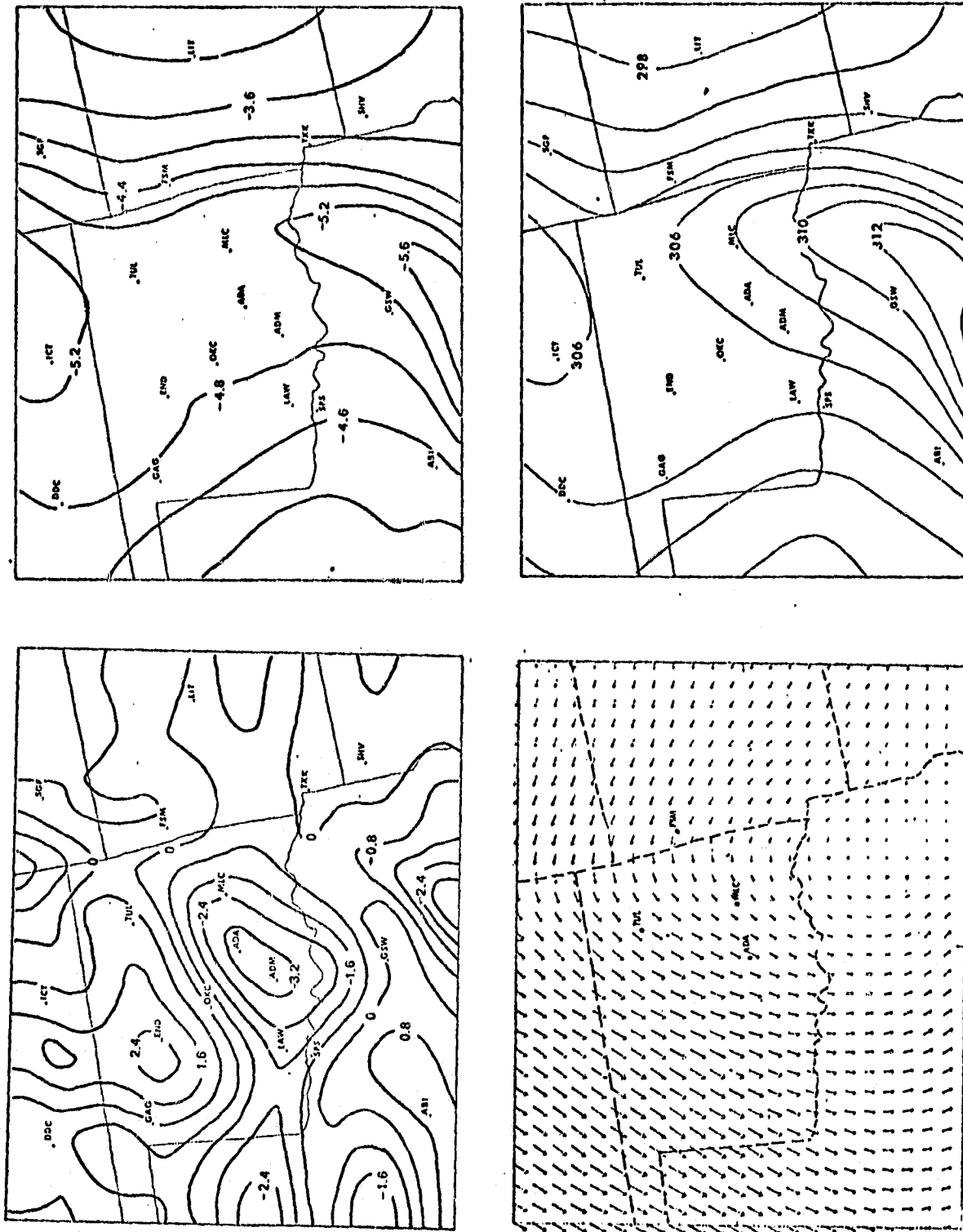


Figure 3-17a. Nine hour 1150 m model forecast valid at 2100 GMT 29 April 1978. Upper left: Divergence field at intervals of $0.8 \times 10^{-1} \text{ s}^{-1}$. Upper right: σ_E at intervals of 0.4. Lower left: Wind vectors. Lower right: θ_E at 2°K intervals.

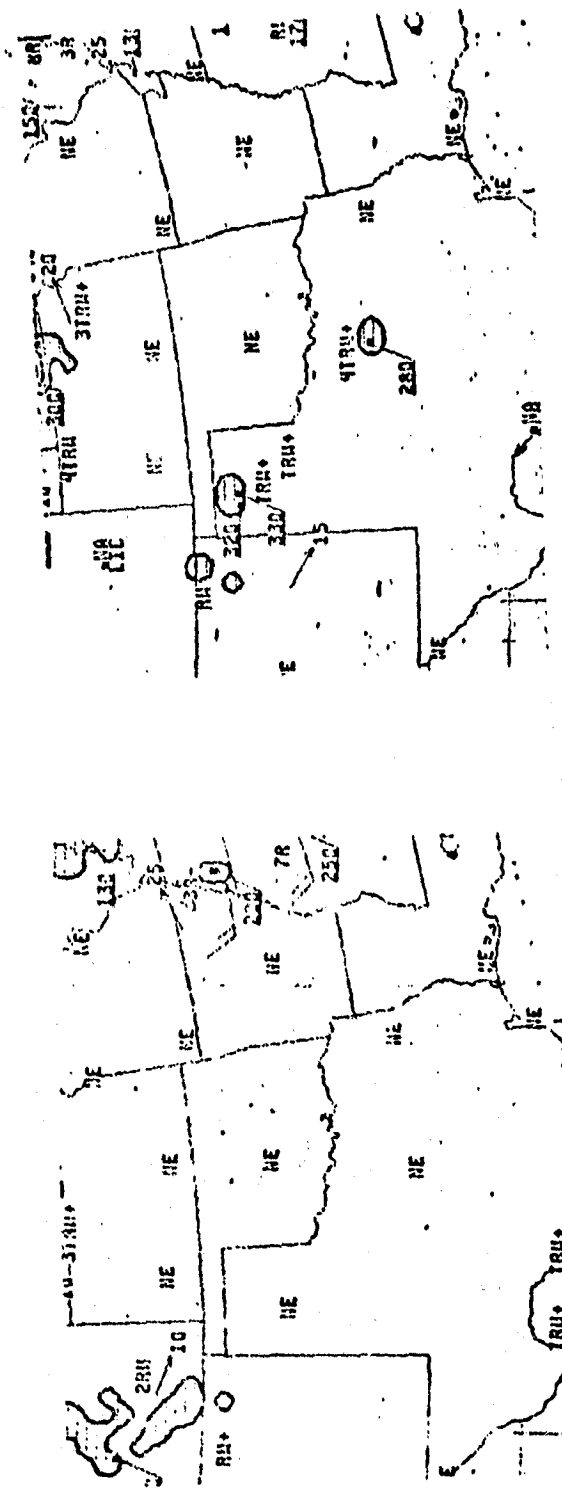


Figure 3-17b. Left: National Weather Service radar summary for 2135 GMT.
Right: National Weather Service radar summary for 2235 GMT.

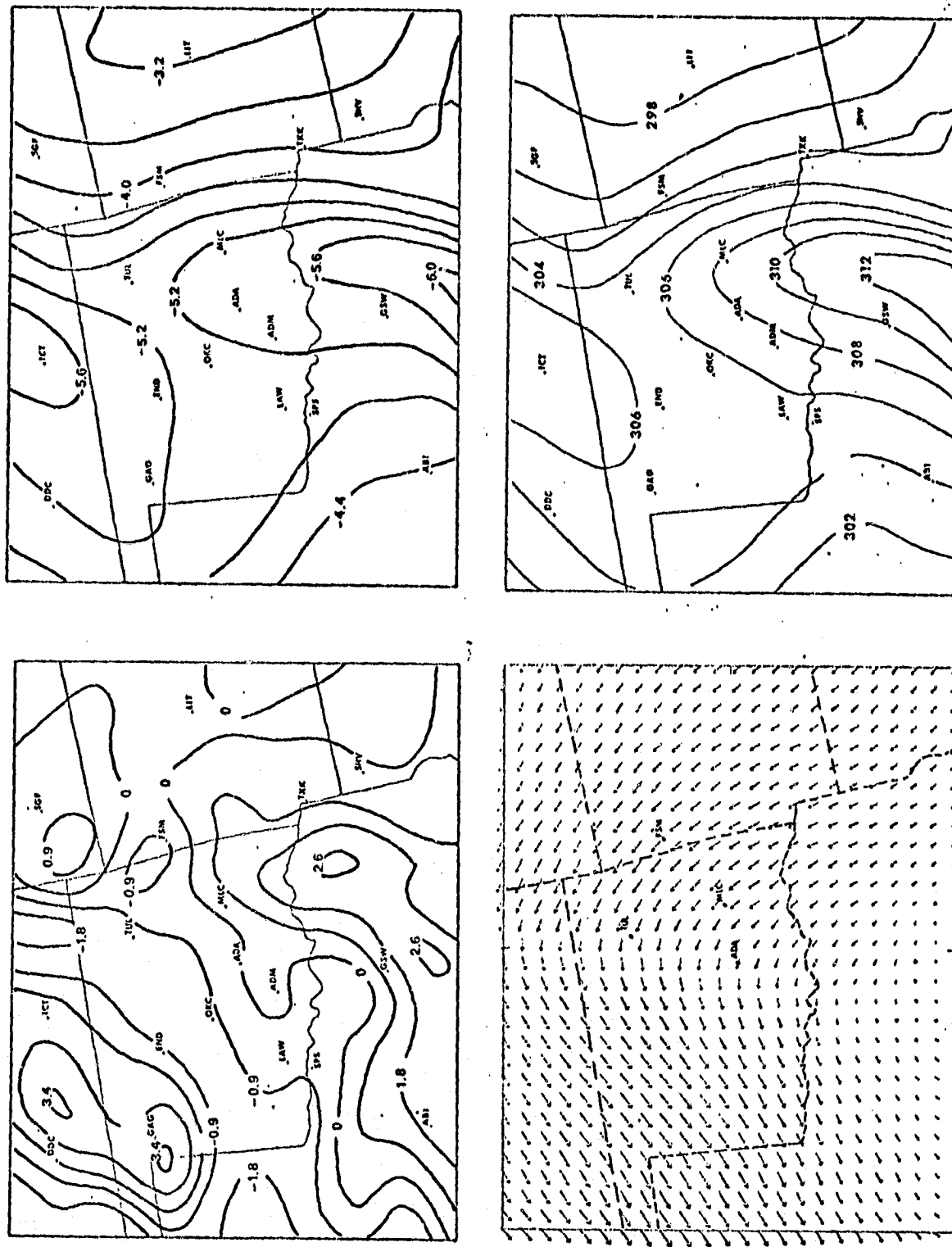


Figure 3-17c. Twelve hour 1150 m forecast valid at 0000 GMT 29 April 1978. Upper left: Divergence field at intervals of $0.9 \times 10^{-5} \text{ s}^{-1}$. Upper right: σ_E at intervals of 0.4. Lower left: Wind vectors. Lower right: θ_F at 2 K intervals.

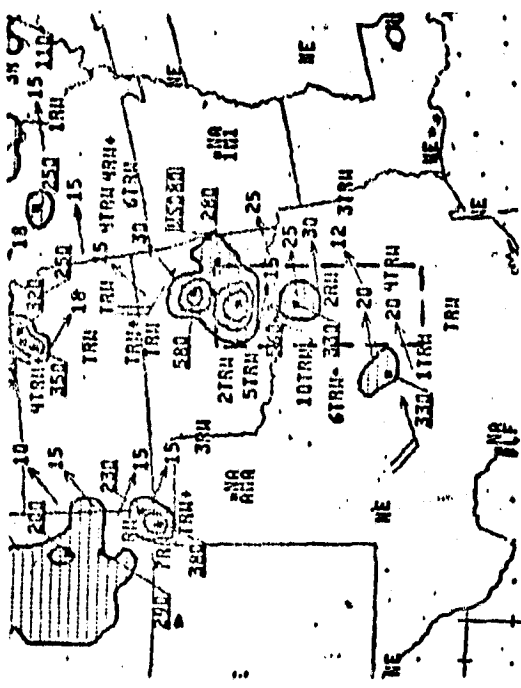
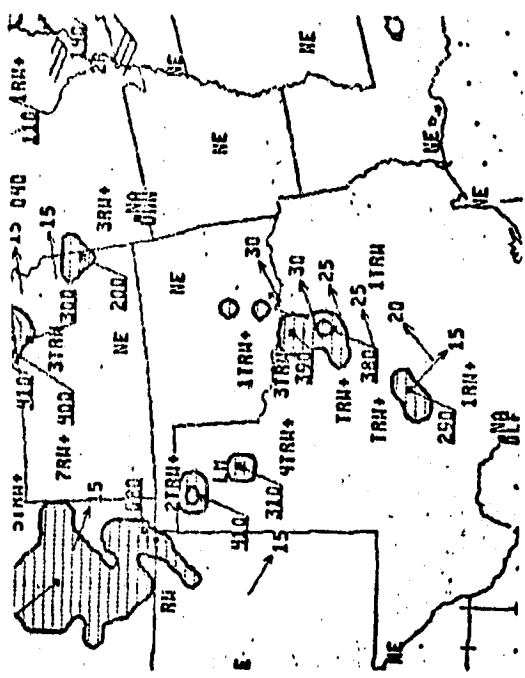
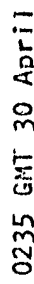
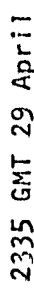
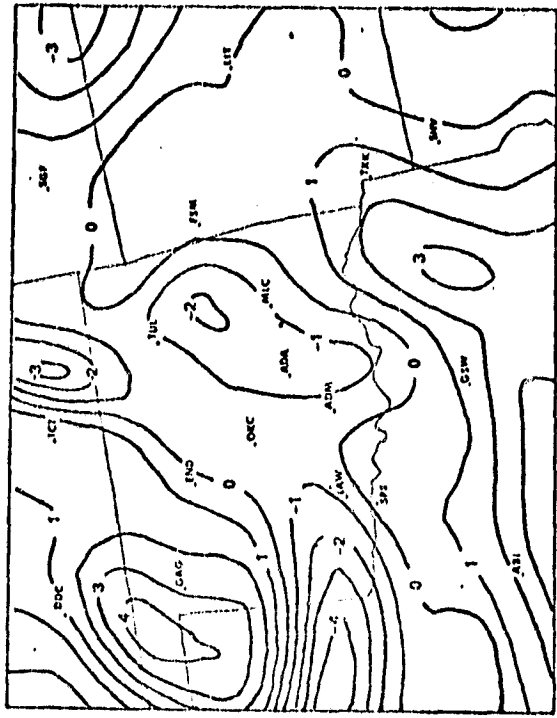
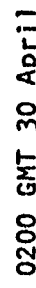
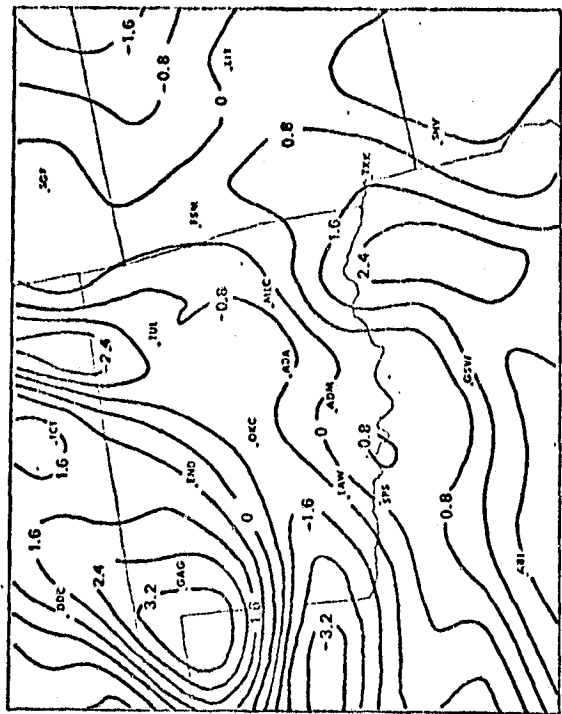


Figure 3-17d. Upper left: Thirteen hour (0100 GMT) model forecast of the 1150 m divergence. Isopleths are at intervals of $0.8 \times 10^{-5} \text{ s}^{-1}$. Upper right: Fourteen hour (0200 GMT) model forecast of the 1150 m divergence at intervals of $1 \times 10^{-5} \text{ s}^{-1}$. Lower left: NWS radar summary for 2335 GMT 29 April. Lower right: NWS radar summary for 0235 GMT 30 April.

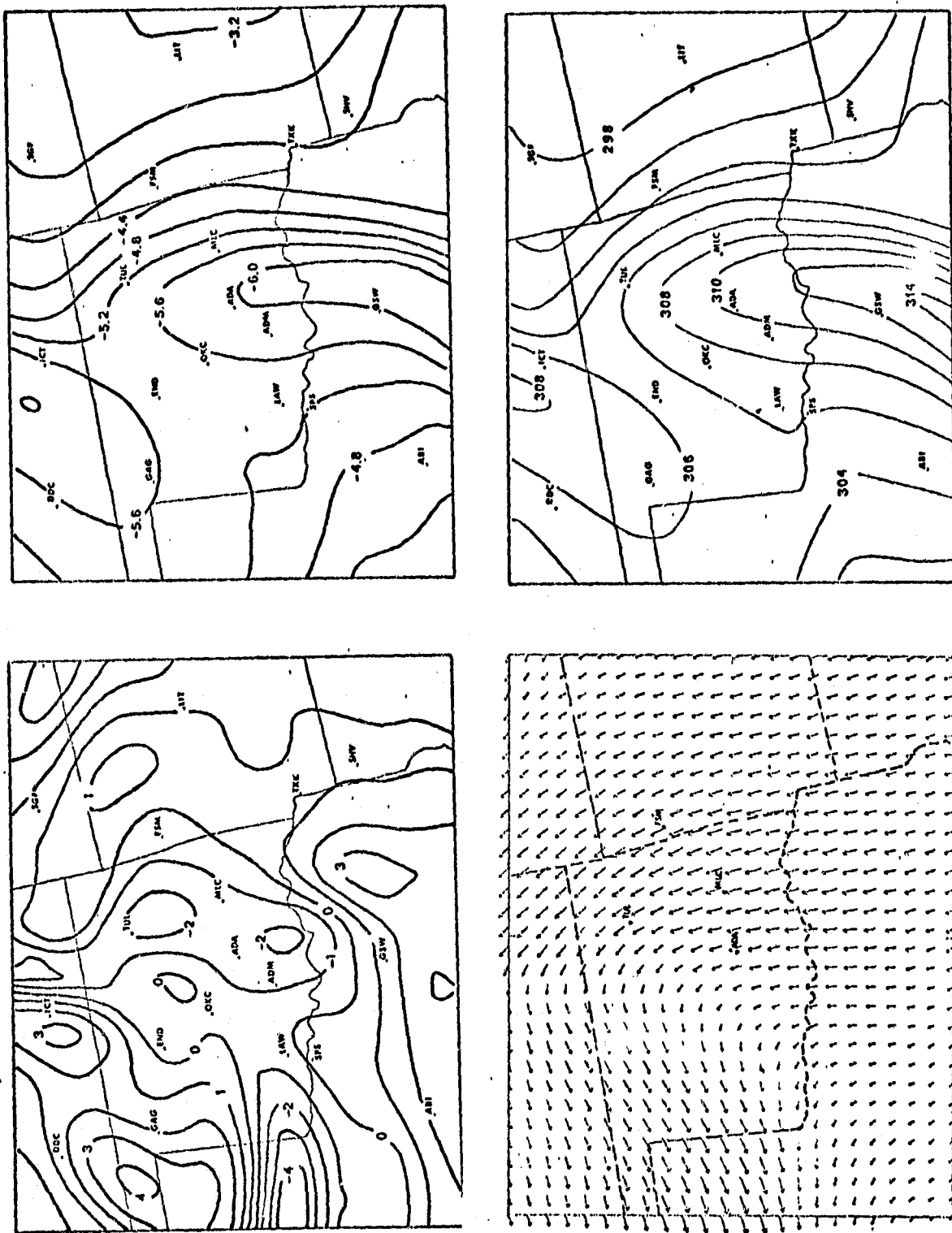


Figure 3-17e. Fifteen hour 1150 m forecast valid at 0300 GMT 30 April 1978. Upper left: Divergence at $1 \times 10^{-5} \text{ s}^{-1}$ intervals. Upper right: σ_E at 0.4 intervals. Lower left: θ_E at 2 °K intervals.

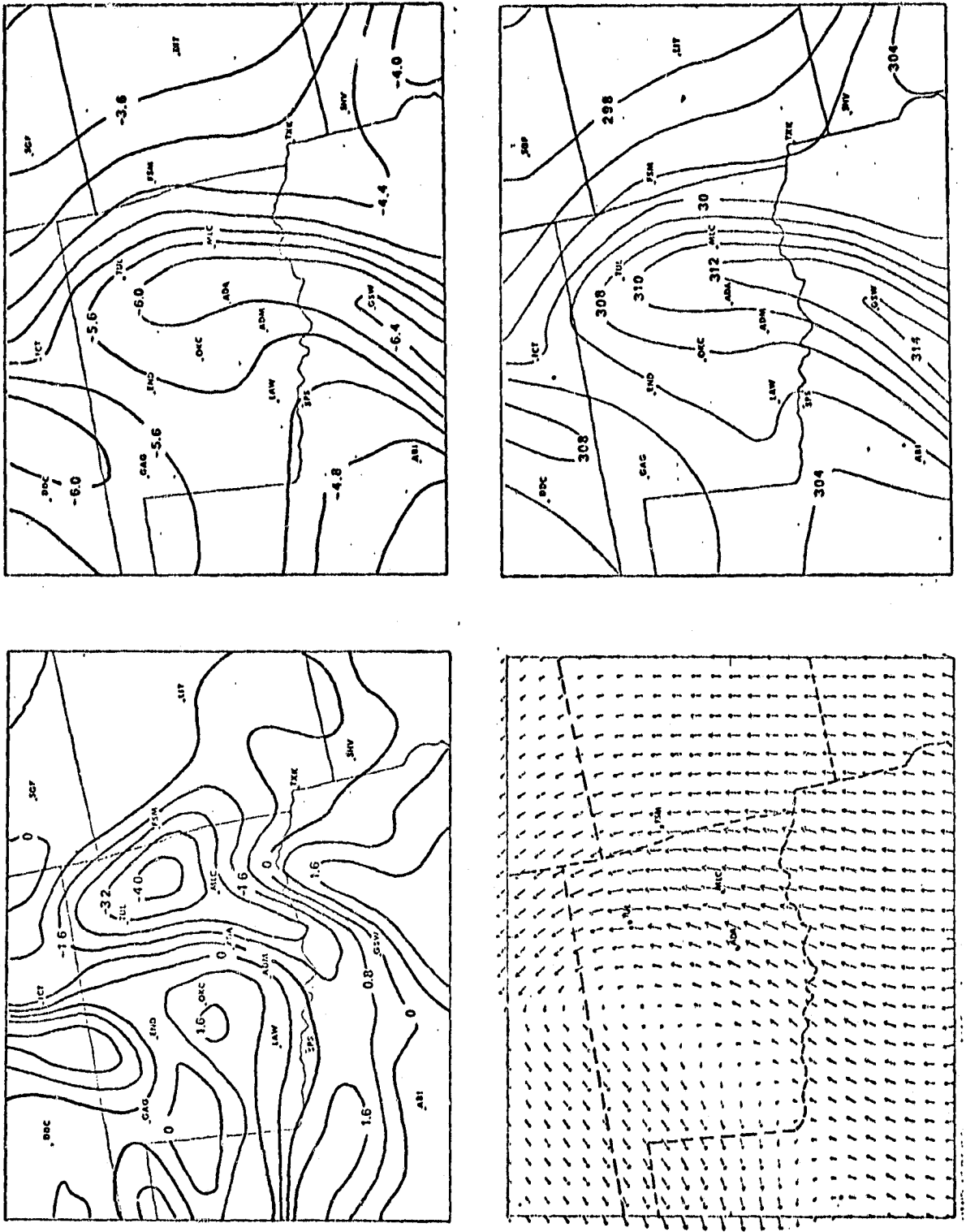
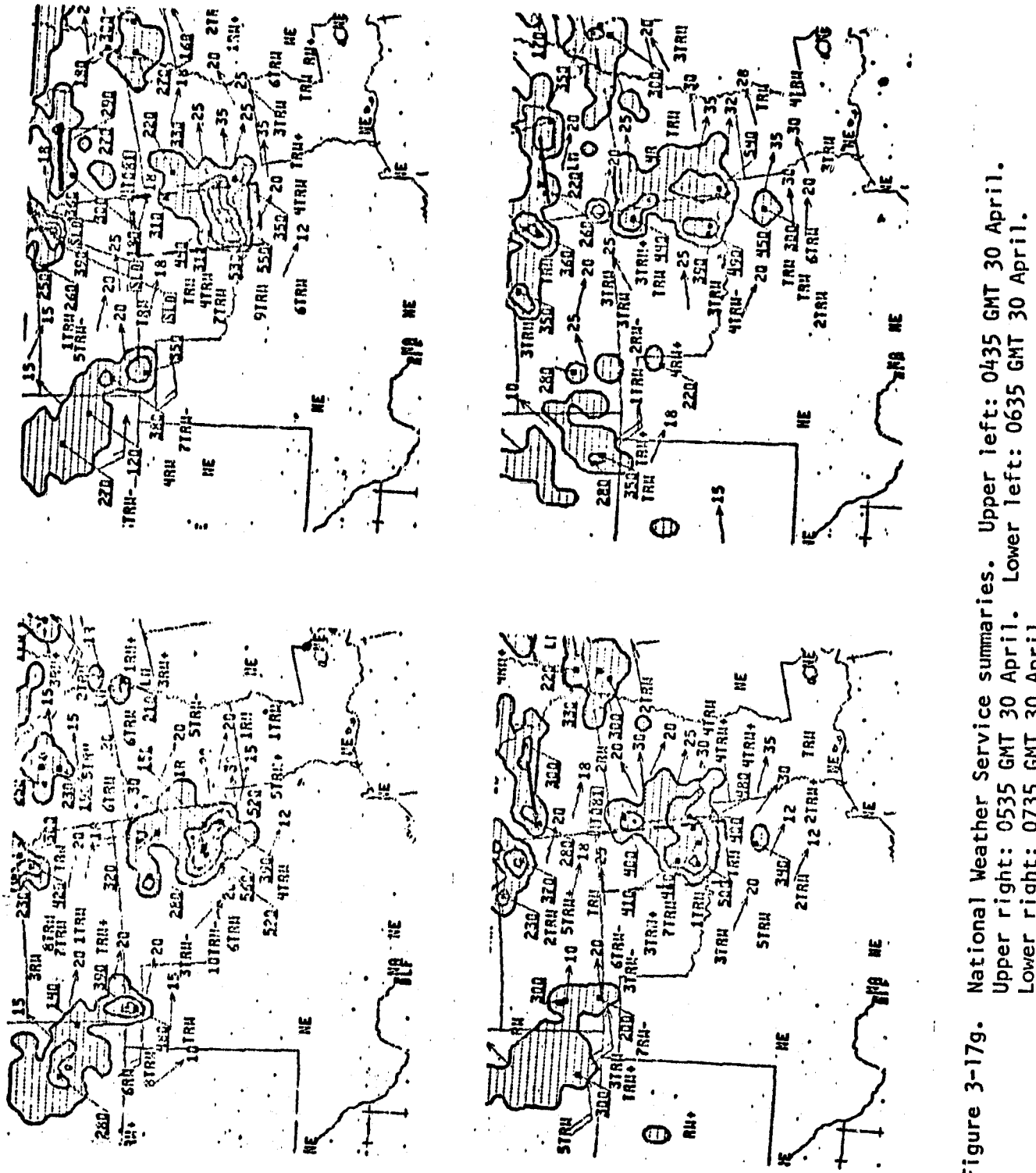


Figure 3-17f. Eighteen hour 1150 m forecast valid at 0600 GMT 30 April. Upper left: Divergence at $0.8 \times 10^{-5} \text{ s}^{-1}$ intervals. Upper right: σ_E at intervals of 0.4. Lower left: Wind vectors. Lower right: θ_E at 2°K intervals.



National Weather Service summaries. Upper left: 0435 GMT 30 April.
Upper right: 0535 GMT 30 April. Lower left: 0635 GMT 30 April.
Lower right: 0735 GMT 30 April.

**ORIGINAL PAGE IS
OF POOR QUALITY**

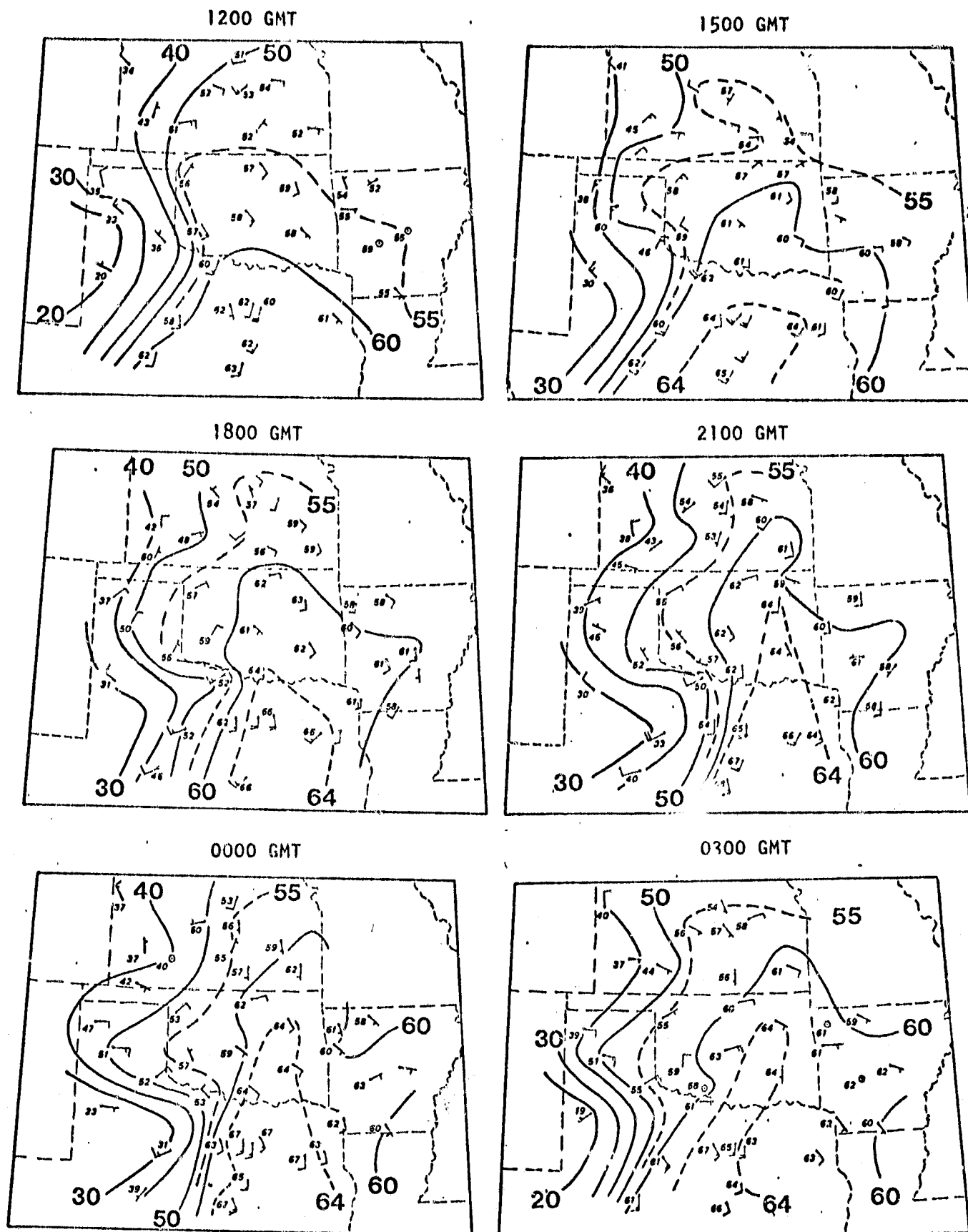


Figure 3-18. Surface dew point and wind data at three hour intervals from 1200 GMT 29 April to 0300 GMT 30 April. Solid isopleths represent dew points at 10°F intervals. Short wind bars are 5 knots. Long wind bars are 10 knots.

3.4 Case IV: 17 June 1978

The most newsworthy and tragic event of the spring 1978 tornado season occurred on the 17 June. A tornado touched down on the western portion of Pomona Lake, four miles to the north-northeast of Lyndon, Kansas at 6:15 pm CST (0015 GMT). The touch down was near the Whippoorwill Showboat and caused the boat to capsize resulting in 16 deaths and 13 reported injuries (Storm Data, June 1978). Additional reports of tornadoes, large hail and damaging winds were received from parts of eastern Kansas, northwestern Missouri and Iowa during the evening of 17 June.

The surface weather map at 1200 GMT 17 June 1978 (Figure 3-19a) indicated a quasi-stationary frontal zone from central Wisconsin through central Iowa and western Kansas to southern Colorado. Warm, moist tropical air dominated the region to the southeast of the frontal zone, while cooler and drier modified polar air was found to the northwest of the front. A secondary front separating the modified polar air from a new surge of polar air was located across northwestern Minnesota, North Dakota and eastern Montana.

The 500 mb chart for 1200 GMT 17 June 1978 (Figure 3-19a) indicated a significant trough with an axis across eastern Montana and western Wyoming. Otherwise, a slightly perturbed west-southwest flow dominated the central and eastern portions of the United States

The 38 km model was initialized over the area indicated in Figure 3-20. One should note that the model domain captures only a portion of the synoptic wave over the northern Rocky Mountain

region. Over the next twenty-four hours, this wave moves eastward and causes the surface frontal zone to translate several hundred kilometers to the east and south (Figure 3-19 b).

The NMC analysis data on the 1000 mb, 850 mb and 700 mb surfaces over the model area at 1200 GMT 17 June is reproduced in Figure 3-21. The 1000 mb height data closely resembles the sea level pressure data. However, the NMC 1000 mb data has the low height center slightly further to the north than the sea level pressure field. The 1000 mb dew points are over 290°K (17°C, 63°F) in the Rocky Mountain region and over northern Nebraska and southern South Dakota. The 1000 mb dew points to the southeast of the frontal zones are 287°K (14°C, 57°F) or below, over all of Kansas, Missouri and Oklahoma. This low level moisture distribution is somewhat different than that implied by the 1200 GMT surface weather chart. On the surface weather chart, the surface dew points range from the middle 60's to near 70°F (21°C, 294°K) over eastern Kansas and Oklahoma. In contrast, the observations recorded on the surface weather map over Nebraska and South Dakota indicate that the dew points range between 45°F (7°C, 280°K) and 55°F (13°C, 286°K) over this area. Thus, the configuration of the NMC 1000 mb dew points and the surface observed dew points appear to be noticeably different. While some of the discrepancy can be attributed to the "build-down" problem, it is not clear why the 1000 mb dew point field underestimates the surface dew points by 5°C or more over the relatively low areas in Oklahoma and eastern Kansas.

The 1150 m model initialization data is presented in Figure 3-22. A low pressure center is located over central Nebraska with a pressure trough extending from southern Minnesota to eastern

Colorado. Southeast of this trough a tongue of warm air stretches from the southwestern U.S. to the northern Midwest. The mixing ratio field indicates that the greatest low level moisture (13.4 g/kg) is located over northern Illinois and eastern Iowa and a secondary 12.4 g/kg maxima is located over extreme northern Nebraska. The 1150 meter air over eastern Oklahoma and Kansas is initialized to be somewhat drier than that over northern Nebraska.

Several areas of misrepresentation in the initial data field are revealed if one examines the actual radiosonde data recorded just before 1200 GMT 17 June at Topeka, Kansas (TOP), Omaha, Nebraska (OMA), Huron, South Dakota (HON) and Oklahoma City, Oklahoma (OKC) (Figure 3-23). The radiosonde data indicates that the 850 mb dew points are near 286.5°K at OKC while the NMC analysis data specifies a dew point of 284°K at 850 mb over OKC. The TOP and OMA sounding data indicate that the NMC analysis data has only overestimated the 850 mb dew points at these locations by approximately 2°K. However, at HON the 850 mb dew point was observed to be 277°K, while the NMC data specifies a value near 286°K.

It is apparent that the NMC analysis procedure has increased the low level dew points in the cold air to the north and west of the low level pressure trough and decreased the dew point values in the warm air to the southeast of the pressure trough. This may be a result of sub' sing the dew point data to a large scale smoothing process. This alteration in the low level moisture field will act to increase the initial diagnosed potential instability in the cold air to the north of the frontal zone and to underrepresent the potential instability in the warm moist air to the southeast of the frontal zone.

The TOP sounding also illustrates the necessity of adequate model resolution within the lowest atmospheric levels. The moist layer ($>13 \text{ g/kg}$) at TOP is confined to the region below 900 mb. The lowest model level (1150 m) over TOP at this time is on the 887 mb surface. Thus, in this case, the lowest model level is actually above the low level moist layer. The effect of this under-representation of the moisture field may not be serious at the larger scales. However, it may be crucial at smaller scales where latent heating exerts a significant influence. The three hour (1500 GMT) forecast depicted in Figure 3-24 indicates large negative values of σ_E over northern Nebraska. These are a result of the incorrect low level moisture representation in this area. A band of low σ_E values from western Oklahoma to northeastern Kansas is relatively unimpressive by comparison. However, this is the zone of actual maximum potential instability. The three hour forecast also indicates the existence of a weak convergence area from western Oklahoma across eastern Kansas and into Iowa. The wind vector and pressure fields place the 1150 m trough, or frontal zone, from Sioux City, South Dakota (SUX) southwestward to a point just to the east of North Platte, Nebraska (LBF). The 1500 GMT surface wind reports (Figure 3-26a) place the frontal zone just to the southeast of the model position. This discrepancy can, in part, be explained by the slope of the frontal zone from the southeast to the northwest with height. Strong southwesterly flow is forecasted across eastern Kansas, Oklahoma, Iowa and Missouri. The convergence zone previously noted is positioned along the zone where westerly winds over western Kansas intersect the southwesterly flow in eastern Kansas.

By six hours into the model forecast (1800 GMT) northerly momentum has penetrated southward into northwestern and north central Kansas. This has established a band of convergence from Dodge City, Kansas (DDC) northeastward into western Iowa. The surface weather map at 1800 GMT (Figure 3-26a) implies a band of convergence located slightly to the southeast of the model's 6 hour forecast position.

However, at nine hours (2100 GMT) into the model forecast (Figure 3-24c) the convergence zone across Kansas and north central Oklahoma has begun to diminish, while a new convergence zone becomes established over northern Nebraska in advance of an increasing northerly wind component. The pressure trough has not moved appreciably to the east during the 6 to 9 hour model forecast, and has allowed continued generation of northerly momentum to the north of the trough and southerly momentum to the south of the trough. The lack of eastward progression may be attributed to the limited model domain and its inability to capture the continued synoptic advection processes beyond 6 to 8 hours into the model forecast. The nine hours σ_E forecast (Figure 3-24c) indicates the maximum area of potential instability is located across Nebraska with a secondary, much less impressive band across Kansas and Oklahoma. It is in this secondary band that the 2035 GMT radar summary (Figure 3-25b) indicates the eruption of convection from western Kansas to central Iowa. This convective area grows steadily in intensity and expands in areal coverage over the next two hours.

Twelve hours into the model forecast (00 GMT) the southerly momentum has returned to places in extreme southeastern Nebraska and northern Kansas.

For example, Concordia, Kansas (CNK) which had shifted from a southwesterly 1150 m wind to a northwest wind at 6 hours into the forecast, has returned to a southerly wind by the twelve hour mark.

This, is a result of the lack of eastward propagation of the pressure trough associated with the synoptic wave movement to the east. The pressure falls to the southeast of the 1150 m pressure trough during the first six hours of the model forecast increased the southerly momentum through the generation of an isallobaric wind. The convergence associated with this isallobaric wind most likely prevented the pressure wave from propagating further to the southeast. In reality, the synoptic wave continued to advect these features to the east. Thus, the lack of simulation of the synoptic advection retarded the eastward propagation and organized a band convergence across eastern Nebraska and western Kansas by 12 hours into the forecast. This was associated with a sustained north-south pressure gradient which caused the generation of a northerly momentum surge across Nebraska. The 0035 GMT radar summary shows the rapid growth of convection to the southwest from 2235 to 0035 GMT from southeastern Kansas and northwestern Oklahoma into the Texas panhandle. The convergence which develops in Nebraska also grows to the southwest during this same time period.

The 15 hour (0300 GMT) and 18 hour (0600 GMT) model forecast also indicates only slow southeastward movement of the convergence zone. The radar summaries during this period also indicate slow southeastward propagation of the convective activity, but of course, it is located some 200 km southeast of the model forecast.

In summary, the model forecast for the 17 June 1978 did correctly forecast the dynamical evolution of a convergence area

across Kansas during the first 6 hours of the model simulation.

However, the subsequent model forecast was degraded by two factors:

- (1) The limited domain of the model prevented the model from simulating the synoptic advection of the sub-synoptic and mesoscale features to the east.
- (2) The initial NMC moisture data was not consistent with the actual moisture distribution.

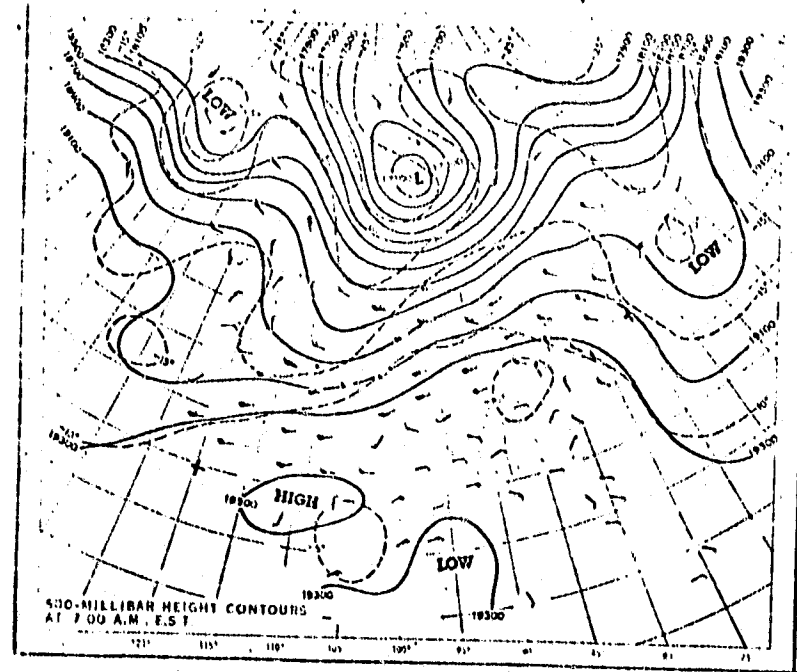
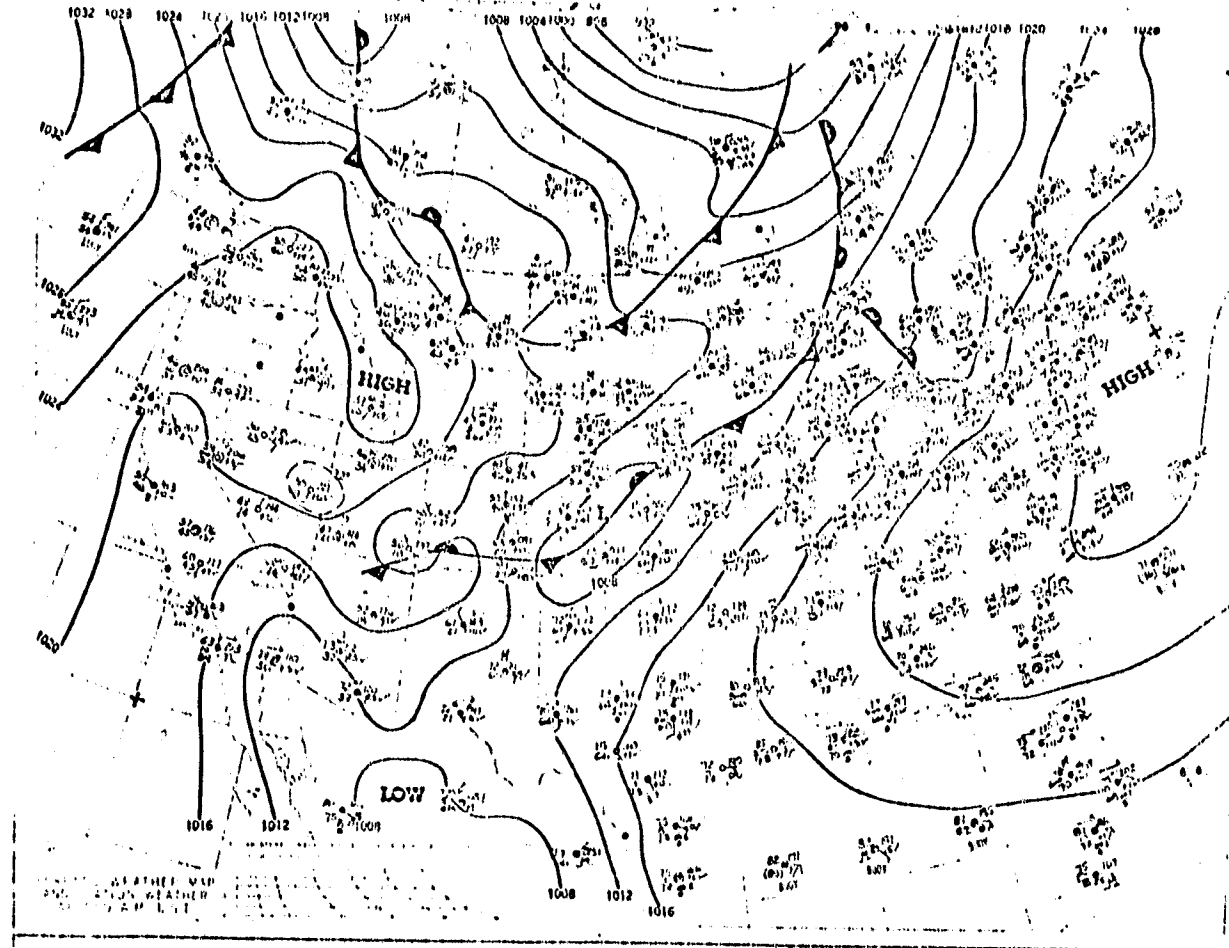


Figure 3-19a. Top: Surface weather map for 1200 GMT 17 June 1978.
Bottom: 500 mb chart for 1200 GMT 17 June 1978.
Heights are labeled in feet.

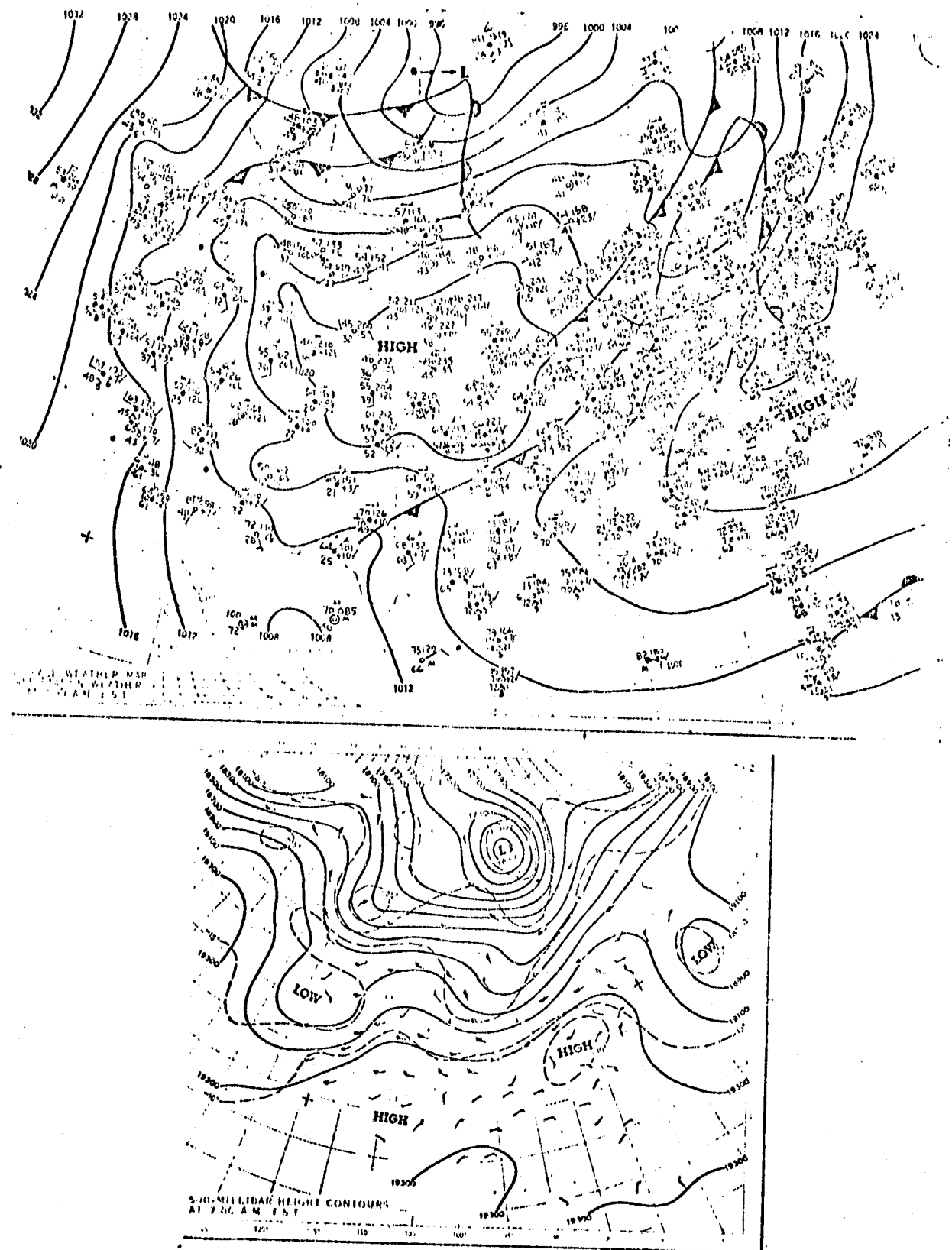


Figure 3-19b. Top: Surface weather map for 1200 GMT 18 June 1978.
 Bottom: 500 mb chart for 1200 GMT 18 June 1978.
 Heights are labeled in feet.

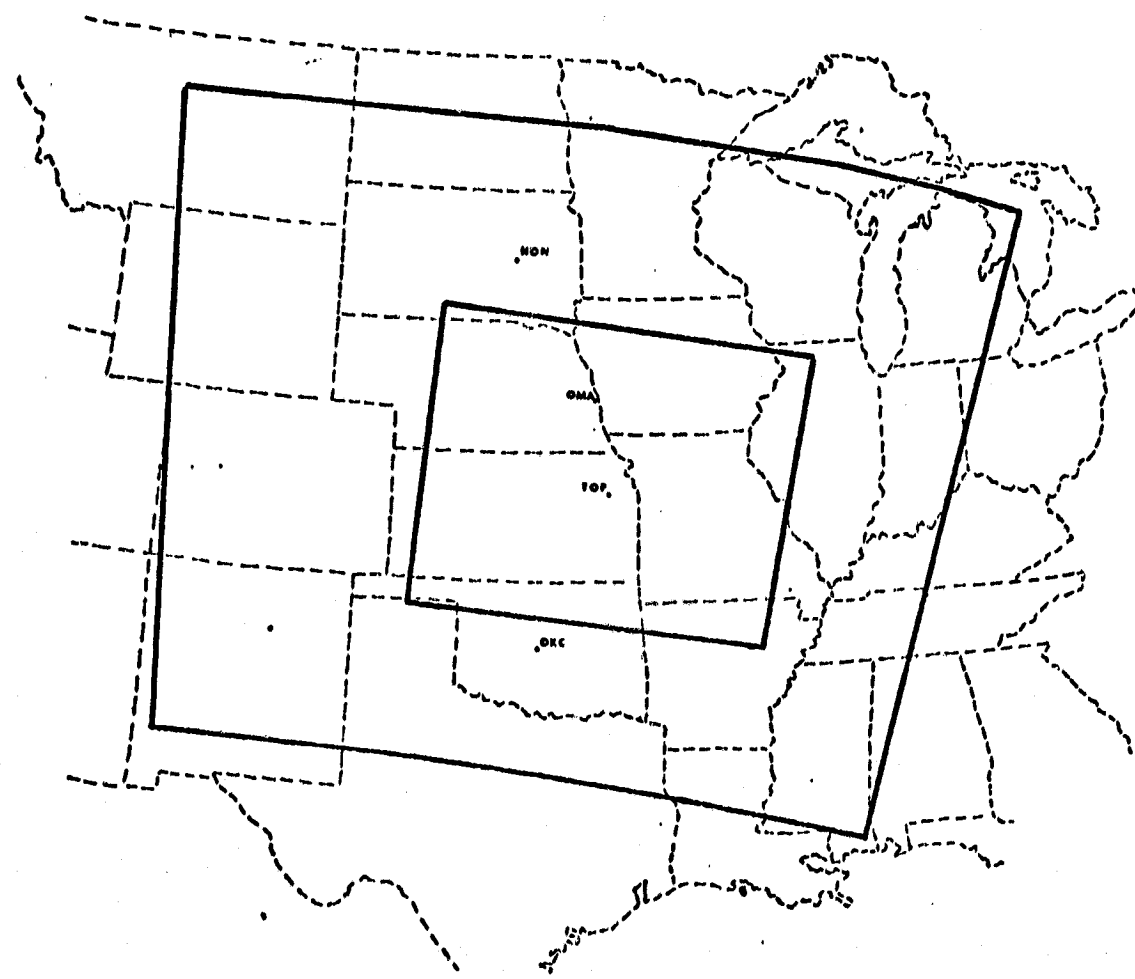


Figure 3-20. The 38 km model domain and display area for the 17 June 1978 case. Outer box indicates the extent of the model domain. Inner box demarcates the display area.

Figure 3-21a. NMC 1000 mb height and dew point data for 17 June 1978. Bold lines are heights in decameters. Light lines are dew points in °K.

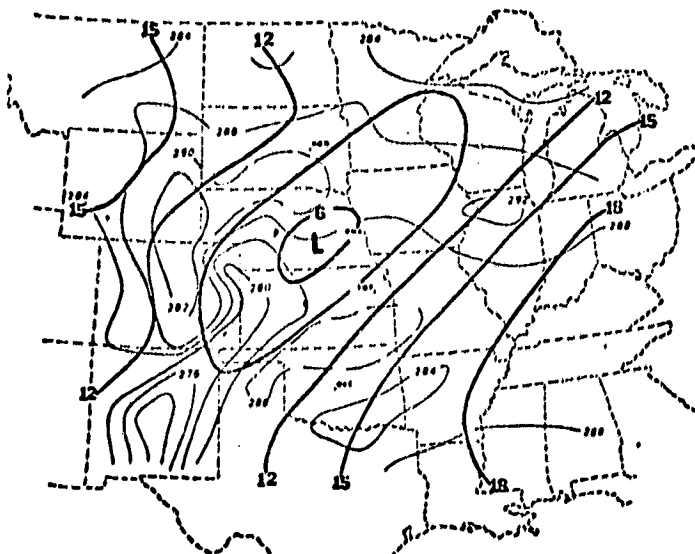


Figure 3-21b. NMC 850 mb height and dew point data for 17 June 1978.
Bold lines are heights in decameters.
Light lines are dew points in °K.

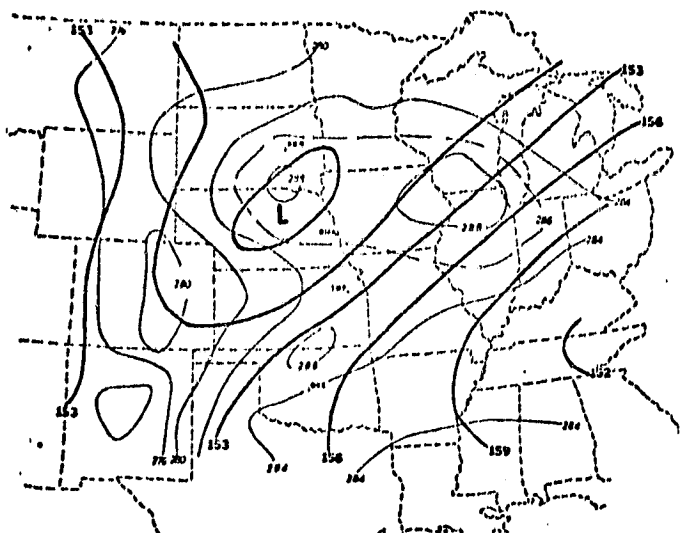
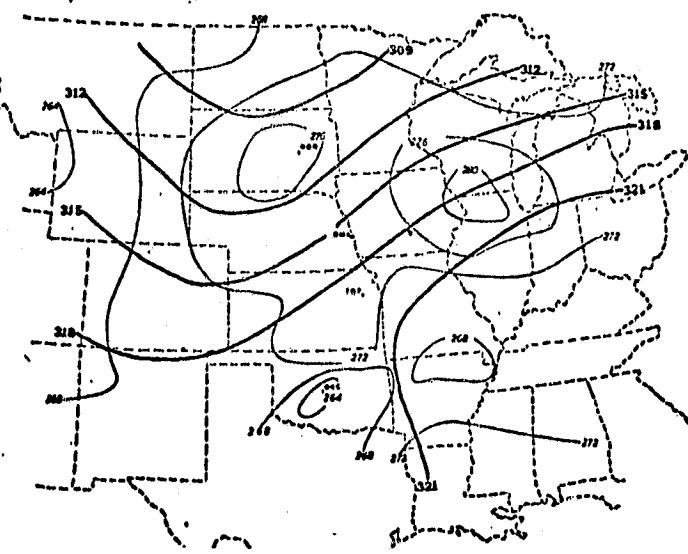


Figure 3-21c. NMC 700 mb height and dew point data for 17 June 1978.
Bold lines are heights in decameters.
Light lines are dew points in °K.



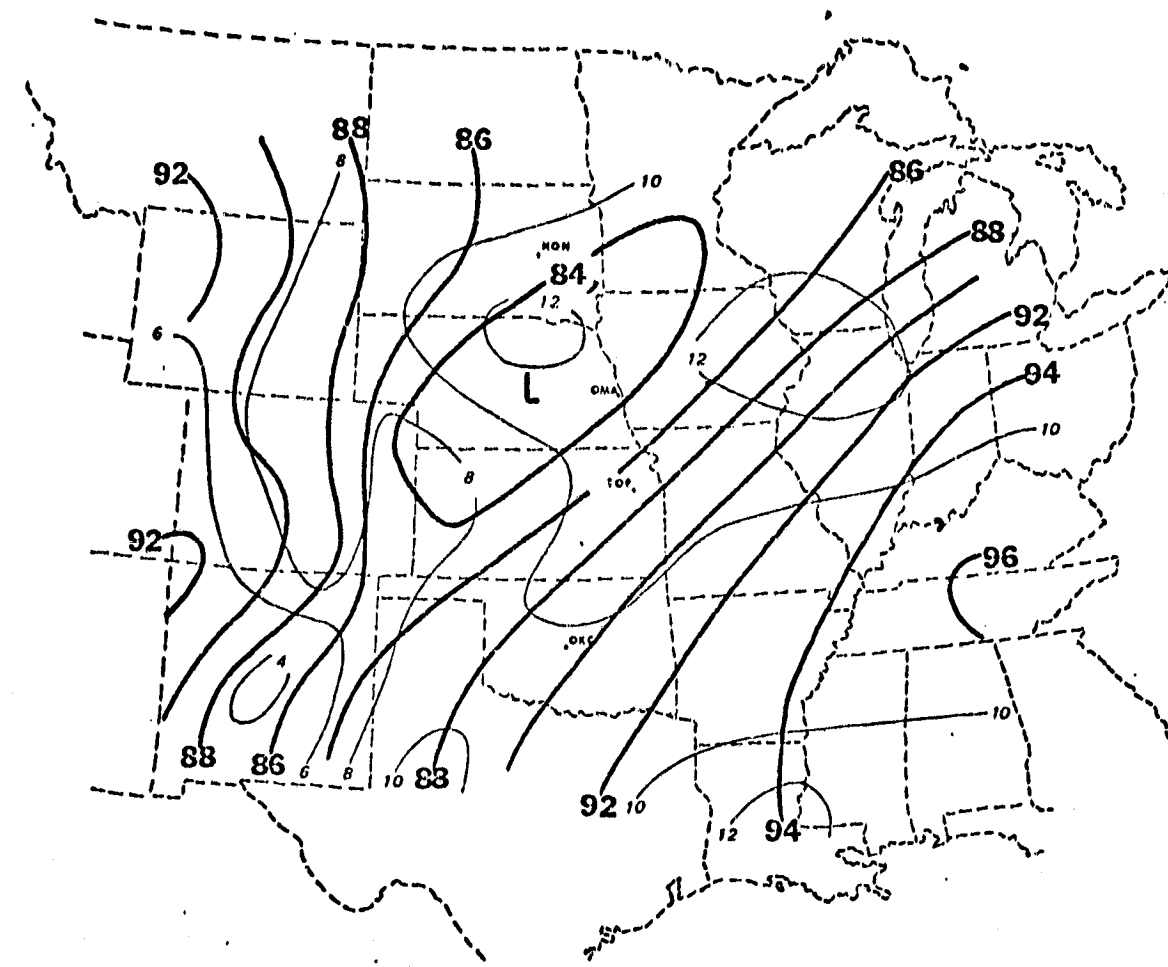


Figure 3-22. The 1150 m model initialization of pressure and dew point at 1200 GMT 17 June 1978. Bold lines are isobars at 2 mb intervals. The labels omit the preceding 8. Light lines are mixing ratio values isoplethed at 2 g/kg intervals.

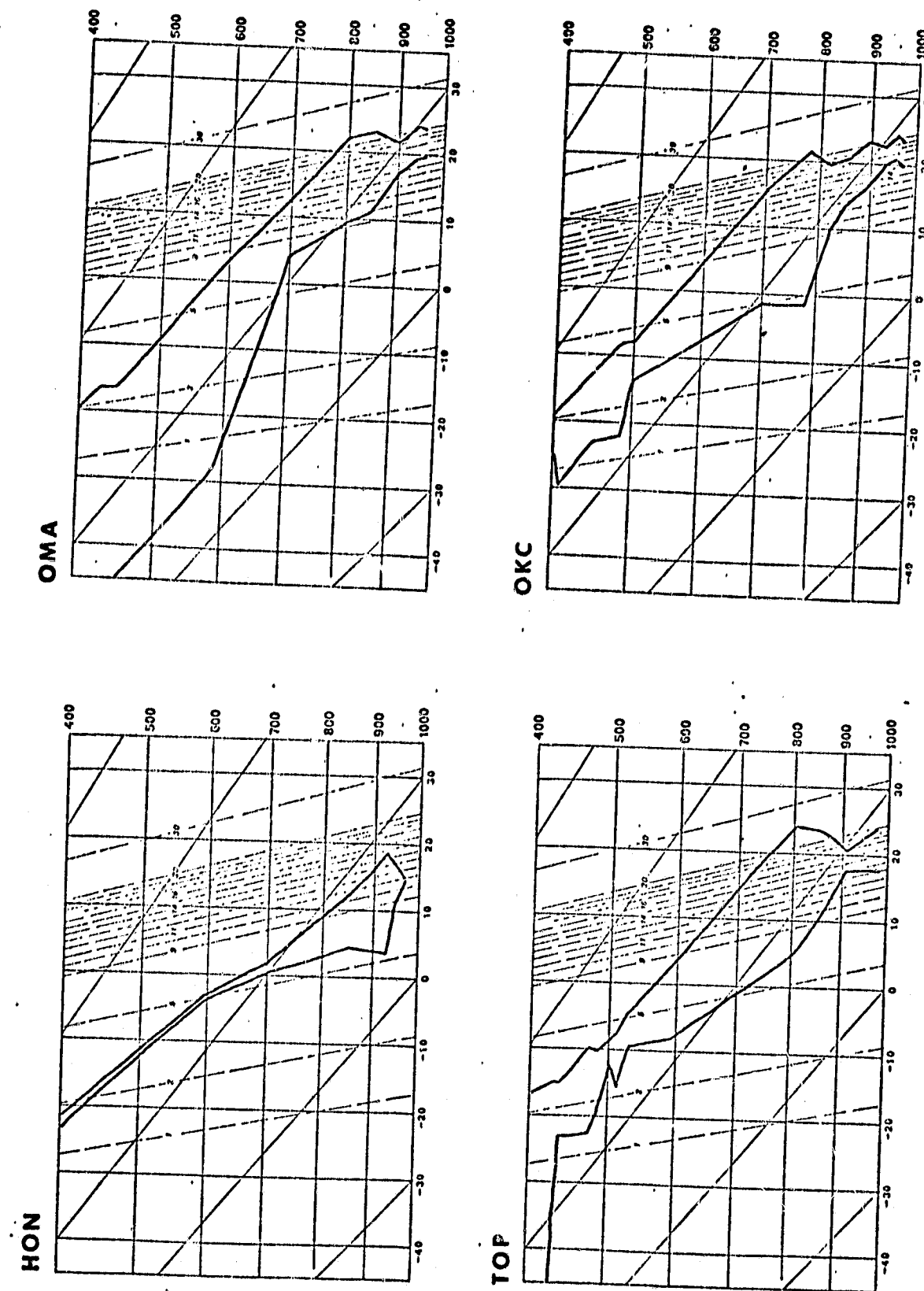
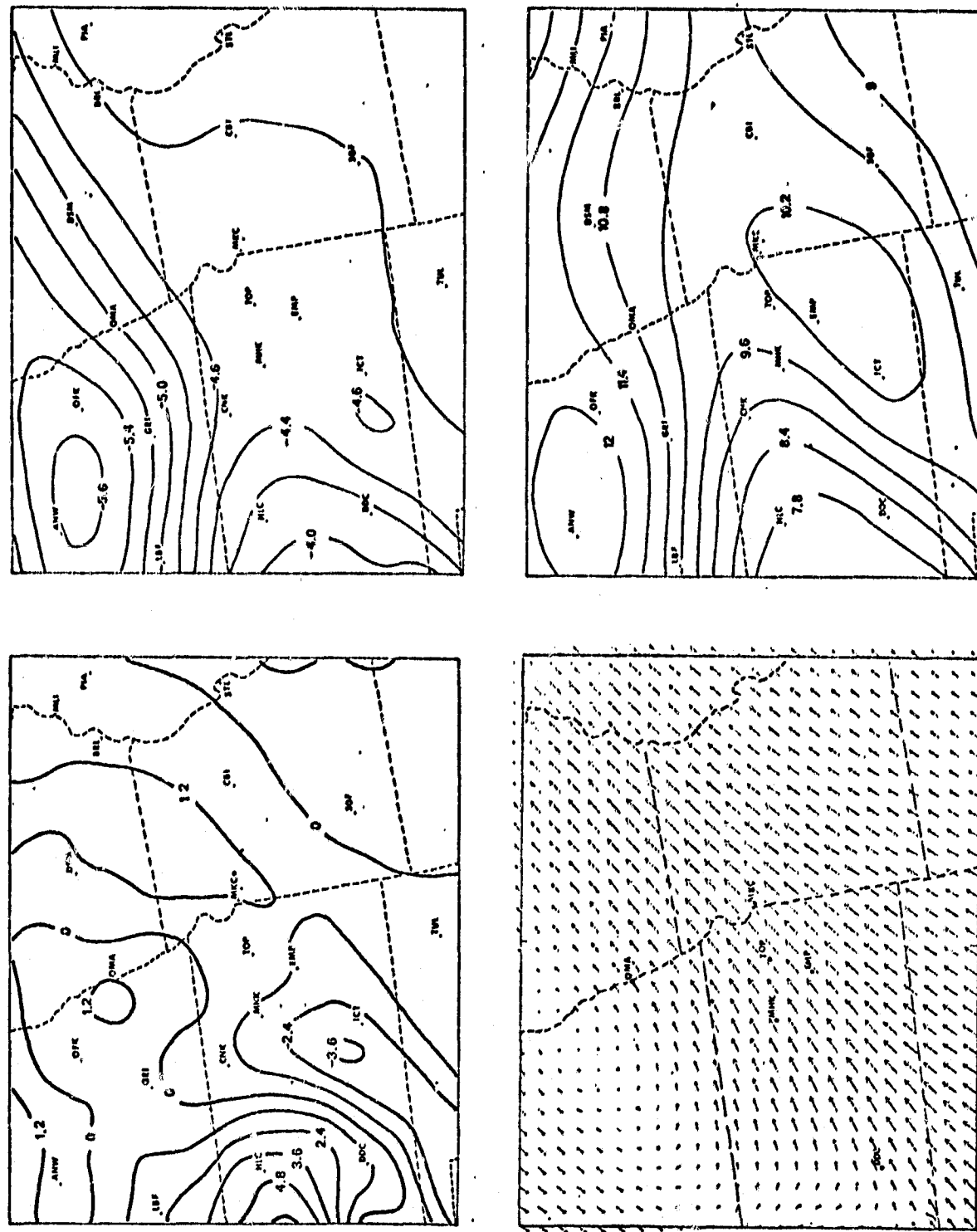


Figure 3-23. Radiosonde data at 1200 GMT 17 June 1978 for Huron, S.D. (HON), Omaha, Nb. (OMA), Topeka, Ka. (TOP) and Oklahoma City, Okla. (OKC). Abscissa are temperatures in °C and ordinates are pressure in millibars. Sloping dashed lines are constant mixing ratio curves labeled in g/kg. Sloping solid lines are dry adiabats.



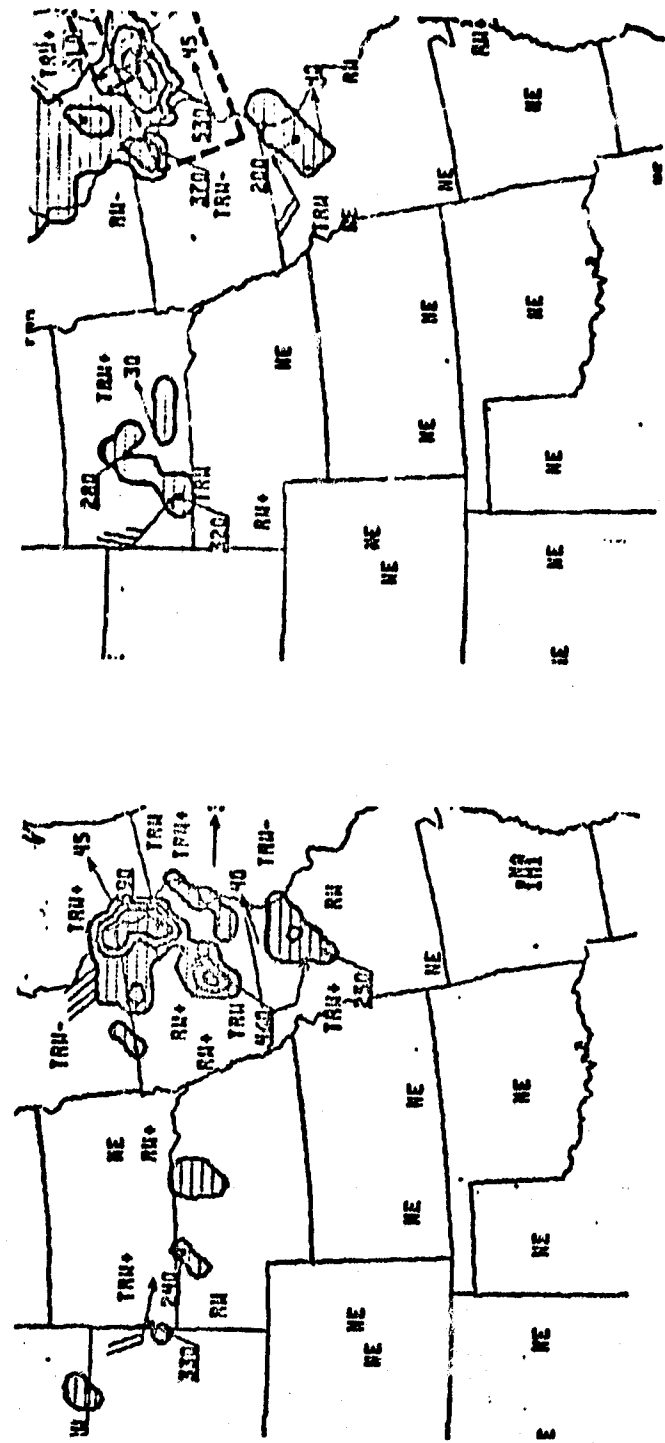
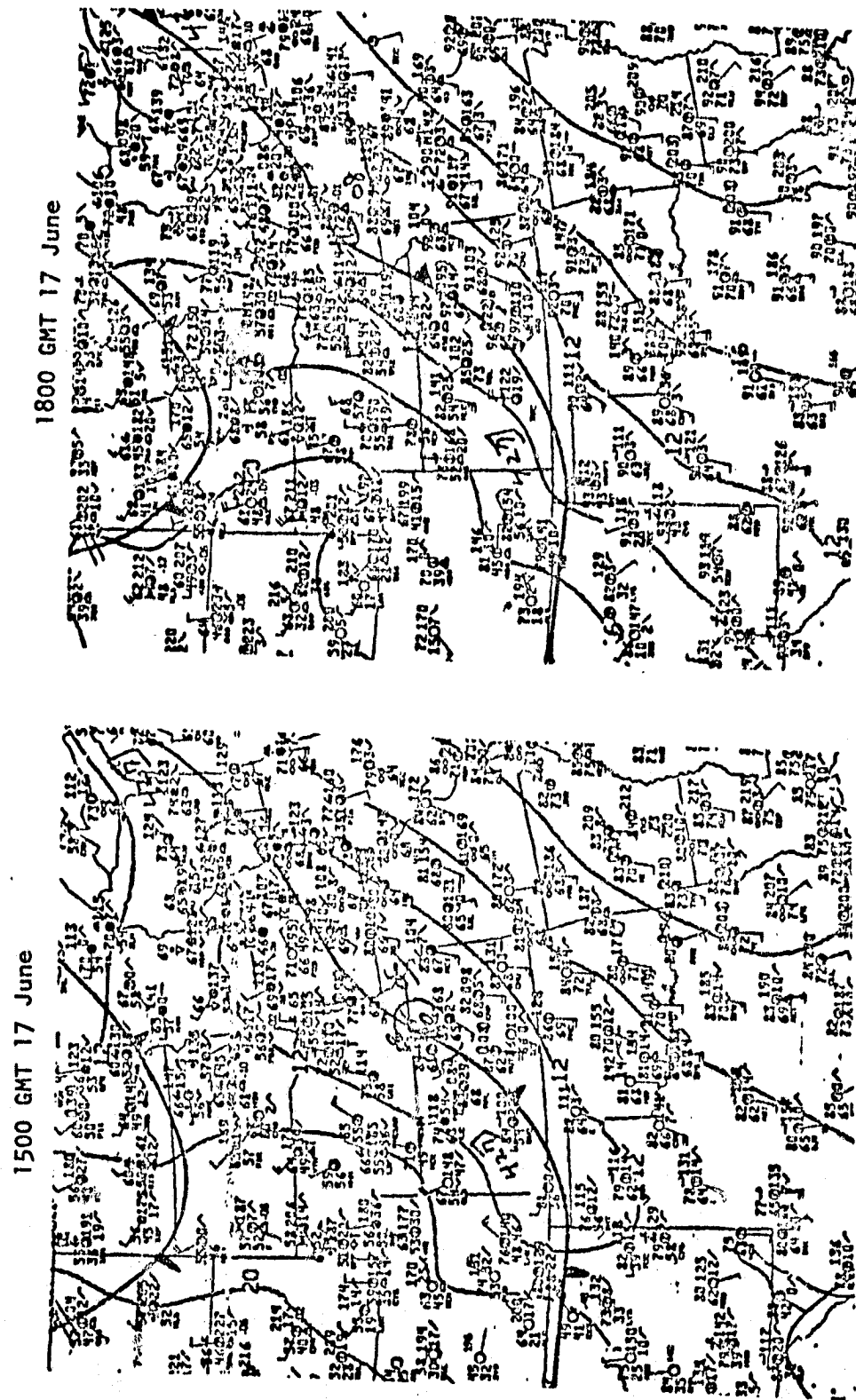


Figure 3-25a. Left: National Weather Service radar summary for 1535 GMT 17 June.
 Right: National Weather Service radar summary for 1735 GMT 17 June.



ORIGINAL PAGE IS
OF POOR QUALITY

Figure 3-26a. Left: National Weather Service surface weather map and sea level pressure analysis for 1500 GMT 17 June.
Right: National Weather Service surface weather map and sea level pressure analysis for 1800 GMT 17 June.

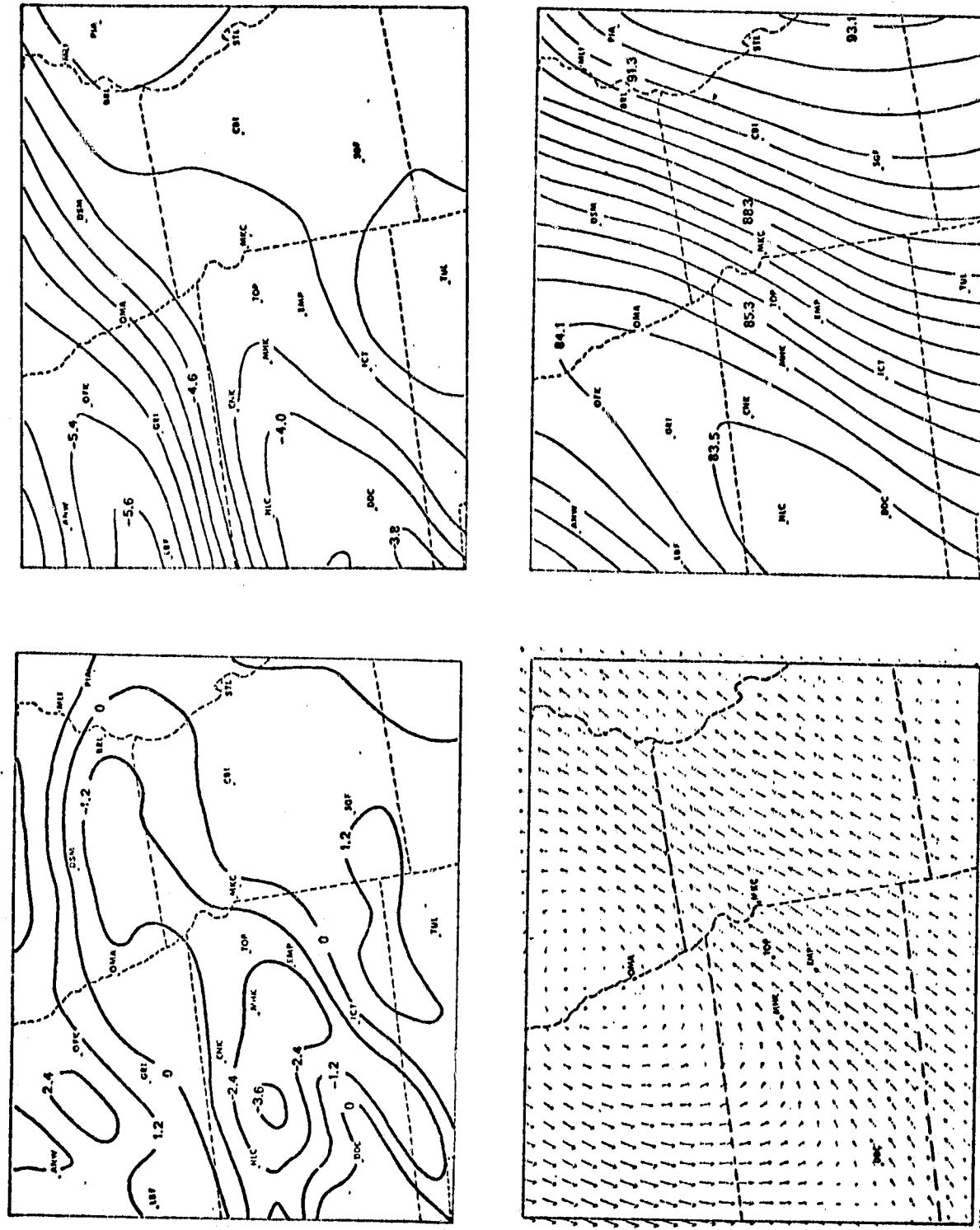


Figure 3-24b. Six hour 1150 m model forecast valid at 1800 GMT 17 June. Upper left: Divergence at $1.2 \times 10^{-5} \text{ s}^{-1}$ intervals. Upper right: σ_E at intervals of 0.2. Lower left: Wind vectors. Lower right: Pressure at 0.6 mb intervals with preceding 8 omitted in labels.

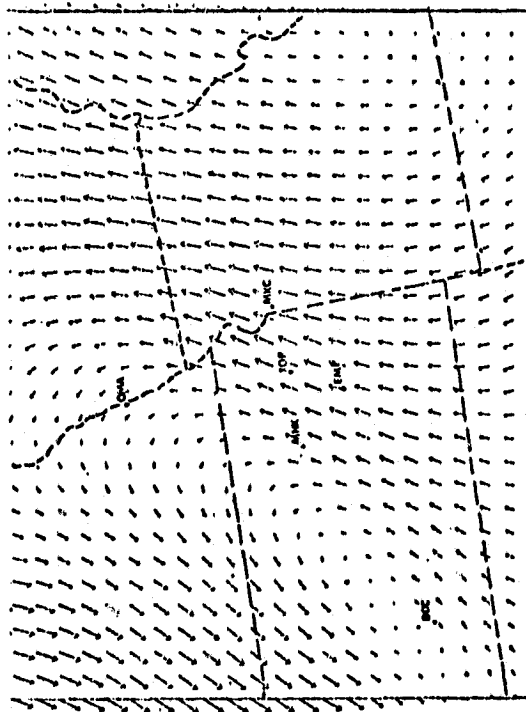
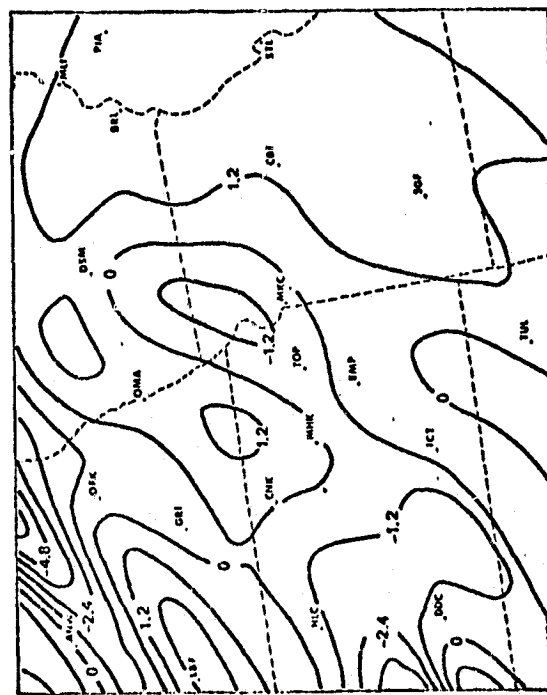
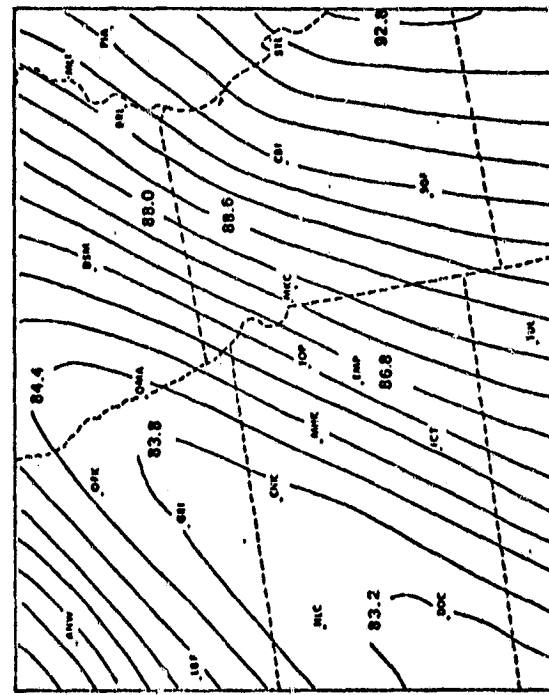
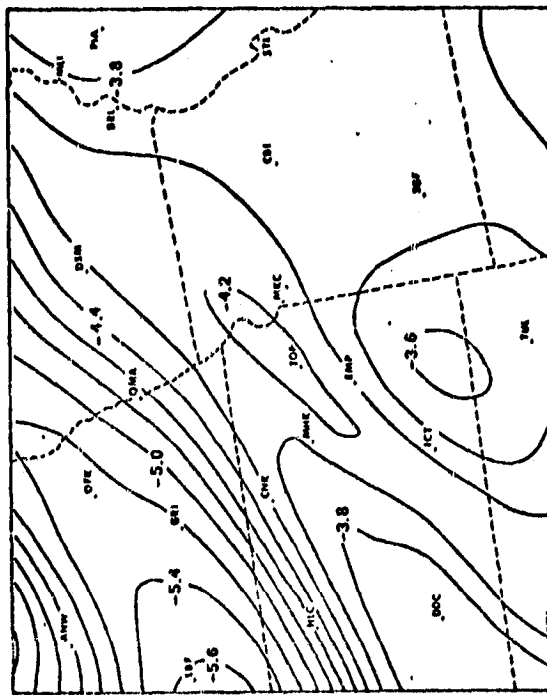


Figure 3-24c. Nine hour 1150 m model forecast valid at 2100 GMT 17 June. Upper left: Divergence at $1.2 \times 10^{-5} \text{ s}^{-1}$ intervals. Upper right: σ_E at intervals of 0.2. Lower left: Wind vectors. Lower right: Pressure at 0.6 mb intervals with preceding 8 omitted in labels.

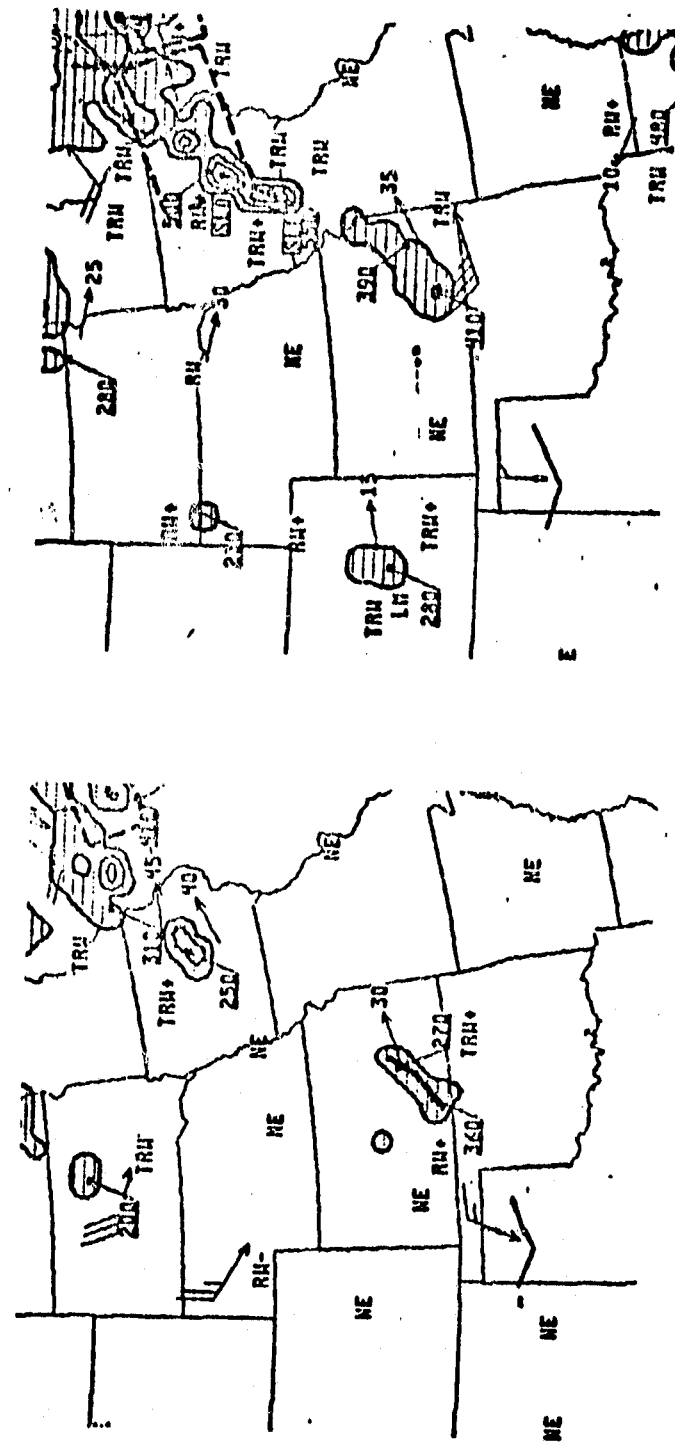


Figure 3-25b. Left: National Weather Service radar summary for 2035 GMT 17 June.
Right: National Weather Service radar summary for 2235 GMT 17 June.

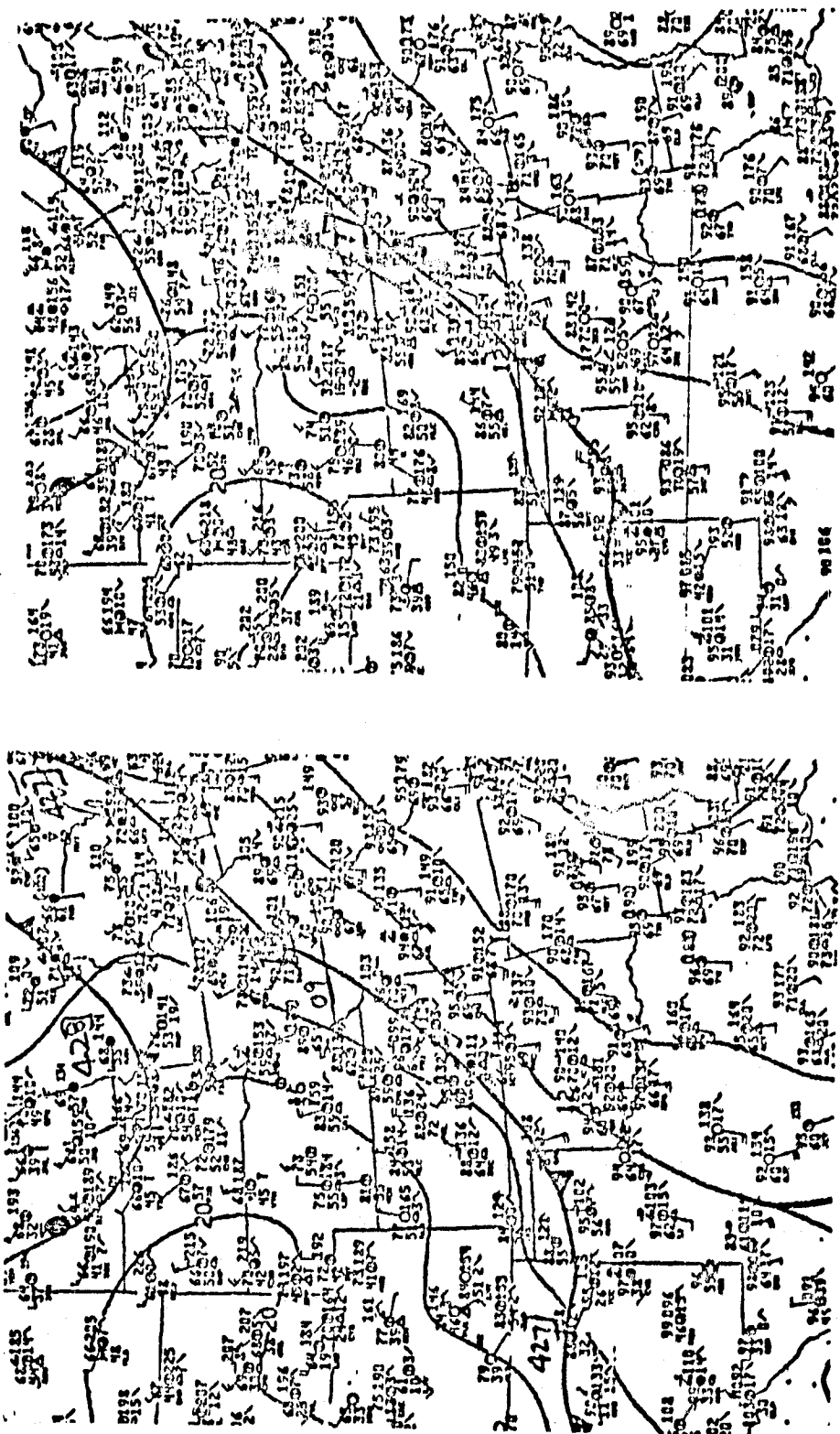


Figure 3-26b. Left: National Weather Service surface weather map and sea level pressure analysis for 2100 GMT 17 June.
 Right: National Weather Service surface weather map and sea level pressure analysis for 0000 GMT 17 June.

**ORIGINAL PAGE IS
OF POOR QUALITY**

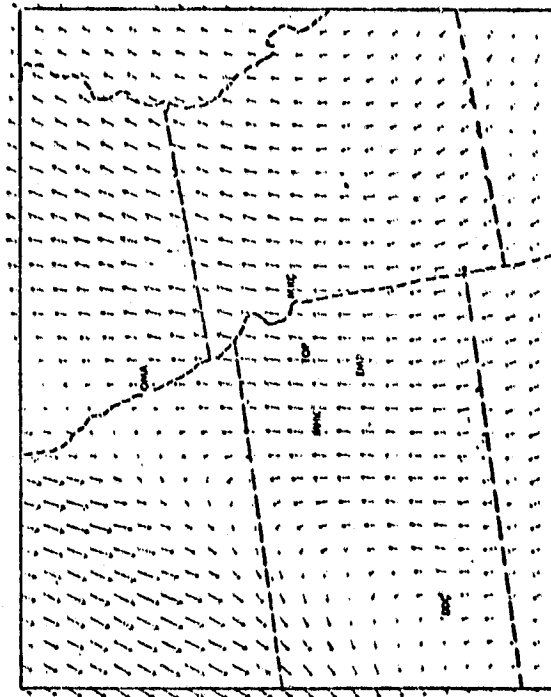
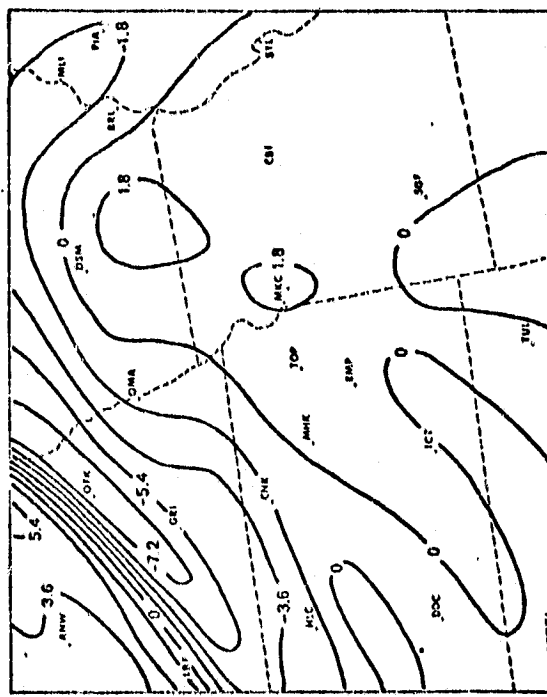
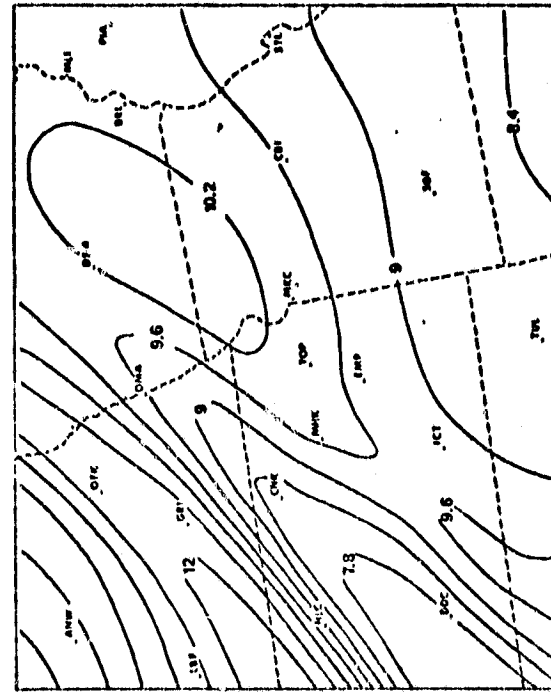
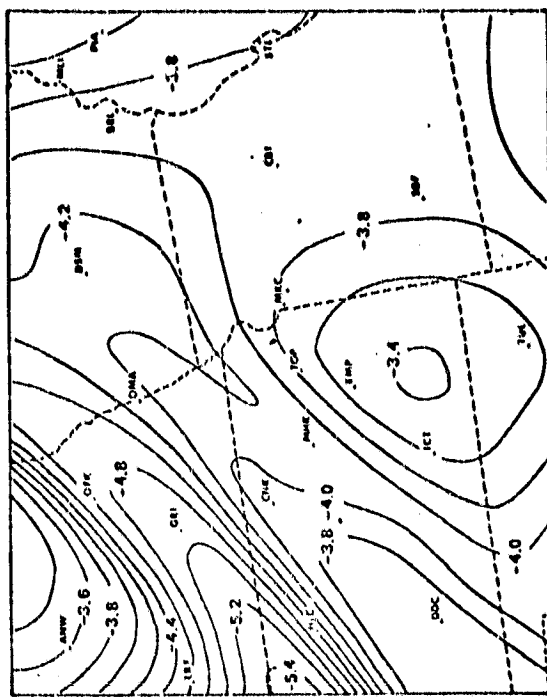


Figure 3-24d. Twelve hour 1150 m model forecast valid at 0000 GMT 18 June. Upper left: Divergence at intervals of $1.8 \times 10^{-5} \text{ s}^{-1}$. Upper right: σ_E at intervals of 0.2. Lower left: Mixing ratio at intervals of 0.6 g/kg.

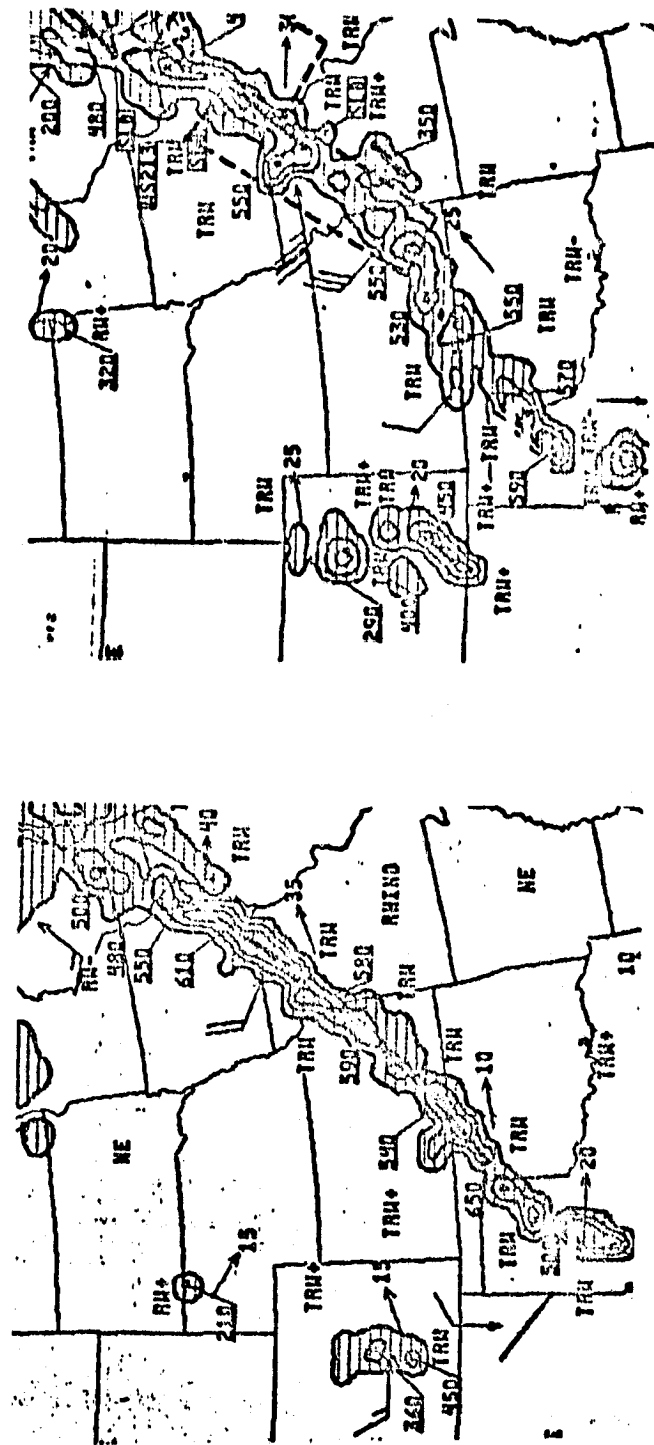


Figure 3-25c. Left: National Weather Service radar summary for 0035 GMT 18 June. Right: National Weather Service radar summary for 0235 GMT 18 June.

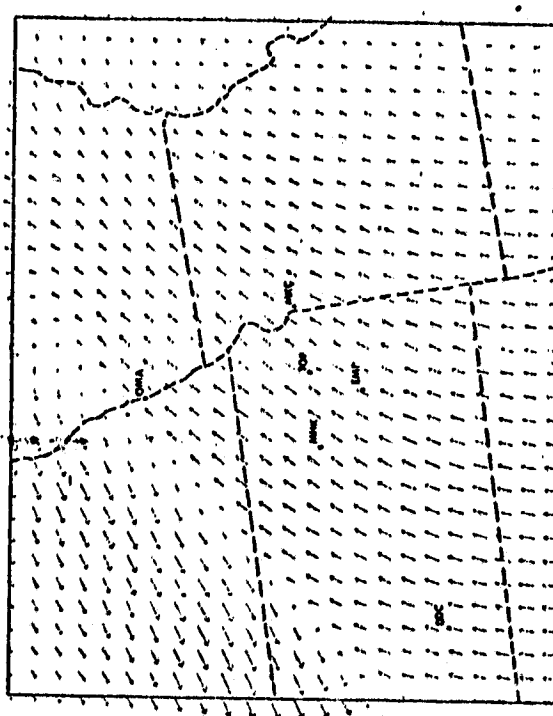
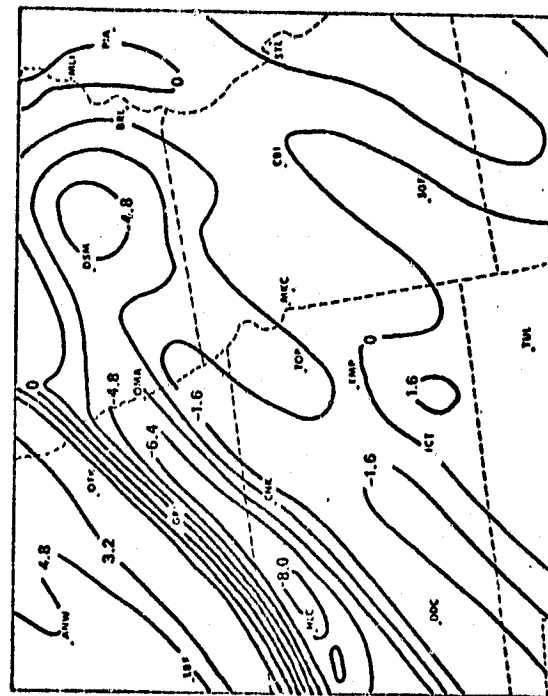
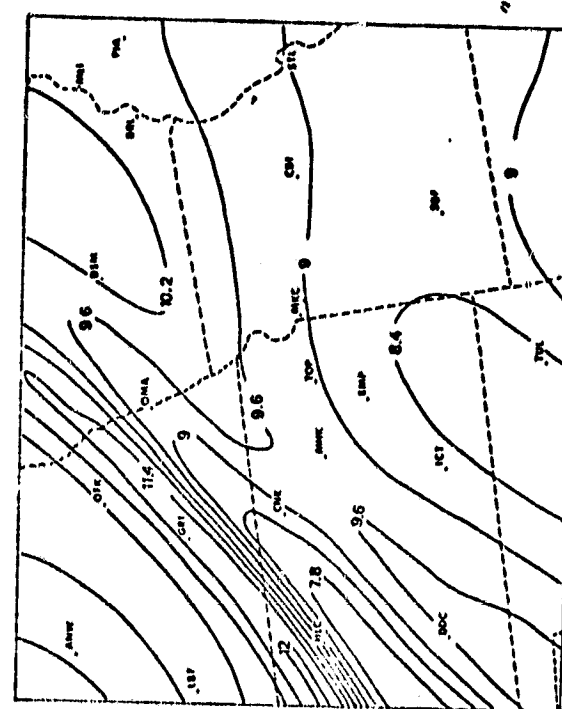
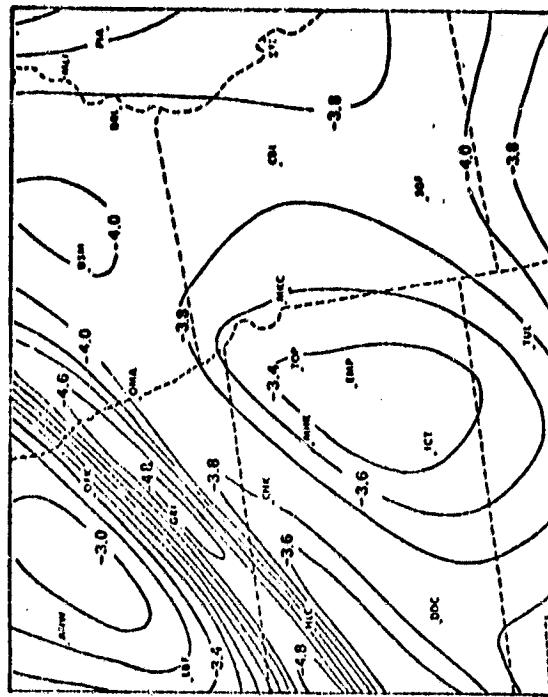


Figure 3-24e. Fifteen hour 1150 m model forecast valid at 0300 GMT 18 June. Upper left: Divergence at intervals of $1.6 \times 10^{-5} \text{ s}^{-1}$. Upper right: σ_E at intervals of 0.2. Lower left: Wind vectors. Lower right: Mixing ratio at intervals of 0.6 g/kg.

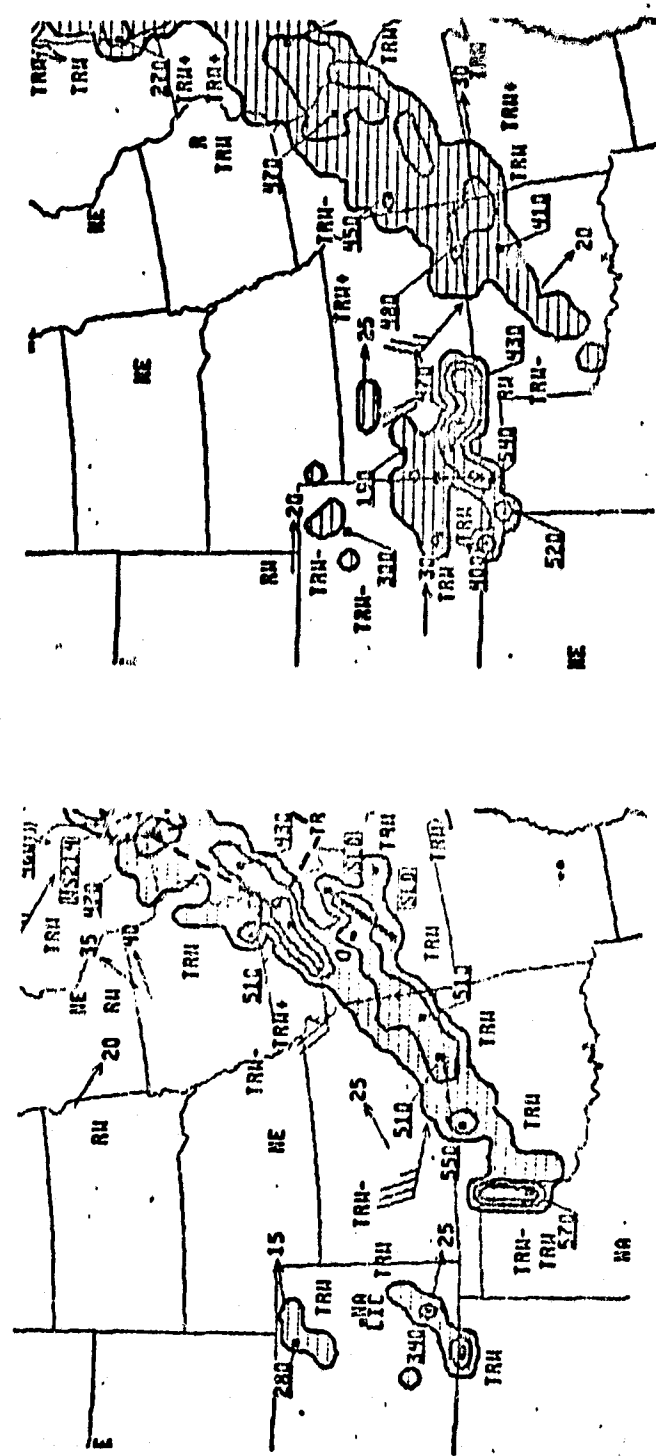


Figure 3-25d. Left: National Weather Service radar summary for 0335 GMT 18 June.
 Right: National Weather Service radar summary for 0635 GMT 18 June.

3.5 Case V: 12 May 1978

A widespread severe local weather outbreak occurred over the southeastern Plains, the middle and lower Mississippi Valley and parts of the southern Midwest on the afternoon and night of 12 May 1978. The area of most intense convective activity included eastern Oklahoma, northeastern Texas, most of Arkansas and parts of southern Missouri, western Tennessee and Mississippi. Numerous reports of tornadoes, funnel clouds, large hail and damaging winds were received from locations throughout this area.

The activity developed in conjunction with an impressive springtime cyclogenesis over the central Plains and Midwest. The surface weather map at 1200 GMT 12 May 1978 (Figure 3-27a) reveals a complex multi-centered low pressure system over the Great Plains and the Midwest. Warm and quite moist air was flowing northward on the eastern side of this system. Surface dew points over 60°F (15°C, 288°K) extended as far north as southern Missouri, while 70°F (21°C, 294°K) dew points were observed over eastern Texas and Missouri. The system possessed a double cold front structure at this time. The leading front was located from a low pressure center over northern Oklahoma southward to Mexico. This front separated the warm very moist maritime tropical air to the east from warm, but very much drier continental air to the west. A secondary cold front extended from another low-pressure center over eastern Nebraska west-southwestward to northern Arizona. This front divided the warm, dry air to the south from cold, relatively dry continental polar air to the north.

The 500 mb chart for 1200 GMT 12 May 1978 (Figure 3-27a) indicated strong cold advection into the trough associated with the Great Plains-Midwest low pressure system and strong warm advection over the Midwest. In addition, a significant amount of westerly momentum was being advected into the trough from an up-stream maximum of over 65 knots. Therefore, one might expect this synoptic system to undergo significant deepening over the next 24 hours.

The 1200 GMT 13 May 1978 surface and 500 mb chart (Figure 3-27 b) shows that this system has deepened considerably and moved slightly to the east. However, the cold front associated with this system has swept eastward into eastern Alabama, Georgia and eastern Tennessee. This represents a frontal boundary movement of over 1000 km in 24 hours. This rapid synoptic scale cyclogenesis and cold frontal movement would be expected to cause the 38 km limited domain model some difficulties in transporting features to the east with their proper speed.

The NMC 1000 mb, 850 mb and 700 mb height and dew point data for 1200 GMT 12 May 1978 is presented in Figure 3-28. In this case, the model was initialized with added vertical resolution at low levels. The vertical levels were 400, 750, 1150, 1675 and 2275 meters.

A time sequence of the model σ_E and divergence forecasts along with selected radar summaries compiled during the forecast period are presented in Figure 3-30.

By six hours after initialization (1800 GMT) an area of strong 400 m convergence is forecasted over extreme eastern

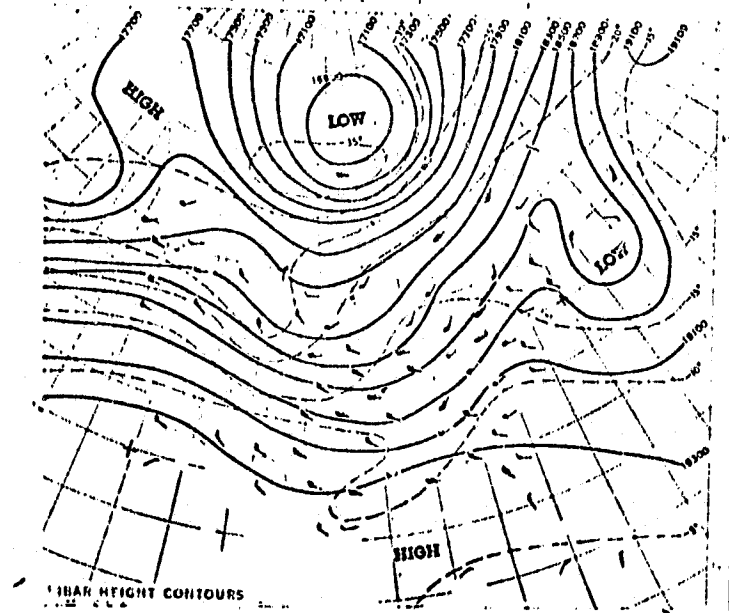
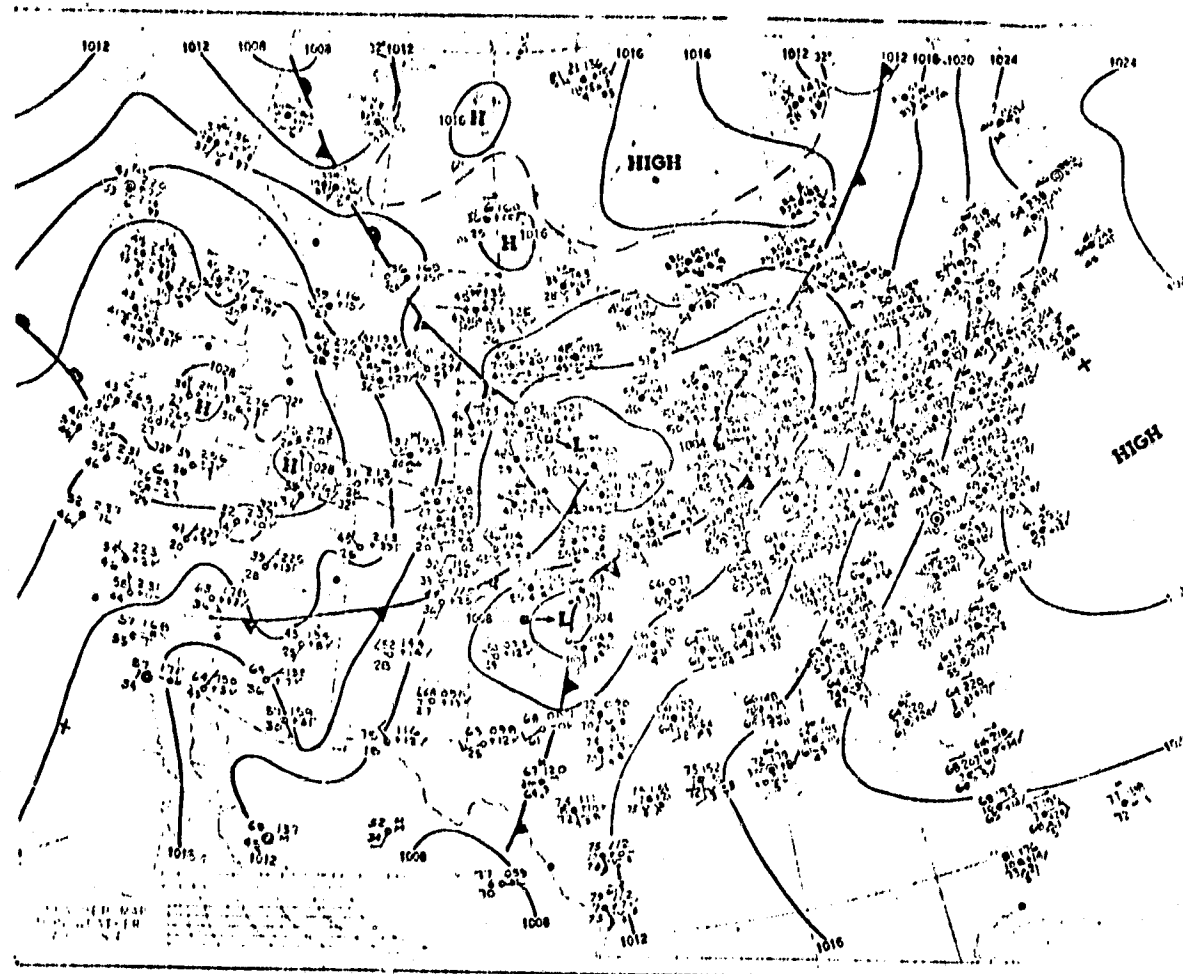
Oklahoma and extreme southeastern Kansas. Although this is superimposed upon a relatively high value of σ_E , a developing line of convective activity is reported over this area on the 1735 GMT radar summary.

By nine hours (2100 GMT) into the forecast, the σ_E minimum is beginning to organize into a band over western and central Arkansas. At this time, the model has forecasted the existence of two zones of convergence. One is over southeastern Oklahoma and western Arkansas, while a second zone is located in extreme southeastern Kansas. The 2035 GMT radar summary clearly indicates this type of structure in the distribution of convective activity. The convergence area over western Arkansas and eastern Oklahoma is superimposed upon lower σ_E values and would be expected to be the area of more intense convection. The 2035 GMT radar reveals that the southeastern line is, indeed, the more intense with several radar determined cell tops over 40,000 feet.

After nine hours, the model forecast is degraded by the effects of the synoptic scale system which are not resolved by the model. A convergence area does propagate through Arkansas into Mississippi during the next twelve hours. In doing so, it traverses a zone of very low σ_E values, (<-6.0) implying that the convective activity over Arkansas and western Mississippi should be rather intense. The observed convective activity did, indeed, propagate eastward through this region. However, the timing was a few hours ahead of the model timing of the activity.

In summary, the 12 May 1978 case illustrates another example of widespread convective activity in association with a significant synoptic scale cyclogenesis. The model forecast appeared to

simulate the space, time and amplitude characteristic of the observed mesoscale zones of convective activity very well through the first nine hours of the forecast. Afterwards, the effect of the synoptic scale amplification and translation caused the model fields to lag behind the observed convective activity.



ORIGINAL PAGE IS
OF POOR QUALITY

Figure 3-27a. Top: Surface weather map for 1200 GMT 12 May 1978.
 Bottom: 500 mb chart for 1200 GMT 12 May 1978.
 Heights are labeled in feet.

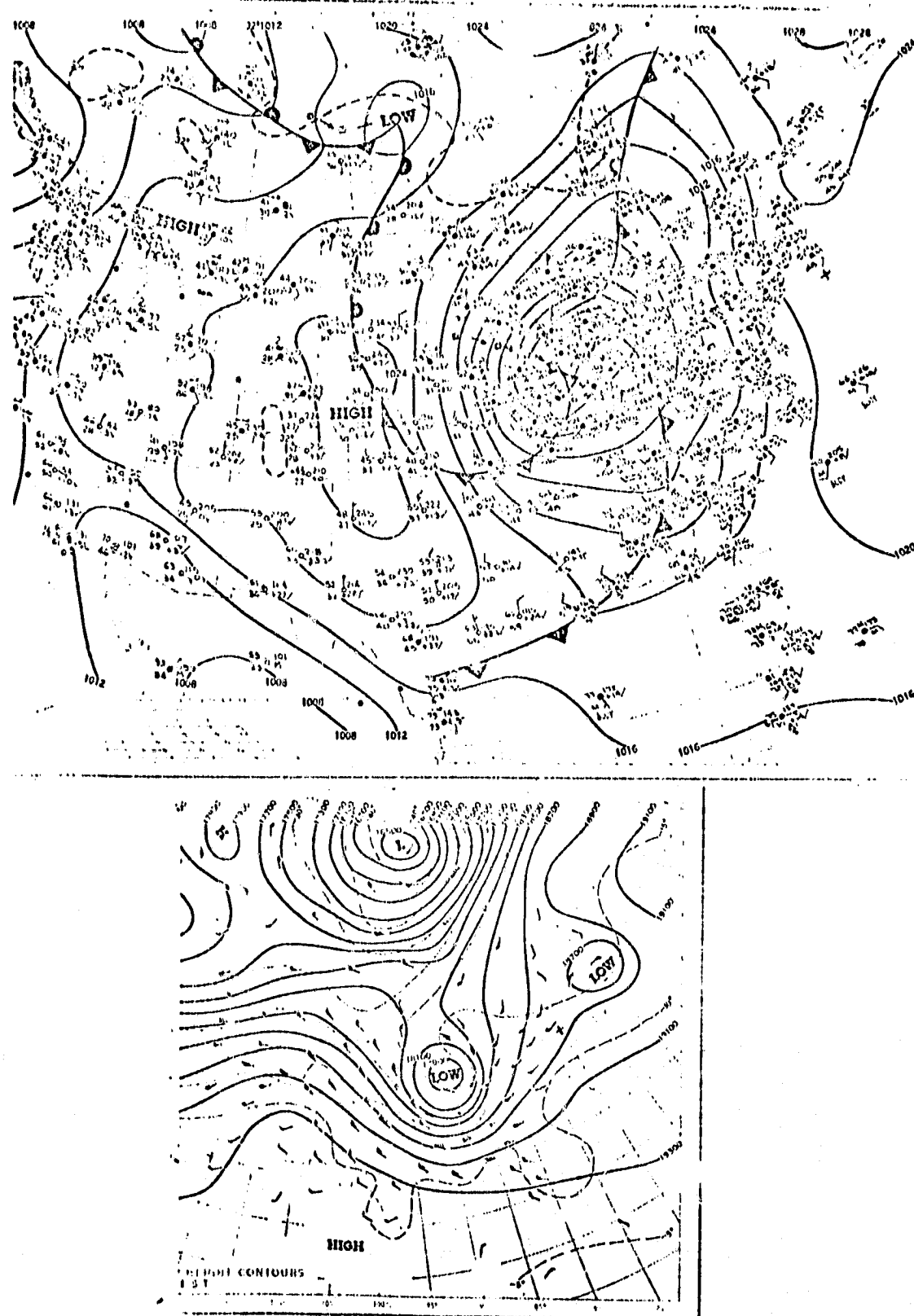


Figure 3-27b. Top: Surface weather map for 1200 GMT 13 May 1978.
Bottom: 500 mb chart for 1200 GMT 13 May 1978.
Heights are labeled in feet.

Figure 3-28a. NMC 1000 mb height and dew point data for 1200 GMT 12 May 1978. Bold lines are heights in decameters. Light lines are dew points in °K.

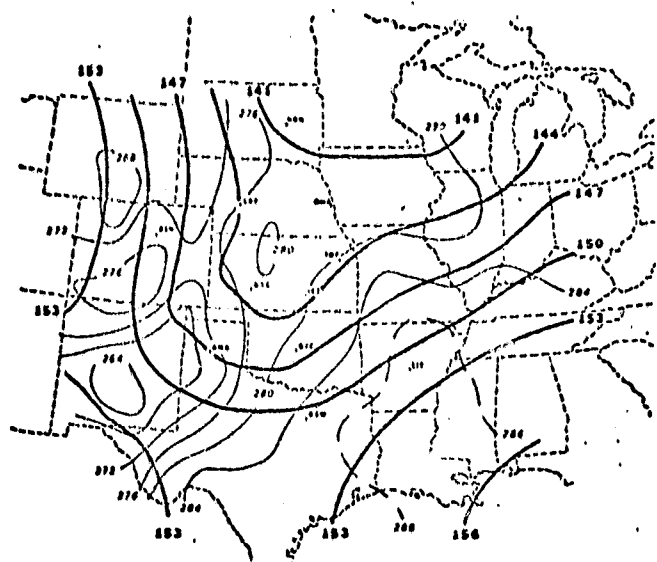
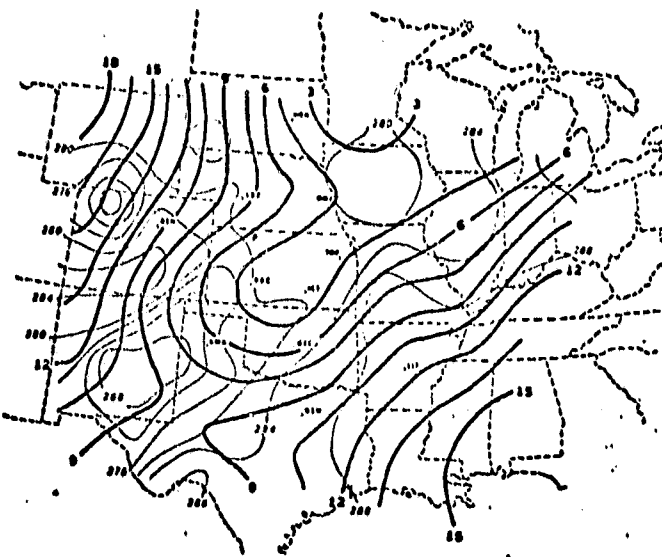
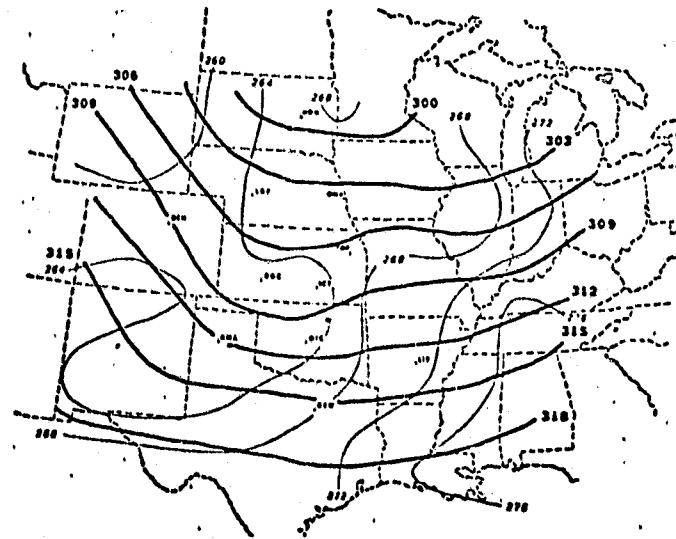


Figure 3-28b. NMC 850 mb height and dew point data for 1200 GMT 12 May 1978. Bold lines are heights in decameters. Light lines are dew points in °K.

Figure 3-28c. NMC 700 mb height and dew point data for 1200 GMT 12 May 1978. Bold lines are heights in decameters. Light lines are dew points in °K.



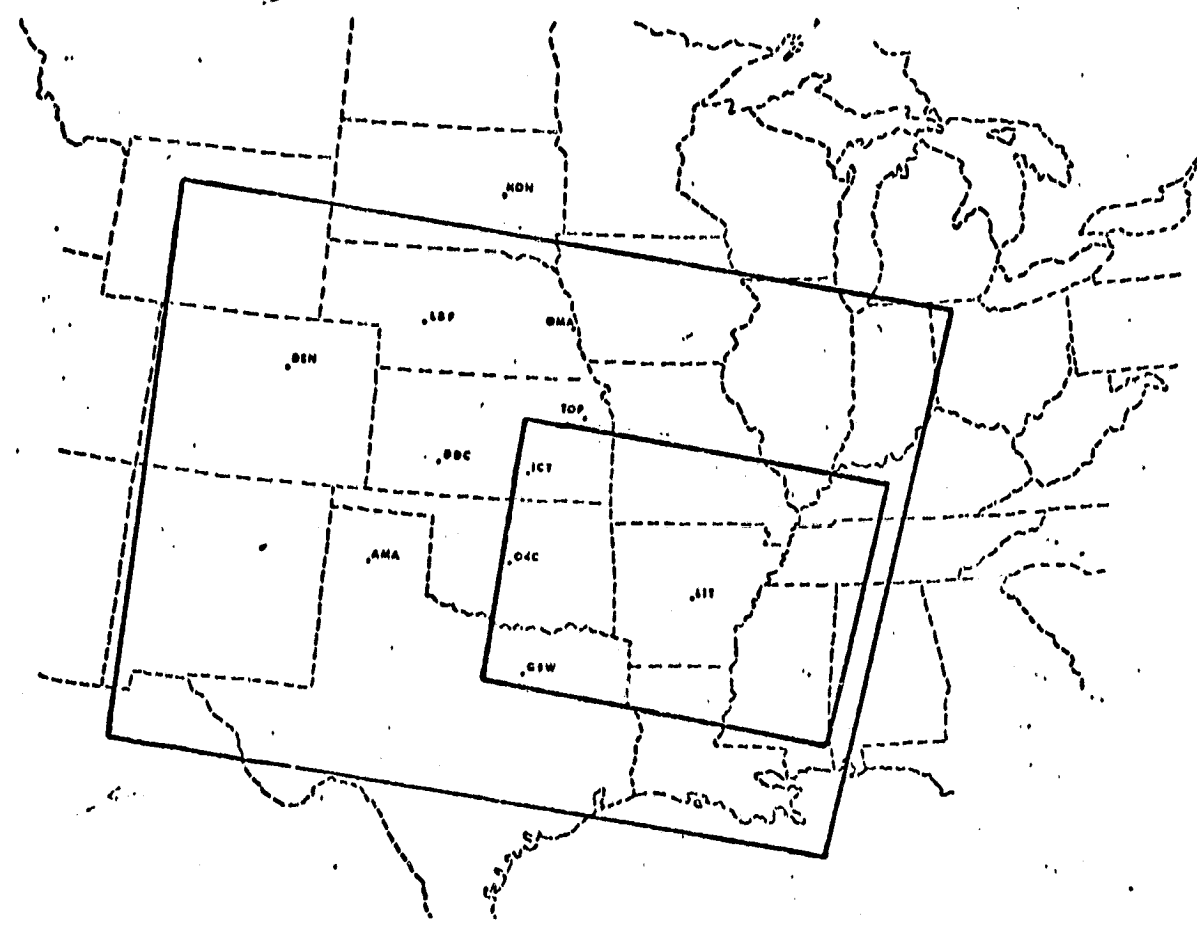


Figure 3-29. The 38 km model domain and display area for the 12 May 1978 case. The outer box demarcates the model domain. The inner box indicates the display area.

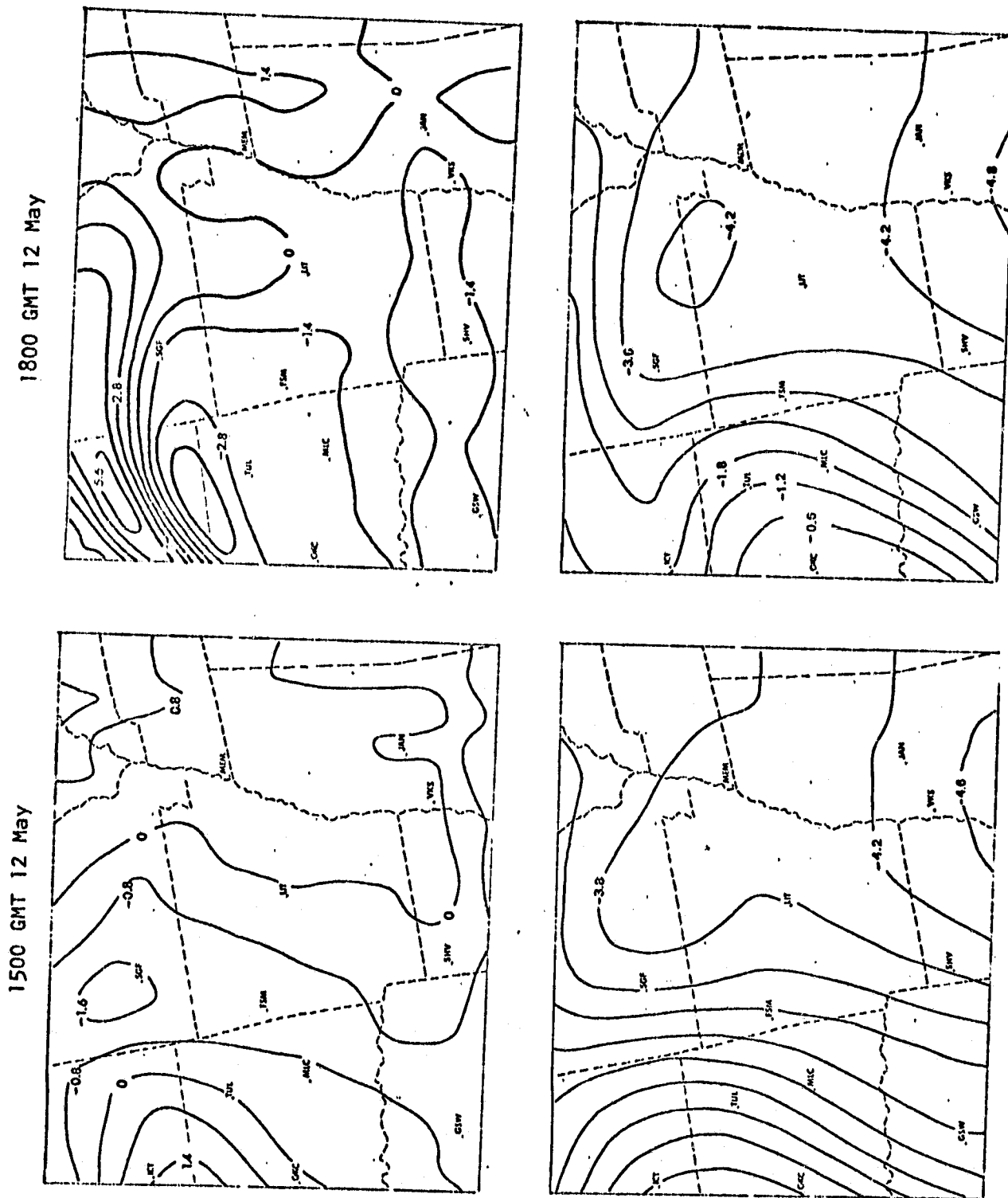


Figure 3-30a. Upper left: three hour forecast of 400 m divergence with isopleths at intervals of $0.8 \times 10^{-5} \text{ s}^{-1}$. Lower left: 750 m σ_E at intervals of 0.4. Upper right: Six hour model forecast of 400 m divergence with isopleths of intervals of $1.4 \times 10^{-5} \text{ s}^{-1}$. Lower right: 750 m σ_E at intervals of 0.6.

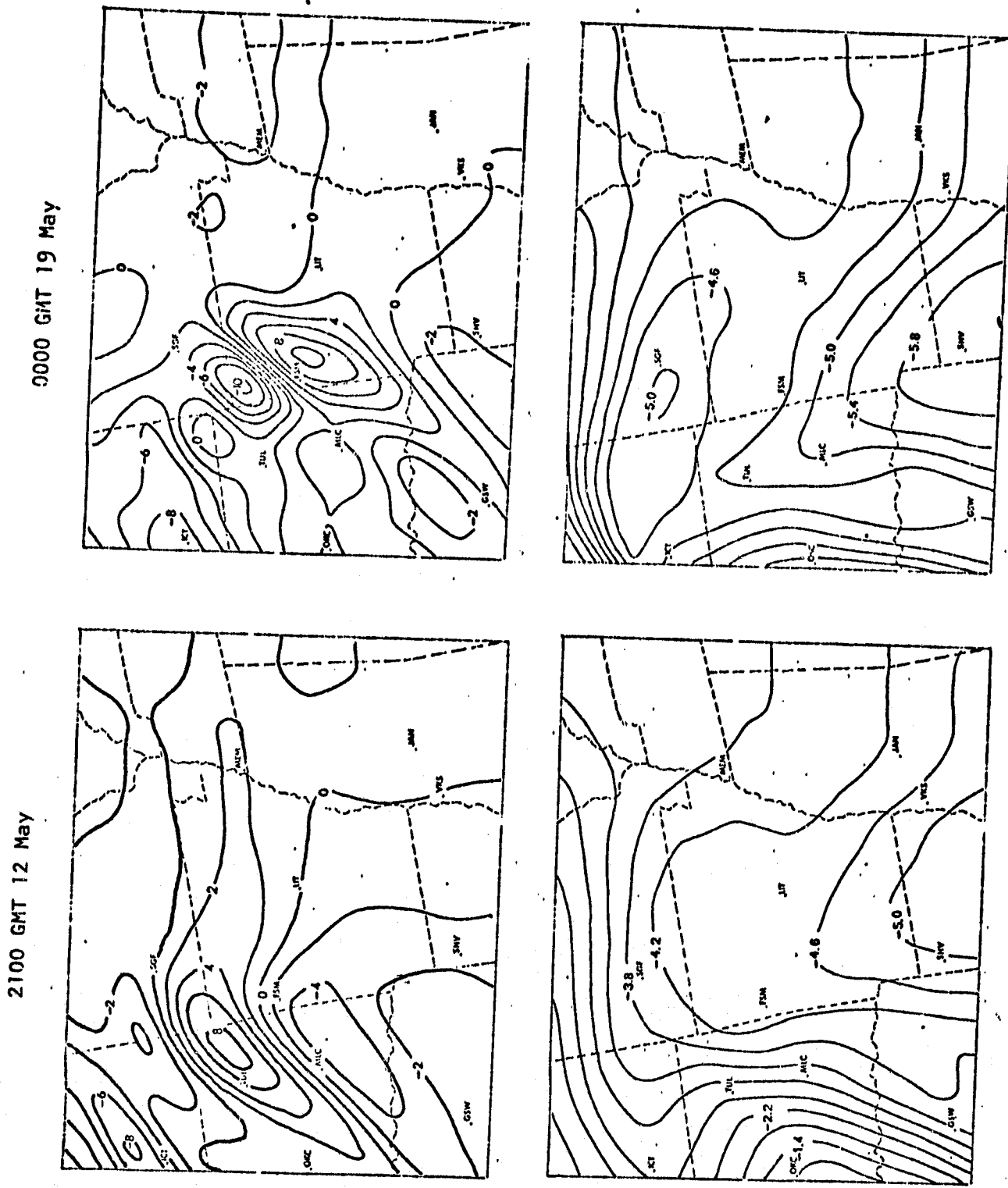


Figure 3-30b. Upper left: Nine hour model forecast of 400 m divergence with isopleths at intervals of $2 \times 10^{-5} \text{ s}^{-1}$. Lower left: 750 m σ_E at intervals of 0.4. Upper right: Twelve hour model forecast of 400 m divergence with isopleths at intervals of 0.6. Lower right: 750 m σ_E at intervals of 0.6.

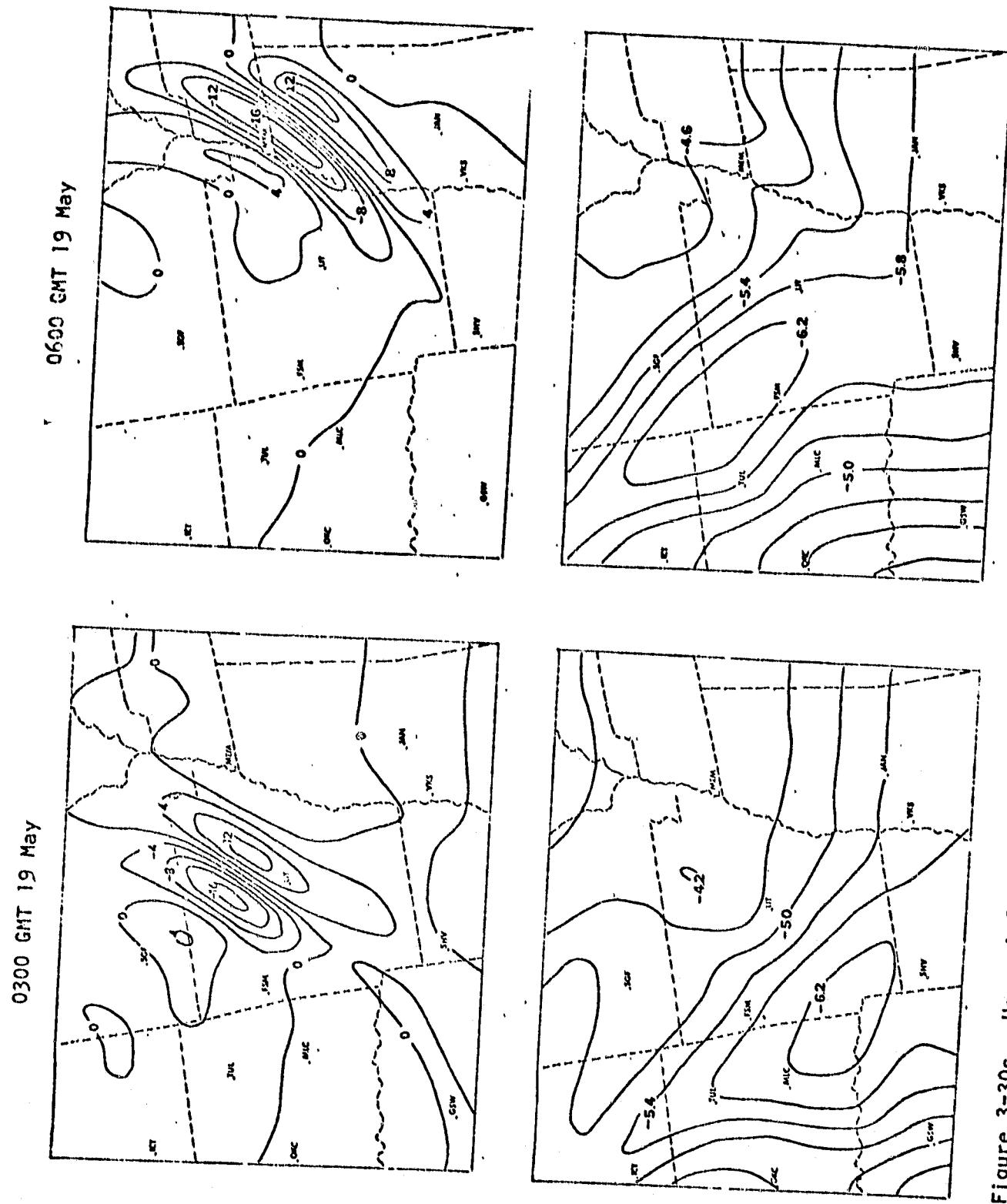


Figure 3-30c. Upper left: Fifteen hour model forecast of the 400 m divergence with isolopleths at intervals of $4 \times 10^{-5} \text{ s}^{-1}$. Lower left: 750 m σ_E at intervals of 0.4. Upper right: Eighteen hour model forecast of 400 m divergence with isolopleths at intervals of $1.4 \times 10^{-5} \text{ s}^{-1}$. Lower right: 750 m σ_E at intervals of 0.6.

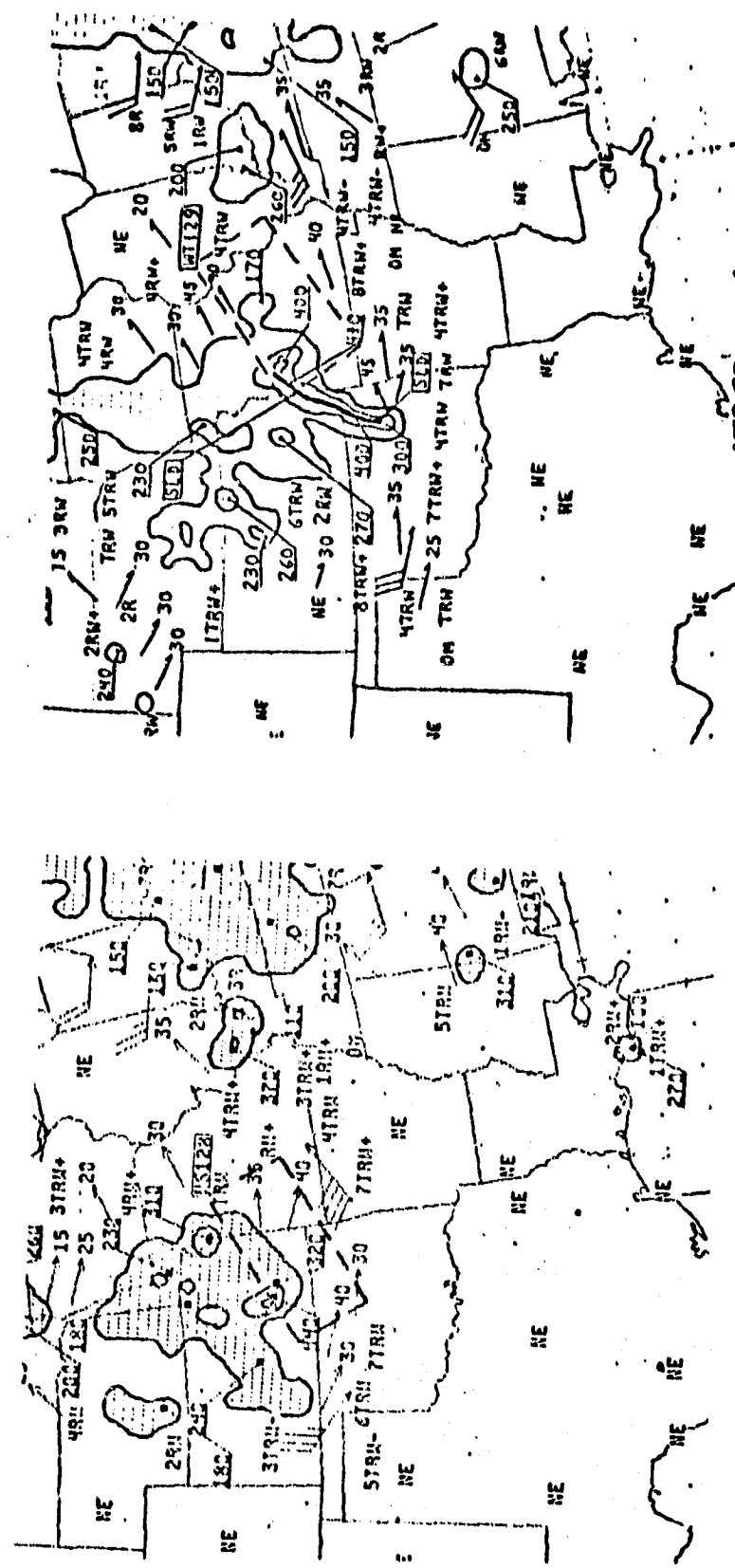


Figure 3-30d. Left: National Weather Service radar summary for 1435 GMT 12 May. Right: National Weather Service radar summary for 1735 GMT 12 May.

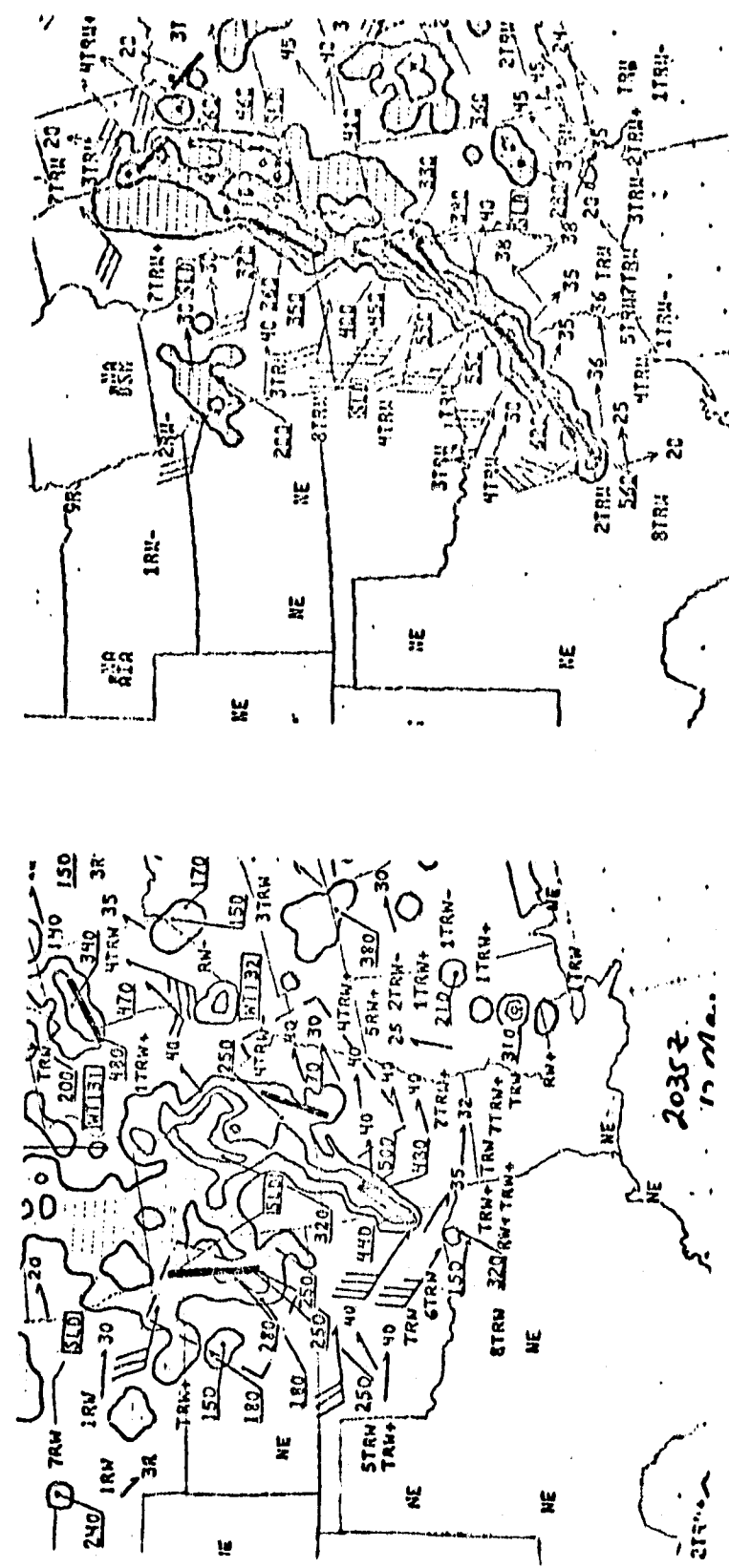


Figure 3-30e. Left: National Weather Service radar summary for 2035 GMT 12 May. Right: National Weather Service radar summary for 0035 GMT 13 May.

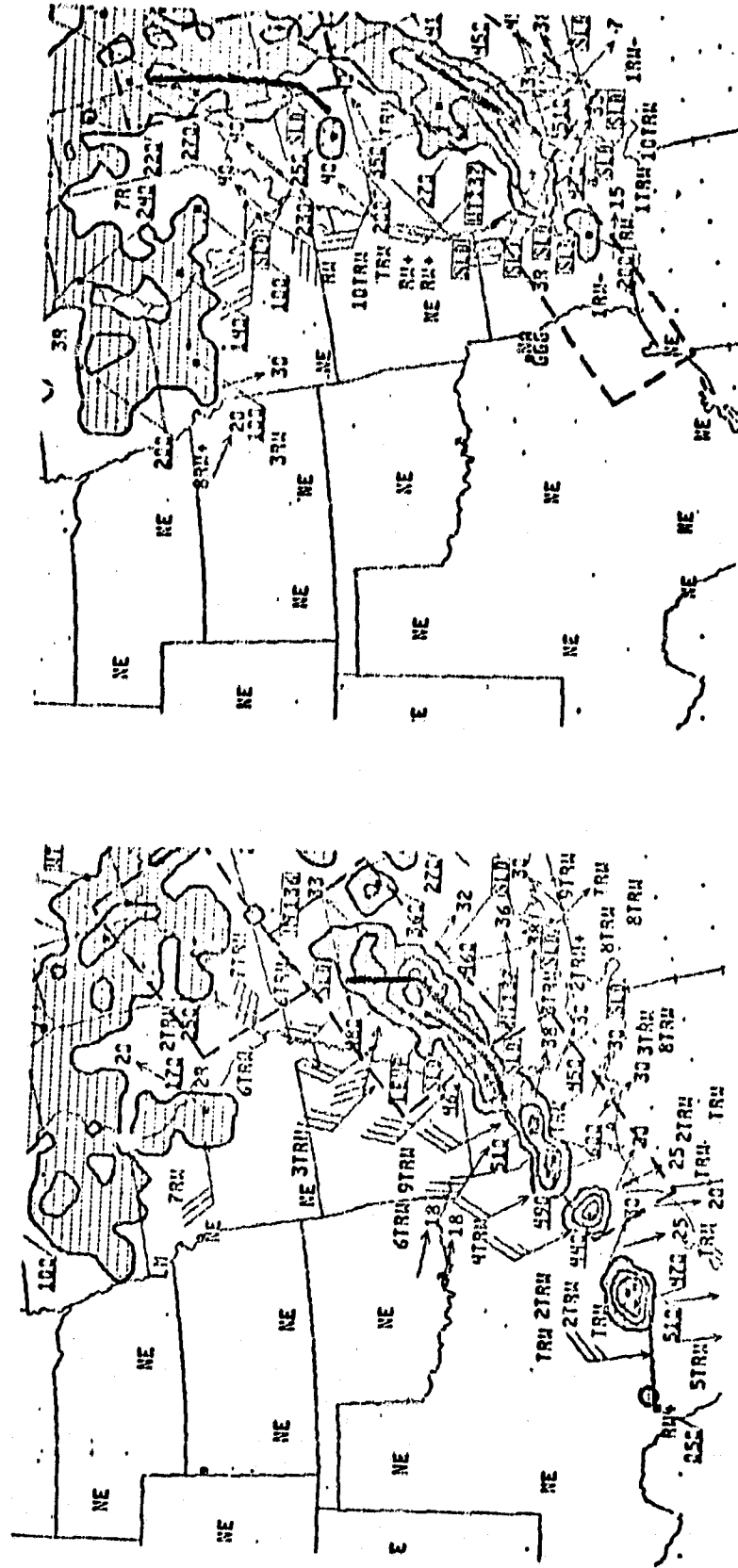


Figure 3-30f. Left: National Weather Service radar summary for 0335 GMT 13 May.
Right: National Weather Service radar summary for 0635 GMT 13 May.

**ORIGINAL PAGE IS
OF POOR QUALITY**

3.6 Case VI: 18 May 1978

Severe weather erupted over southwestern Oklahoma and northwestern Texas during the late afternoon and evening of 18 May 1978. Figure 3-31 is a display of the areal extent of the reported severe weather. At approximately 6:00 pm CST (0000 GMT, 19 May 1978) Post, Texas reported 3/4 inch hail. During the next two hours (0000 to 0200 GMT) a twelve mile swath from southwest of Grassland, Texas to near Post, Texas received hail up to 1 3/4 inches in diameter and nearly 2.5 inches of rain. In addition, at approximately 6:30 pm CST (0030 GMT) Hollis, Oklahoma reported hail as large as 2 3/4 inches in diameter.

Later in the night, the severest convective activity shifted slightly to the southwest. At 1:24 am CST 19 May (0724 GMT) Slaton, Texas in Lubbock County reported extensive damage to homes and crops from hailstones up to 1 3/4 inches in diameter.

The 1200 GMT 18 May 1978 surface weather map (Figure 3-32a) reveals a familiar pattern on the central and western Plains. A north-south trough extends from eastern Montana southward to western Texas. A cold front is placed along the trough axis over the Oklahoma panhandle eastward to Georgia. Warm, very moist air is found to the east of the cold front and south of the stationary front. Surface dew points near 75°F (24°C, 297°K) were observed over southeastern Texas with 70°F (21°C, 294°K) dew points extending as far north as Dallas, Texas. Meanwhile, to the west of the cold front, surface dew points were mostly below 30°F (-1°C, 272°K) over extreme western Texas, New Mexico and Colorado.

The 1200 GMT 18 May 1978 500 mb chart (Figure 3-32a) reveals the presence of an ω block pattern over the United States. A difluent pattern in the wind and height fields is present over the central and southern Plains.

The 1200 GMT surface and 500 mb charts for 19 May 1978 (Figures 3-32 b) indicate that there was little change in the overall synoptic weather pattern over the central and southern Plains during the 24 hours following 1200 GMT 18 May. The previously described cases indicate that the 38 km limited domain model appears to do very well in these cases.

The NMC 1000 mb, 850 and 700 mb initial height and dew point data are displayed in Figure 3-33. In this case, the model was again initialized with added low level resolution. The vertical levels were 400, 750, 1150, 1675 and 2275 meters.

A very impressive forecast is revealed by comparing the 750 m σ_E and 400 m divergence fields with the radar summaries presented in Figure 3-35.

By 10 hours into the forecast (2200 GMT) the model has organized a zone of convergence from central Kansas southwestward through west central Oklahoma into west central Texas. A moderately strong convergence maximum ($-4 \times 10^{-5} \text{ s}^{-1}$) is located over central Kansas at this time. The forecasted σ_E distribution also has an axis of moderately low values from central Kansas southward to north central Texas.

Over the next two hours (2200 GMT to 0000 GMT, 19 May) the area of maximum convergence is forecasted to move to the south-southwest and increase in magnitude to $-5.6 \times 10^{-5} \text{ s}^{-1}$. The minimum σ_E axis is also forecasted to increase in strength and shift

slightly to the west during this two hour period. Thus, by 12 hours (0000 GMT) the maximum 400 m convergence and the minimum 750 m σ_E are nearly superimposed over southwestern Oklahoma. It was at about this time that the first reports of severe weather were received from Hollis, Oklahoma and Post, Texas.

During the next two hours (0000 GMT to 0200 GMT) the model forecasts a southwestward movement and growth of the convergence band. The area of maximum convergence has moved into the vicinity of Childress, Texas (CDS) and Hobart, Oklahoma (HBR). The magnitude had reached nearly -10^{-4} s^{-1} . The minimum values of σ_E have again decreased in response to the low level moisture convergence associated with the zone of wind velocity convergence. The 0135 GMT radar summary showed a southwest to northeast squall line which is nearly coincident with the model's band of superposition of strong low level convergence and minimum σ_E values. In fact, the area of maximum convergence between 13 and 14 hours of the model forecast is also the location of the most intense radar observed convective activity. For example, the highest radar reported echo (62,000 ft) is located just to the southeast (toward lower σ_E) of the model forecasted convergence maximum.

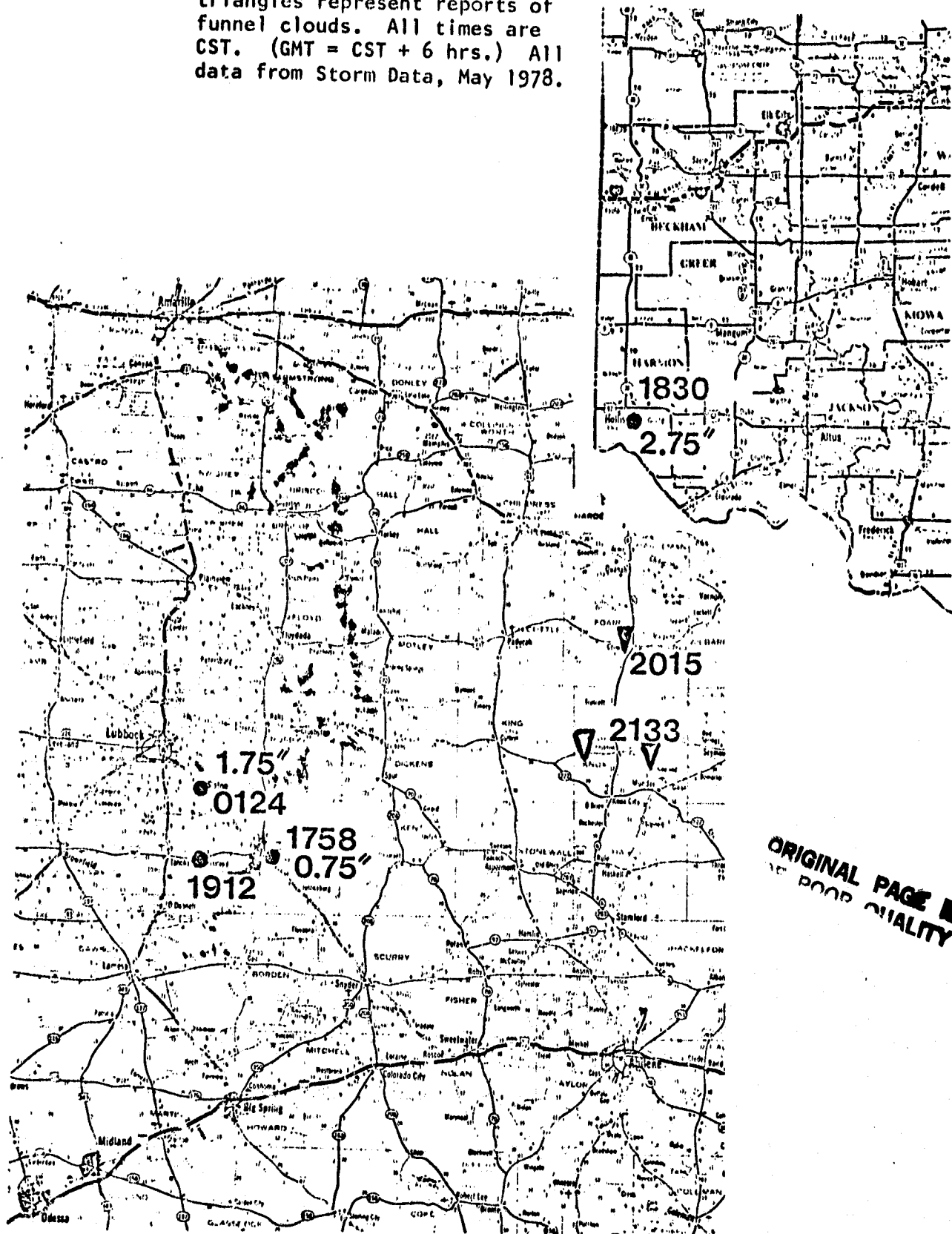
By 16 hours (0400 GMT) the model forecasted convergence maximum has moved southwestward into the vicinity of Lubbock, Texas (LBB). During the two hours from 0200 GMT (14 hours) to 0400 GMT (16 hours) the low level moisture convergence has continued to force a decrease in the 750 m σ_E values over southwestern Oklahoma and extreme north central Texas. One should note that by the 16 hour mark, a portion of the western flank of the convergence band has become superimposed upon high values of σ_E (>-1.0).

Thus, one would expect the majority of the convective activity to occur on the northeastern side of the convergence band. Indeed, this is observed on the late evening radar summaries.

The 10 to 17 hour convergence forecasts have clearly indicated a southwestward movement in the preferred zone of convective development. Interestingly, the same trend is observed in the real world. The convective activity in southwestern Oklahoma diminishes during the night while the activity in northwestern Texas continues through 1035 GMT.

In summary, the 18 May case featured a very slowly changing synoptic circulation. As a result, the temporal and spatial evolution of the model's stability and divergence fields was very closely aligned with the temporal and spatial evolution of the convective activity for over 18 hours.

Figure 3-31. An areal summary of the severe reports during the evening of 18 May. Darkened circles represent hail reports. Hailstone diameters are indicated in inches. Darkened inverted triangles designate tornado reports while undarkened inverted triangles represent reports of funnel clouds. All times are CST. (GMT = CST + 6 hrs.) All data from Storm Data, May 1978.



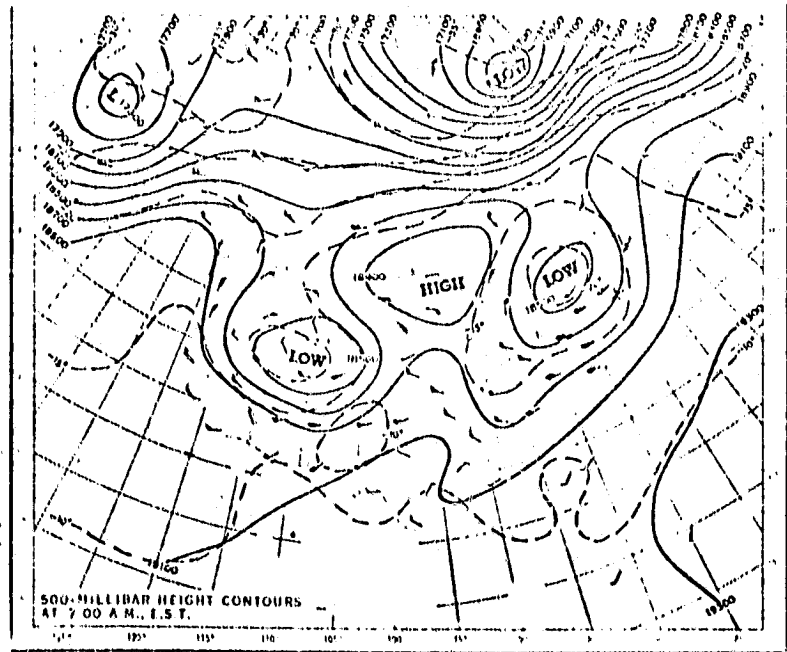
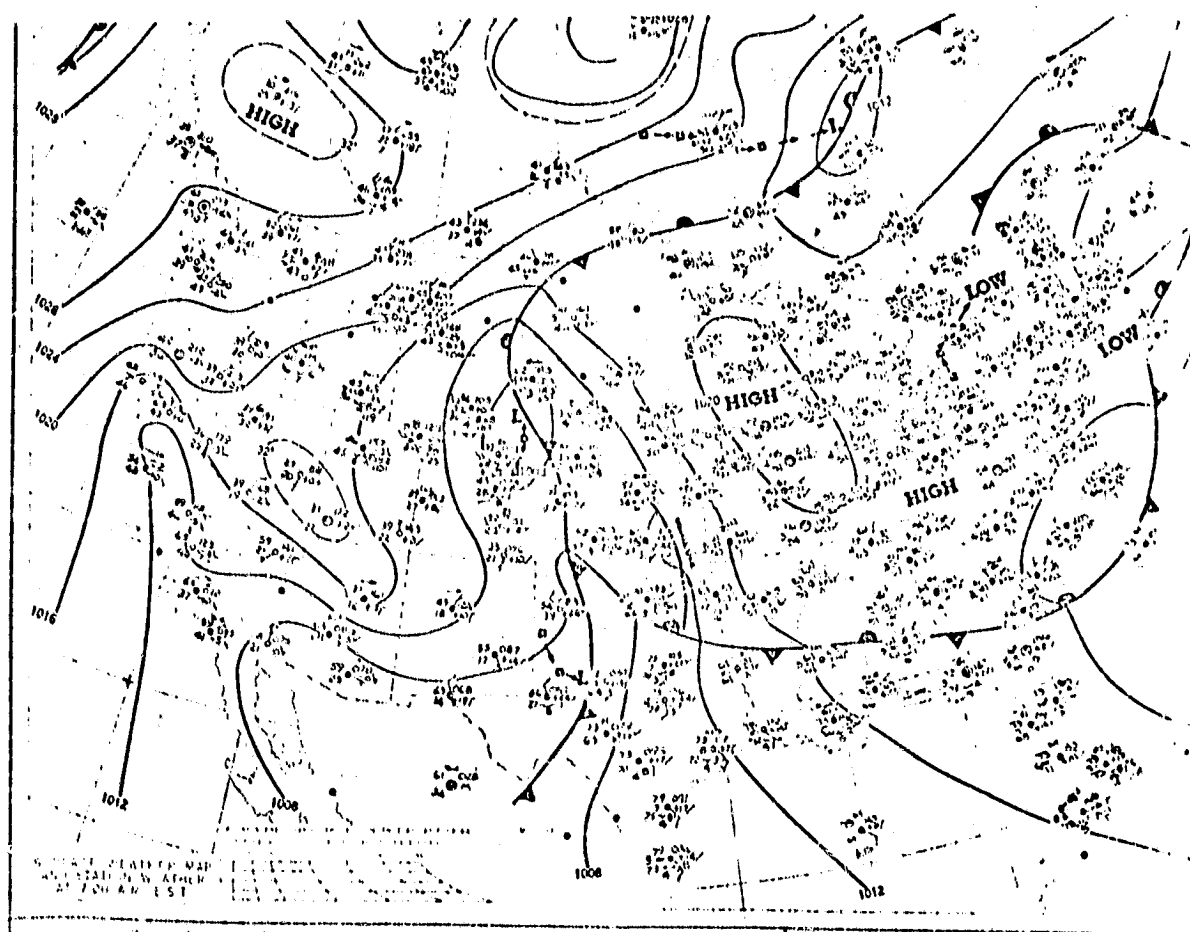


Figure 3-32a. Top: Surface weather map for 1200 GMT 18 May 1978.
Bottom: 500 mb chart for 1200 GMT 18 May 1978.
Heights are labeled in feet.

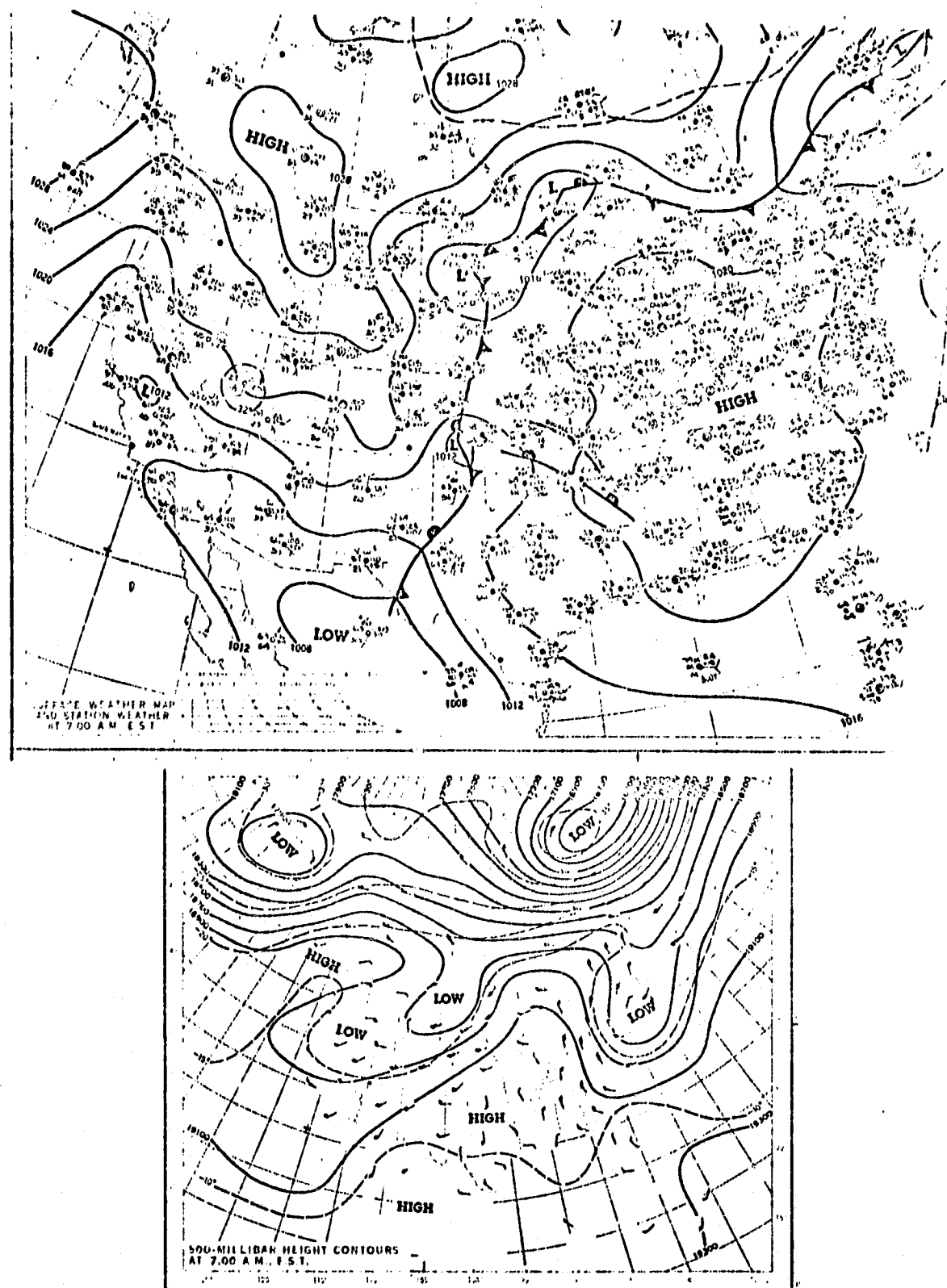


Figure 3-32b. Top: Surface weather map for 1200 GMT 19 May 1978.
 Bottom: 500 mb chart for 1200 GMT 19 May 1978.
 Heights are labeled in feet.

Figure 3-33a. NMC 1000 mb height and dew point data for 1200 GMT 18 May 1978. Bold lines are heights in decameters. Light lines are dew points in °K.

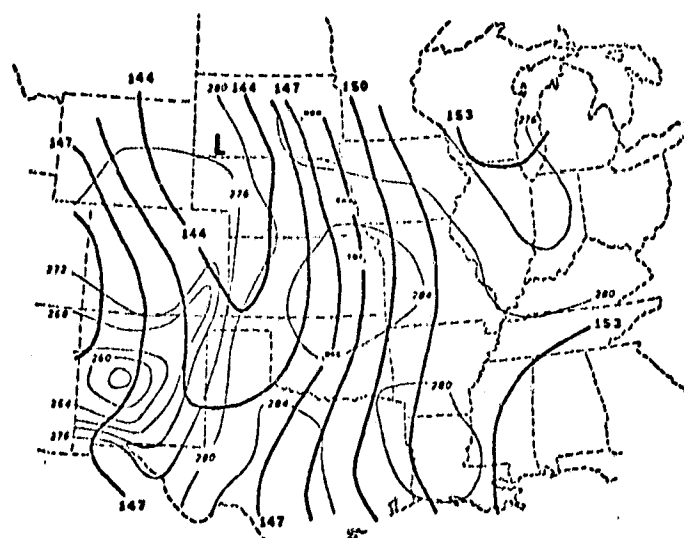
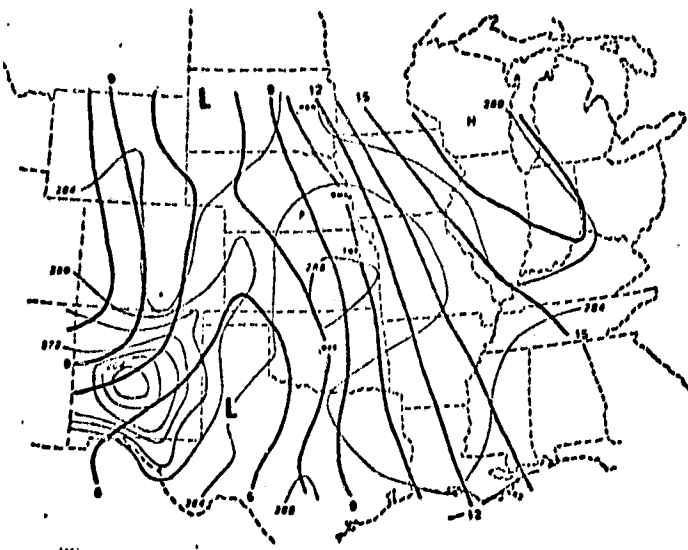
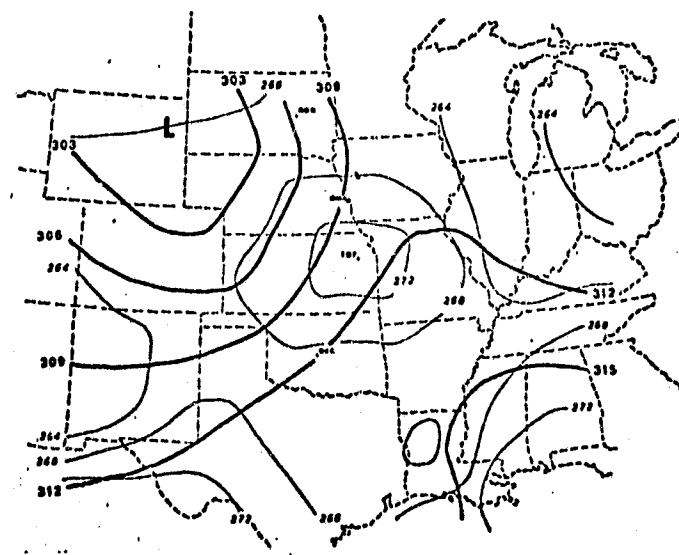


Figure 3-33b. NMC 850 mb height and dew point data for 1200 GMT 18 May 1978. Bold lines are heights in decameters. Light lines are dew points in °K.

Figure 3-33c. NMC 700 mb height and dew point data for 1200 GMT 18 May 1978. Bold lines are heights in decameters. Light lines are dew points in °K.



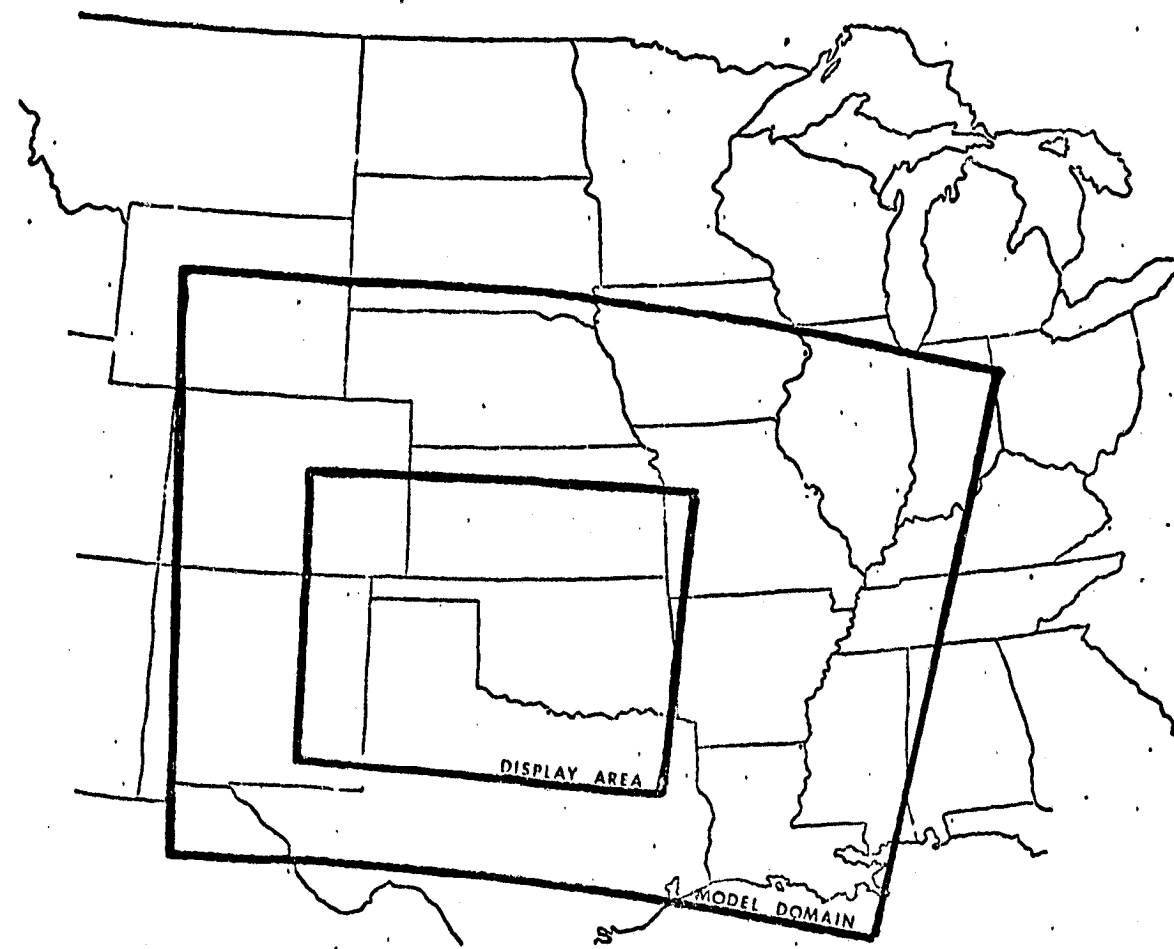
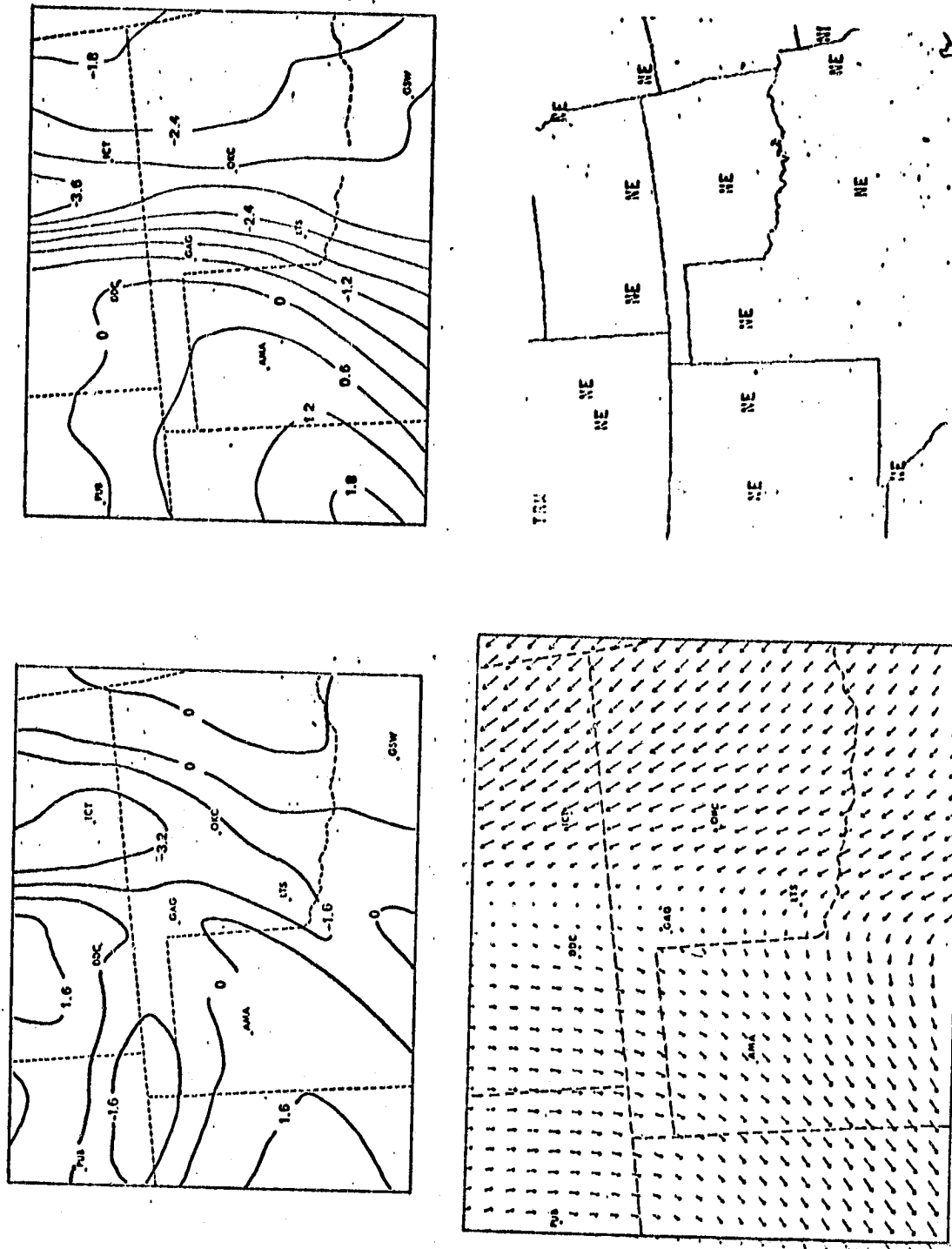


Figure 3-34. The 38 km model domain and display area for the 18 May 1978 case. The outer box demarcates the model domain. The inner box indicates the display area.



Ten hour 400 m model forecast valid at 2200 GMT 18 May 1978.
 Upper left: Divergence at intervals of $1.6 \times 10^{-5} \text{ s}^{-1}$.
 Upper right: 750 m or at intervals of 0.6 hPa .

Upper right: 750 m at intervals of 0.6 s; given at intervals of 1.6 x 10-3 s = 1.

Lower left: Wind vectors.

Lower right: National Weather Service radar summary for 2035 CMT 18 May

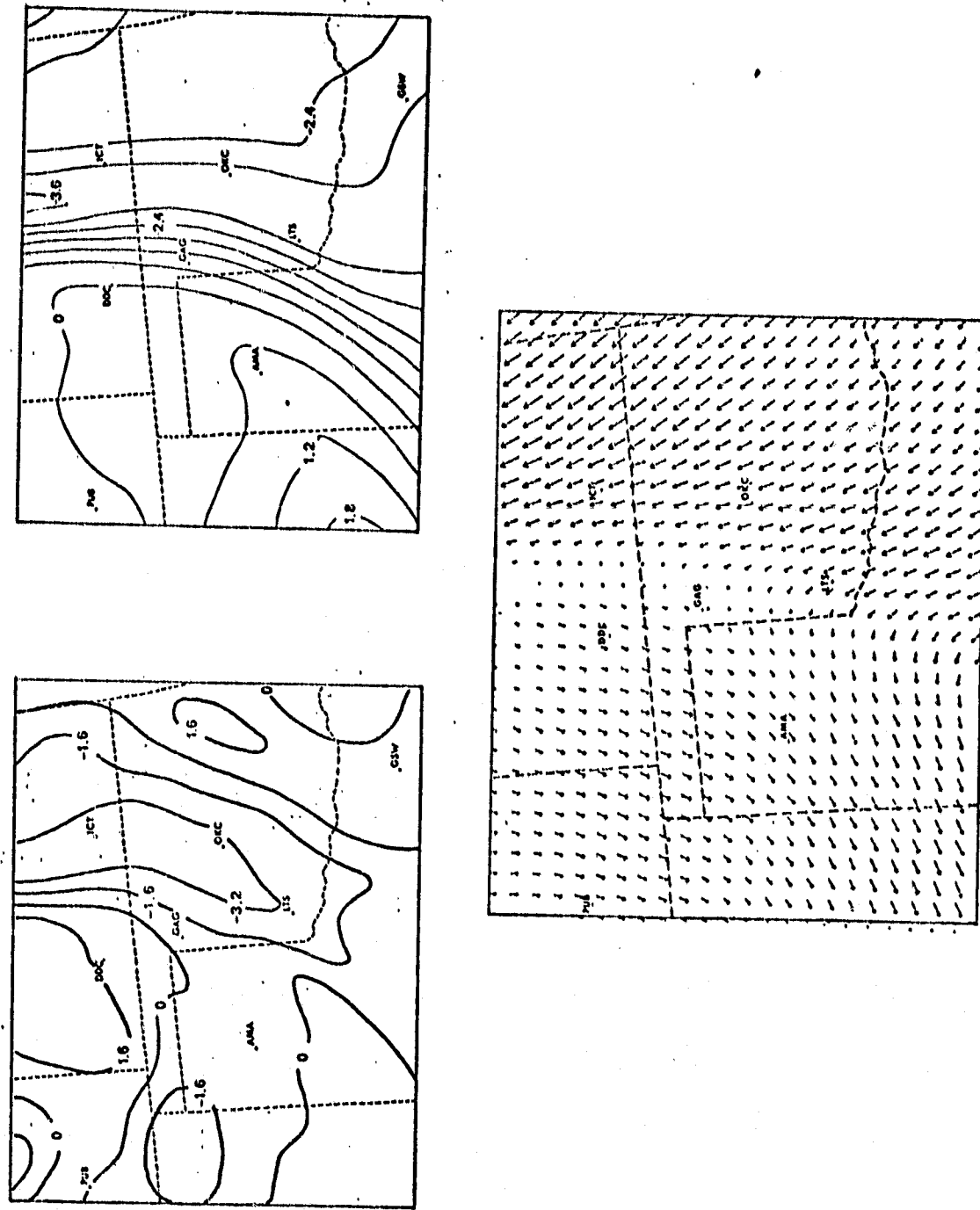


Figure 3-35b. Eleven hour 400 m model forecast valid at 2300 GMT 18 May 1978.
 Upper left: Divergence at intervals of $1.6 \times 10^{-5} \text{ s}^{-1}$.
 Upper right: 750 m σ E at intervals of 0.6.
 Bottom: Wind vectors.

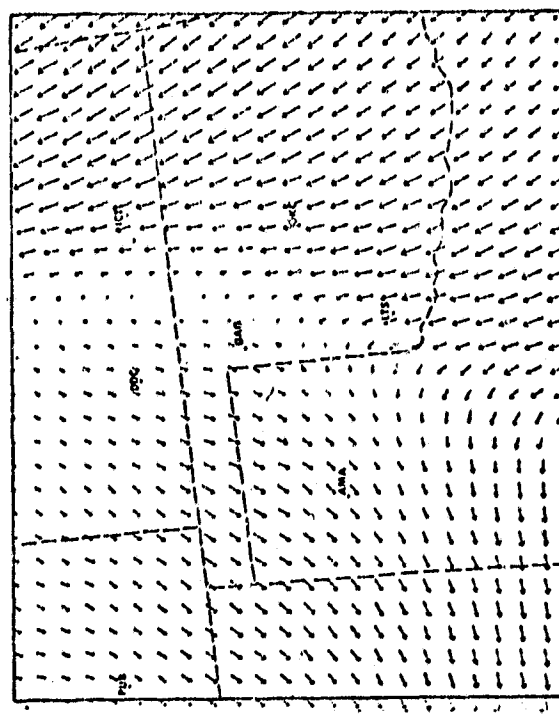
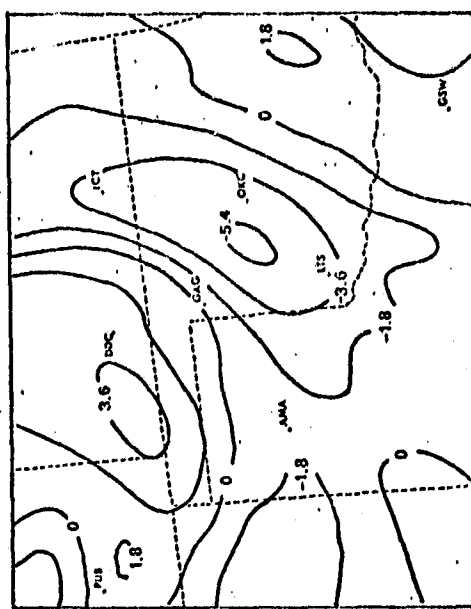
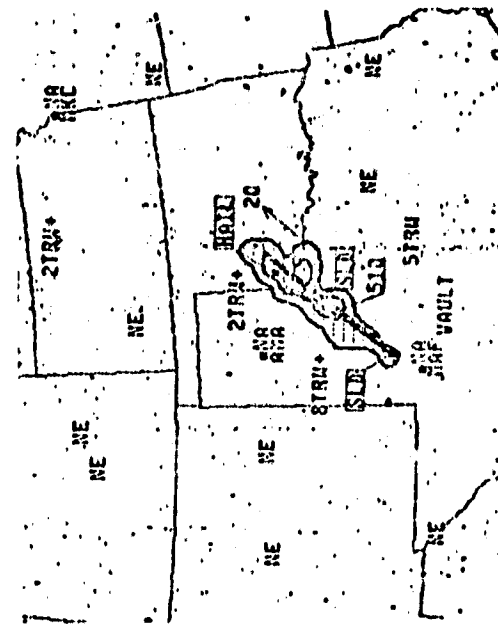
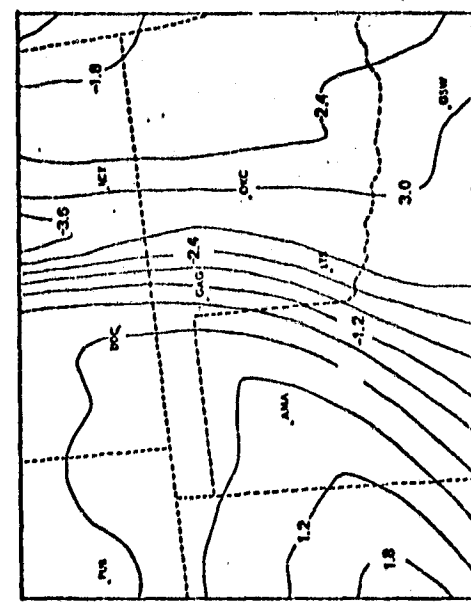


Figure 3-35c. Twelve hour 400 m model forecast valid at 0000 GMT 19 May 1978.
Upper left: Divergence at intervals of $1.8 \times 10^{-5} \text{ s}^{-1}$.
Upper right: 750 m σ at intervals of 0.6.

Lower left: National Weather Service radar summary for 2335 GMT 18 May.
Lower right: Wind vectors.

ORIGINAL PAGE IS
OF POOR QUALITY

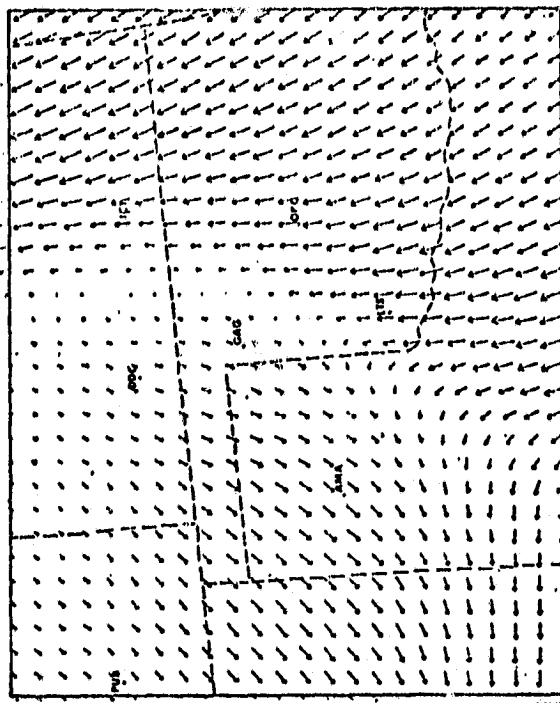
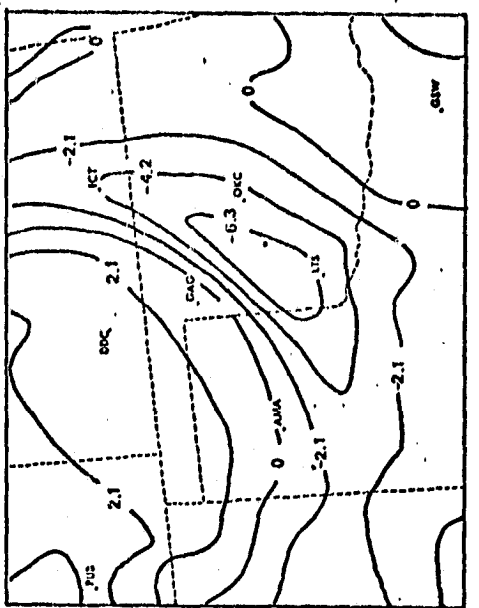
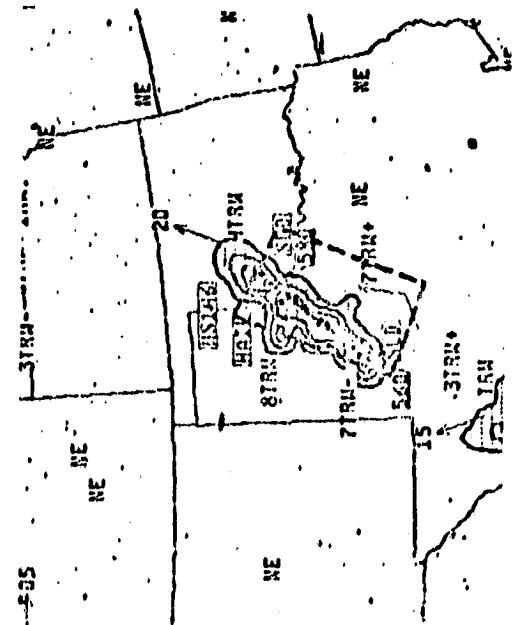
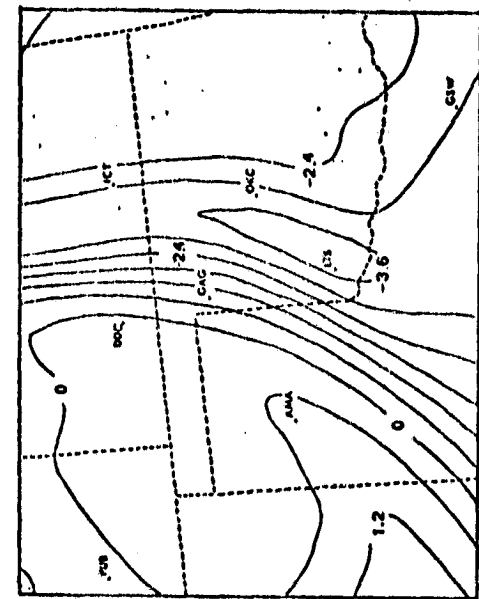


Figure 3-35d. Thirteen hour 400 m model forecast valid at 0100 GMT 19 May 1978.

Upper left: Divergence at intervals of $2.1 \times 10^{-5} \text{ s}^{-1}$.

Upper right: 750 m σ E at intervals of 0.6.

Lower left: Wind vectors.

Lower right: National Weather Service radar summary for 0035 GMT 19 May.

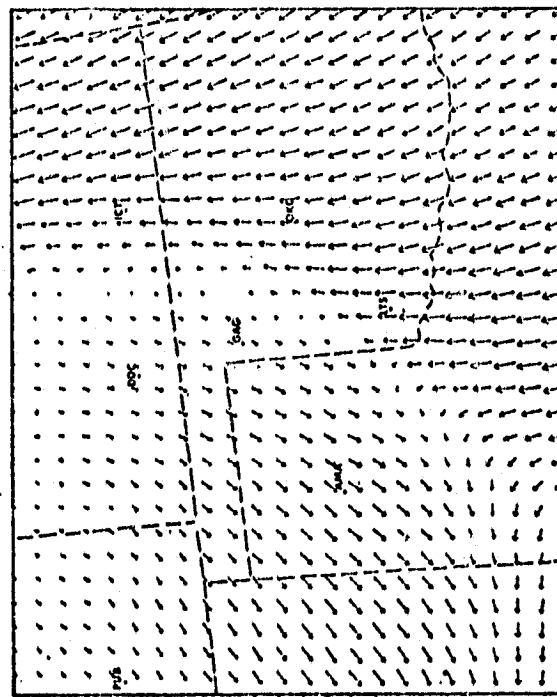
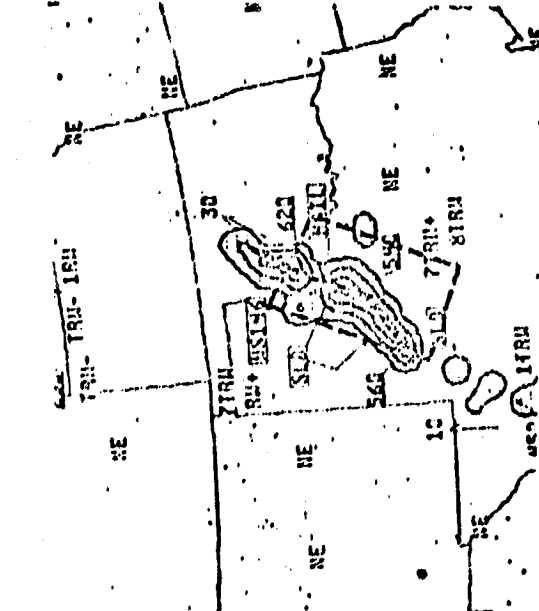
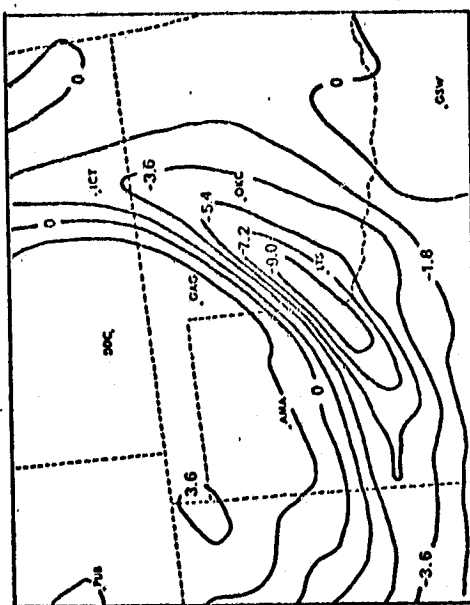
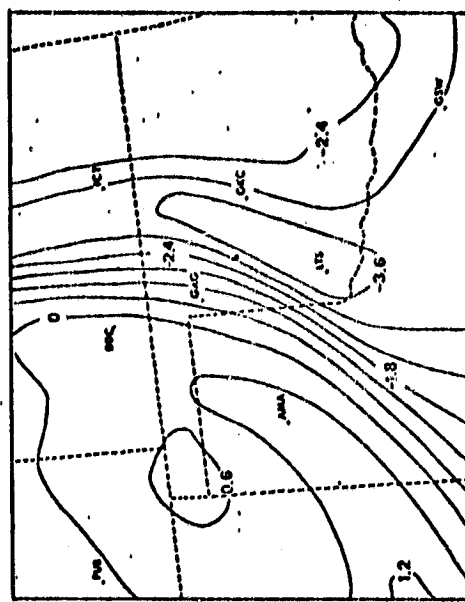


Figure 3-35e. Fourteen hour 400 m model forecast valid at 0200 GMT 19 May 1978.
 Upper left: Divergence at intervals of $1.8 \times 10^{-5} \text{ s}^{-1}$.

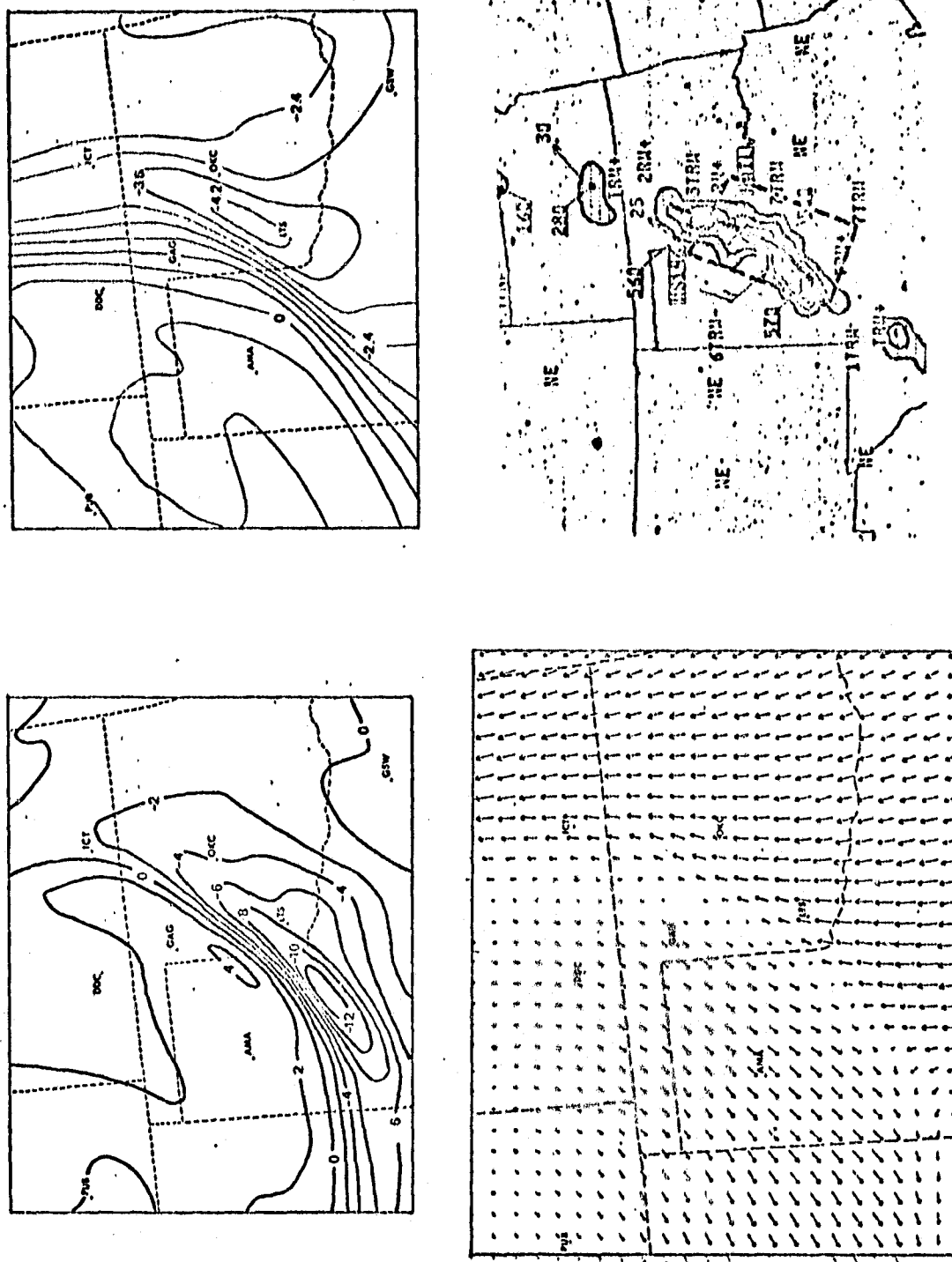


Figure 3-35f. Fifteen hour 400 m model forecast valid at 0300 GMT 19 May 1978.
Upper left: Divergence at intervals of $2 \times 10^{-5} \text{ s}^{-1}$.
Upper right: 750 m σ_E at intervals of 0.6.
Lower left: Wind vectors.
Lower right: National Weather Service radar summary for 0235 GMT 19 May.

Upper left: Divergence at intervals of $2 \times 10^{-5} \text{ s}^{-1}$.
Upper right: 750 m σ_E at intervals of 0.6.
Lower left: Wind vectors.
Lower right: National Weather Service radar summary for 0235 GMT 19 May.

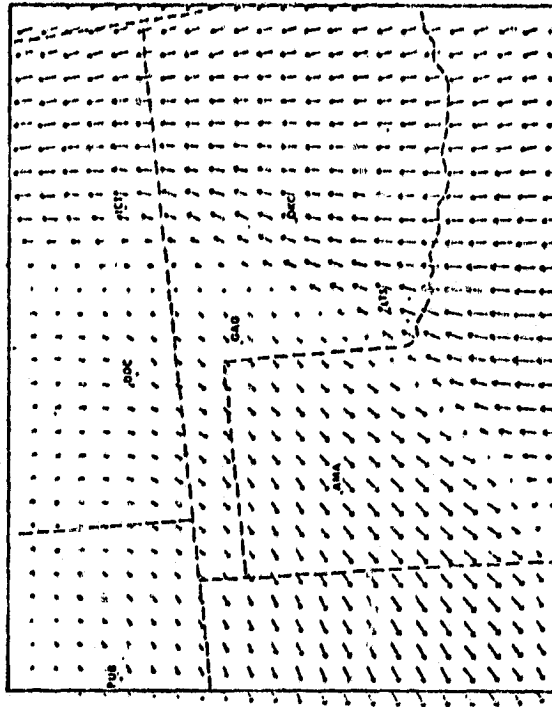
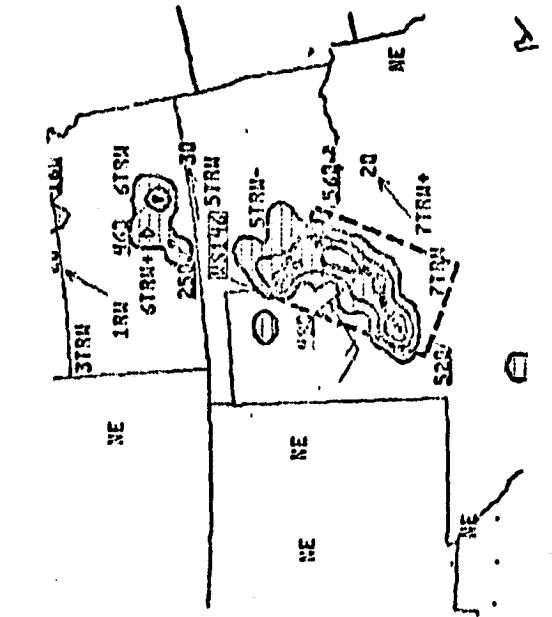
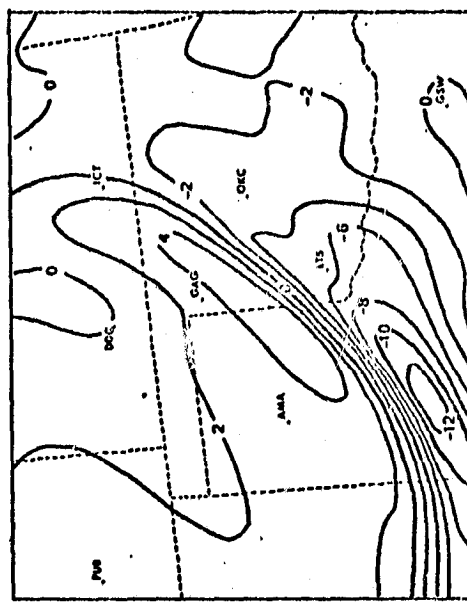
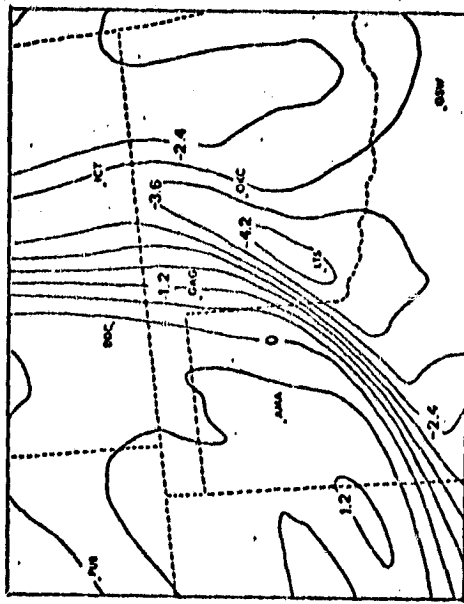


Figure 3-35g. Sixteen hour 400 m model forecast valid at 0400 GMT 19 May 1978.
Upper left: Divergence at intervals of $2 \times 10^{-5} \text{ s}^{-1}$.

Upper left: Divergence at Intervals of 2×10^{-5} .
 Upper right: 750 m.s. at intervals of 0.6

upper right: /30 M 8E at lower left: Wind vectors

Lower left: National Weather Service radar summary for 0335 GMT 19 May.
Lower right: Wind vectors.

ORIGINAL PAGE IS
OF POOR QUALITY

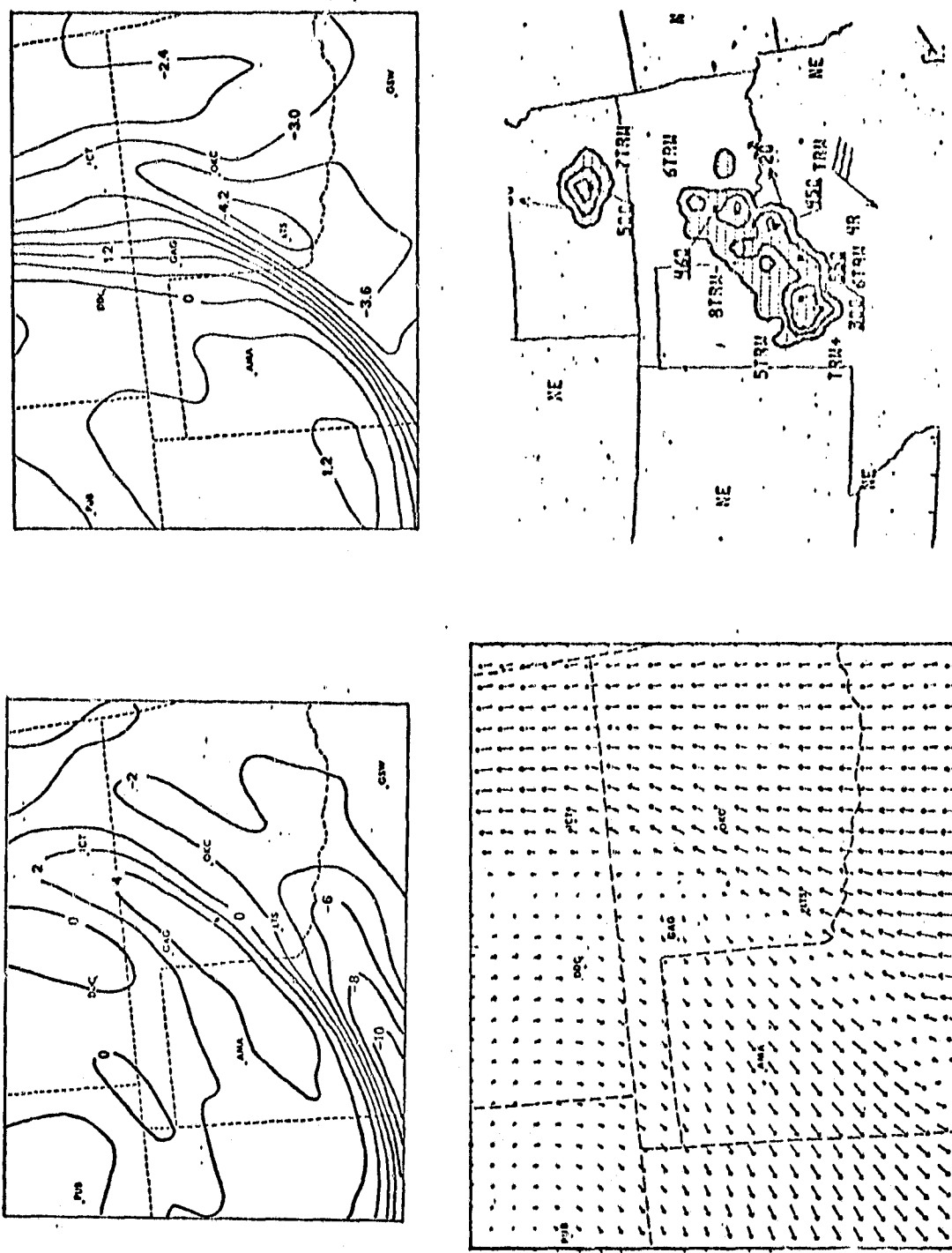


Figure 3-35h. Seventeen hour 400 m model forecast valid at 0500 GMT 19 May 1978.
Upper left: Divergence at intervals of $2 \times 10^{-5} \text{ s}^{-1}$.

Upper right: σE at intervals of 0.6.

Lower left: Wind vectors.

Lower right: National Weather Service radar summary for 0535 GMT 19 May.

4.0 Summary

The 60 day test period during the spring of 1978 permitted the achievement of the following goals:

- (1) A mesoscale numerical model was run in real time with a standard meteorological data base on a daily basis for the first time.
- (2) A mesoscale numerical model simulated the development and interaction of sub-synoptic and mesoscale waves with reasonable fidelity.
- (3) A mesoscale numerical model provided a useable forecast of the preferred mesoscale areas of convective activity.
- (4) Areas in which the mesoscale model can be improved were revealed.

The following technical problems were encountered during the test:

- (1) The limited size of the model domain prevented the proper handling of synoptic wavelengths greater than 2000 km for time periods in excess of approximately 8 hours. This often lead to a situation in which a well simulated mesoscale flow field was superimposed upon a slowly degrading macroscale forecast. In time, this created new misforecasted mesoscale fields. The chief result of this problem was the lack of eastward propagation of mesoscale features originating within rapidly moving or developing synoptic scale waves.

- (2) Poor initial low level data over high elevation regions caused the model to erroneously create or amplify areas of convergence or potential instability in and surrounding the high elevation regions. This was a result of the need to use atmospheric data at levels which are below the surface on the Western Plains and in the Rocky Mountain region. This problem seriously affected the forecast in the high elevation regions.
- (3) The geostrophic initialization of momentum generated fictitious waves during the first few hours of the forecast. These high frequency waves were dampened by the model numerics after this initial period. However, they did affect the quality of the model forecast for the first couple of hours.
- (4) The model vertical resolution in the lower troposphere may have been insufficient to capture the complete dynamical process associated with the generation and amplification of the mesoscale convergence zones.
- (5) Only the distribution of an index could be made available to users on a real time basis. Several forms of the index were employed. However, considerable information was lost by condensing the entire model forecast into one simple 0 to 10 index. Thus, the use of an index tended to underplay the model's achievements in simulating the generation and interaction of the mesoscale waves.

The following improvements are expected to alleviate these problems and improve the forecast substantially:

- (1) The horizontal domain of the model will be expanded.

At present the limiting matrix size on the STAR 100A computer constrains the horizontal matrix size to 60×48 . This limitation is a result of the STAR "hardware" making only 500,000 words of memory presently available. However, the memory potential can be doubled by rewriting the program in SL-1, a newly developed language at NASA-Langley, which requires 32-bit as opposed to the normal STAR FORTRAN 64-bit arithmetic. This will increase the maximum matrix size to 90×64 . In 1980, the STAR 100A memory will increase to 1,000,000 words. This will allow the horizontal matrix size to be expanded to 134×84 . The relative areal coverages of these matrix sizes with a 38 km model is illustrated in Figure 4-1. This should improve the forecast of the longer wavelength synoptic features significantly.

- (2) A terrain representation will be incorporated into the model. This will eliminate the necessity to use data which is obtained by extrapolation to positions below the surface of the earth.
- (3) Additional vertical resolution will be added to the lower tropospheric region of the model. Several cases (e.g. 12 May, 18 May) have already been evaluated using levels at 400, 750, 1150, 1650 and 2275 meters, as opposed to the 1150, 2275, 3400

meter levels used during the test period. This has noticeably improved the forecast.

- (4) The geostrophic initialization scheme will be replaced by a scheme which will represent the initial wind field with greater realism. This will eliminate fictitious waves early in the forecast period.
- (5) Additional scales of motion will be simulated by employing several smaller scale nested grids in addition to the 38 km grid. This should increase the spatial and temporal resolution of the convective forecast.
- (6) Future dissemination of the model forecasts are planned to include actual model forecast parameters such as the equivalent static stability, low level vertical motions and low level moisture. This should give a better representation of the model forecast than the use of a simple index.

In conclusion, the 1978 test period proved useful in establishing the feasibility of real time mesoscale numerical models. The model did appear to capture the essence of the mesoscale organization of convection, although certain technical problems prevented the generation of a consistently excellent product. Improvements planned during the next year should increase the quality and fidelity of the model significantly.

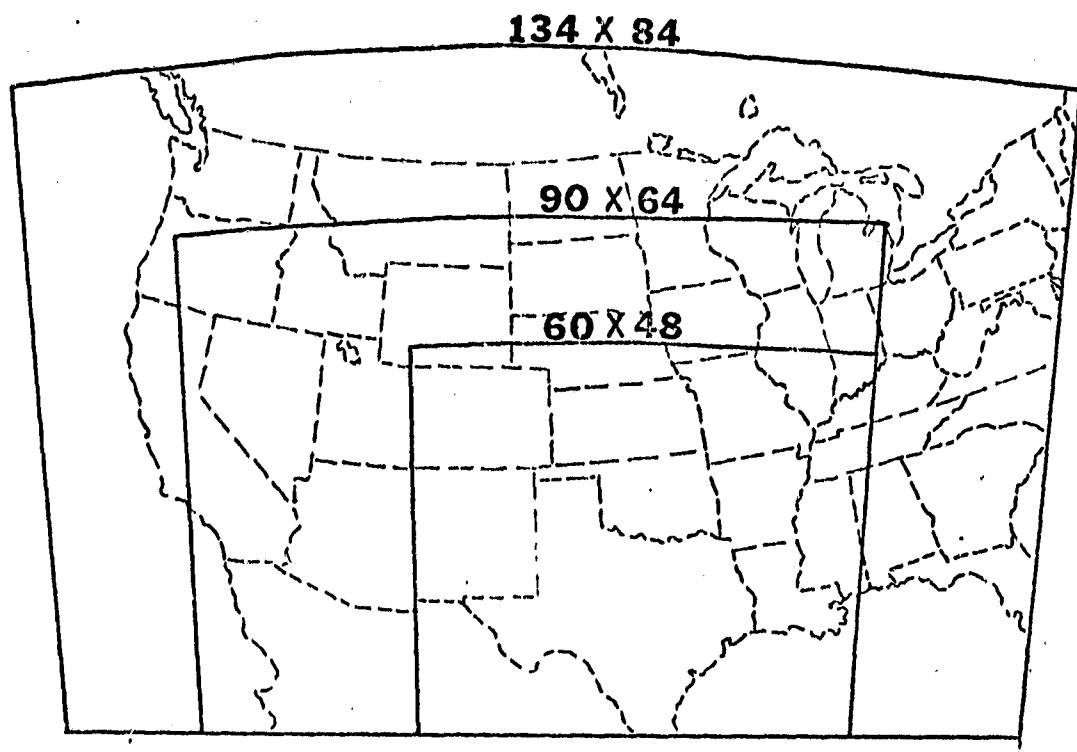


Figure 4-1. The relative areal coverage of three different matrix sizes when employed to represent a 38 km horizontal grid mesh. The 60×48 matrix was used during the spring 1978 test period. Translation of the model code into the SL-1 language will permit the use of a 90×64 matrix within the next year. An increase in the STAR 100A memory will permit the use of a 134×84 matrix for the 38 km model by 1980.

5.0 References

- Hess, S.L., 1959: Introduction to Theoretical Meteorology. Holt, Rinehart and Winston, New York, 362 pp.
- Holton, J.R., 1972: An Introduction to Dynamic Meteorology. Academic Press, New York, 319 pp.
- Kreitzberg, C.W., D.J. Perkey and J.E. Pinkerton, 1974: Mesoscale modeling, forecasting and remote sensing research. Project Themis Final Report, AFCRL-TR-74-0253, Dept. Physic and Atmos. Sci., Drexel University, 318 pp. [NTIS: AD-784-875]
- Orlanski, I., 1975: A rational subdivision of scales for atmospheric processes. Bulletin of the American Meteorological Society, 56, 527-530.
- Paine, D.A., J.W. Zack, J.T. Moore and R.J. Posner, 1975: A theory for the conservation of three dimensional relative vorticity which describes the cascade of energy-momentum leading to tornadic vorticities. American Meteorological Society Preprint - Ninth Conference on Severe Local Storms, Oct. 21-23, Norman, Oklahoma, pp. 131-138.
- Paine, D.A. and M.L. Kaplan, 1976: An equivalent potential vorticity theory applied to the analysis and prediction of severe storm dynamics. American Meteorological Society Preprint - Sixth Conference on Weather Forecasting and Analysis, May 10-14, Albany, New York, pp. 98-105.
- Paine, D.A., J.W. Zack and M.L. Kaplan, 1978: The cascade concept of severe local storm generation: horizontal convergence development. Manuscript submitted to Monthly Weather Review.
- Palmén, E. and C.W. Newton, 1969: Atmospheric Circulation Systems. Academic Press, 603 pp.
- Perkey, D.J., 1976: A description and preliminary results from a fine-mesh model for forecasting quantitative precipitation. Monthly Weather Review, 104, 1513-1525.
- Richardson, L.F., 1922: Weather Prediction by Numerical Process. New York, Dover.
- Shuman, F.G. and J. Hovermale, 1968: An operational six-layer primitive equation model. Journal of Applied Meteorology, 7, 525-547.
- Storm Data, 1978: NOAA Environmental Data Services, Vol. 20, Nos. 4-6, April, May, June 1978.
- Sutton, O.G., 1955: Atmospheric Turbulence. Wiley, New York.

6.0 Appendix

Definition of Symbols

<u>Symbol</u>	<u>Definition</u>
D	divergence, $\frac{\partial u}{\partial x} + \frac{\partial v}{\partial y}$
f	Coriolis parameter; $2\Omega \sin \phi$
g	gravitational acceleration
p	pressure
T	temperature
u, v	east-west, north-south wind components
x, y	east-west, north-south coordinates
a	specific volume
β	change of Coriolis parameter, f, with longitude
λ	$2\Omega \cos \phi$
$\frac{\partial}{\partial t}, \frac{\partial}{\partial x}, \frac{\partial}{\partial y}, \frac{\partial}{\partial p}, \frac{\partial}{\partial \theta}, \frac{\partial}{\partial z}$	local derivatives
$\frac{d}{dt}$	total derivative
∇	2 dimensional spatial operator, $\frac{\partial}{\partial x} \hat{i} + \frac{\partial}{\partial y} \hat{j}$
∇_3	3 dimensional spatial operator, $\frac{\partial}{\partial x} \hat{i} + \frac{\partial}{\partial y} \hat{j} + \frac{\partial}{\partial z} \hat{k}$
F	friction term
J(u, v)	Jacobian of $u, v \equiv \frac{\partial u}{\partial x} \frac{\partial v}{\partial y} - \frac{\partial v}{\partial x} \frac{\partial u}{\partial y}$
∇^2	2 dimensional Laplacian operator
ρ	density
θ	potential temperature

Definition of Symbols, continuedSymbolDefinition θ_E

equivalent potential temperature

$$\theta_E = \theta \exp \left\{ \frac{L Q_s}{C_p T} \right\}$$

w

 $\frac{dz}{dt}$. vertical motion in z coordinate system ζ

kth component of relative vorticity;

$$\frac{\partial v}{\partial y} - \frac{\partial u}{\partial y}$$

 σ_E

equivalent hydrostatic stability;

$$\sigma_E = \frac{\alpha^2}{\theta_E} \frac{\partial \theta_E}{\partial z}$$

Q

mixing ratio

 Q_s

saturation mixing ratio

m

map scale factor

 p_v

water vapor density

 C_p

specific heat at constant pressure

L

latent heat of vaporization